AN ABSTRACT OF THE THESIS OF

Jinwon Kim for the degree of Doctor of Philosophy in

Atmospheric Sciences presented on November 29, 1990.

Title: Turbulent and Gravity Wave Transport in the Free Atmosphere

Redacted for Privacy

Abstract approved: _____

Larry Mahrt

Turbulent fluxes and related parameters in the free atmosphere are estimated from aircraft data obtained in SESAME and CABLE. Estimated eddy diffusivities and mixing lengths are found to decrease rapidly with increasing gradient Richardson number (Ri) at small Ri, and then decrease more slowly at large Ri. The eddy Prandtl number increases with increasing Ri. This suggests that the generation of TKE by the pressure correlation term becomes more significant as the stability increases.

A simple representation of the eddy diffusivities in the free atmosphere is proposed by using an asymptotic mixing length and a nondimensional function of Ri. Tests of this formulation in a column model indicates that nocturnal CAT may become significant near the low-level jet above NBL. This constitutes the first systematic study of the residual layer above NBL.

The momentum flux by orographic gravity waves and the turbulent heat flux in the wave breaking regions are estimated from aircraft data sets from two days in ALPEX. The calculation of these fluxes allows the first direct comparison between gravity wave momentum transport models and observed fluxes.

Toward this goal, the gravity-wave stress supersaturation theory by Lindzen

(1988) is generalized for the application to vertically-varying mean flows. The wave momentum flux estimated from the generalized model agrees well with the observations for both the cases with and without a critical level. The wave breaking leads to convectively unstable regions of 10 - 20 km wide where the magnitude of the observed upward turbulent heat flux can be approximated by using the flux gradient relationship in which the mixing length and modified shear are derived from the generalized wave stress supersaturation condition.

The *effective* height (h_e) of the surface topography varies substantially between the two days. Our sensitivity tests tentatively suggest

$$h_e = \mathbf{min}\left[h_0, 0.32\frac{U_0}{N_0}\right],$$

close to that proposed by Stern and Pierrehumbert (1988), where h_0 is the mountain height, and U_0 and N_0 are the surface wind and stratification.

Turbulent and Gravity Wave Transport in the Free Atmosphere

by

Jinwon Kim

A THESIS

submitted to

Oregon State University

in partial fulfillment of
the requirements for the
degree of

Doctor of Philosophy

Completed November 29, 1990

Commencement June 1991

APPROVED:

Redacted for Privacy

Professor of Atmospheric Sciences in charge of major

Redacted for Privacy

Head of Department of Atmospheric Sciences

Redacted for Privacy

Dean of Graduate School

Date thesis is presented November 29, 1990

Typed by researcher for Jinwon Kim

To my parents

ACKNOWLEDGEMENTS

I greatly appreciate the guidance and support of my major advisor Prof. Larry Mahrt. Without his thoughtful comments and helpful discussions I could never complete this study. Special thanks are due to Dr. D. Lenschow for supplying the valuable CABLE data. Comments of Dr. T. Dunkerton on the wave breaking was very helpful. I also thank Dr. R. B. Smith and Mr. Gluhosky for supplying the radiosonde sounding data for ALPEX and necessary software. Drs. J. Noihlan and Sam Chang supplied valuable information for the analysis of 19 May HAPEX and 7 May SESAME, respectively.

Thanks to my colleagues, Nimal Gamage and Michael Ek for many helpful discussions and comments. Wayne Gibson provided indispensable computing assistance. Special thanks to my wife, Young-Sook, for her love, understanding, and endurance and to my parents and friends for their support.

This research was financially supported by the Geophysical Laboratory under contract F19628-88-K-001.

TABLE OF CONTENTS

LIST OF FIGURES

Turbulent and Gravity Wave Transport in the Free Atmosphere

1. Introduction

Turbulence and gravity waves are two of the most important small-scale mechanisms which transport momentum and heat in the free atmosphere. There have been numerous attempts to represent the fluxes due to turbulence and gravity waves in the free atmosphere in numerical models of large-scale flows. However, direct comparisons between such representations and actual turbulence and gravity wave observations are not available. While gravity waves and clear air turbulence interact in actual atmospheric flows, their parameterization is also superficially linked in large-scale numerical models. For example, turbulent mixing may be artificially enhanced to compensate for lack of a formulation for gravity wave drag.

This study will provide first observational support for the parameterization of turbulent and gravity wave transport in the free atmosphere. In Chapter 2, a formulation of the eddy diffusivity is derived from aircraft observations and applied to a column model. Chapter 3 of this study estimates momentum fluxes by gravity waves from aircraft observations and compares such observations with model predictions.

1.1 Clear air turbulence transport

Turbulence in the free atmosphere has been recognized as one of the principal sinks of atmospheric kinetic energy. Previous studies suggest that as much as 25 % of the dissipation of atmospheric kinetic energy occurs through clear air turbulence in the mid- and upper troposphere (Heck *et al*, 1977). Clear air turbulence also redistributes heat and momentum and can influence the evolution of mesoscale and synoptic-scale disturbances in the free atmosphere.

Turbulence in the free atmosphere is usually localized in regions where

the vertical shear is large. Clear air turbulence is often found in thin, slanting baroclinic layers (internal fronts) which are characterized by large vertical shear, large horizontal potential temperature gradient, and small Richardson numbers (Heck *et al*, 1977). Clear air turbulence is also induced by localized disturbances such as breaking gravity waves. Consequently the frequency of occurrence and strength of turbulence in the free atmosphere is related to the types of underlying terrain (e.g. Trout and Panofsky, 1969) and attendant mesoscale disturbances.

As a result, proper representation of turbulent fluxes in the free atmosphere is one of the important problems in numerical modeling of large-scale flows. Most of the previous representations of the turbulent fluxes in the free atmosphere were attempted by adopting a similarity relationship between turbulent fluxes and gradients of mean flow variables for the surface layer (e.g. Louis, 1979). The validity of extending the surface-layer similarity theory to the free atmosphere is not known. Unlike the surface layer, turbulence in the free atmosphere is not directly related to the distance from the surface. Observations of turbulent fluxes and their relationship with the vertical variations of mean large-scale flow in the free atmosphere are rarely documented in the literature.

In this study, seventeen slant soundings obtained on 6, 7, and 24 May 1983 in CABLE (Clear Air Turbulence and Boundary Layer Experiment) and eight soundings and one horizontal leg obtained on 6 May 1979 in SESAME (Severe Environmental Storms and Mesoscale Experiment) are analyzed to estimate the turbulent fluxes in the free atmosphere. The analyses focus on the estimation of the turbulent length scale for heat transport and the turbulent Prandtl number which lead to formulation for the eddy diffusivities in the free atmosphere.

We will establish an approximate relationship between the observed turbulent fluxes and the stability parameter measured from large-scale mean flow profiles. Such a relationship is documented in Kennedy and Shapiro (1980) for the upper part of the troposphere. Their estimation of fluxes includes contributions from motions on horizontal scales up to several hundred kilometers which include hydrostatic gravity waves. The validity of relating fluxes by wave scale disturbances to the mean gradient and eddy diffusivity is unknown. We will only consider turbulent scale motions in estimating fluxes in this study.

The gradient Richardson number calculated across bulk turbulent layers will be used as the stability parameter. The stability of linearized dynamical systems is related to the gradient Richardson number. Laboratory experiments also seem to support the gradient Richardson number criterion for the onset of turbulence (Thorpe, 1973). In the present study the gradient Richardson numbers calculated across bulk turbulent layers vary from 0.2 to 1.0 while those calculated outside the turbulent layers are usually larger than 1.5. In a few exceptions the gradient Richardson number drops to about 0.6 in a quiescent layer.

Estimation of turbulent fluxes requires separation of turbulent fluctuations from the "mean" flow. Turbulence-scale motions are usually selected by high-pass filtering the raw records. Estimated fluxes in stable stratification are often sensitive to the cutoff filterlength. Due to uncertainties in the scale of the largest turbulent eddies and their separation from gravity waves (Finnigan *et al*, 1984), a study of the scale dependence of the motions and fluxes will be initiated in Section 2.1.

The eddy diffusivities, associated turbulent Prandtl numbers and turbulent mixing lengths are estimated from the observed fluxes and mean flow profiles in

Section 2.2 The mixing length and the turbulent Prandtl number will be related to the gradient Richardson number. The resulting representations of the mixing length and turbulent Prandtl number will be compared against those based on Louis (1979).

The eddy diffusivity formulation derived from the observations will be applied to a column model. The turbulence in the residual layer (remnant of the daytime mixed layer) above the nocturnal surface inversion layer leads to adjustment of the mean flow. Observations of Lu *et al* (1983) and André and Mahrt (1982) indicate the occurrence of significant turbulence where significant shear develops in what appears to be a residual layer. Strong shear develops at the bottom of the residual layer (top of the surface inversion layer) on the underside of the low-level jet (André and Mahrt, 1982). Although not previously studied, shear may develop at the top of the residual layer for similar reasons. In Section 2.3, the influence of eddy mixing on the evolution of low-level flow in the residual layer will be studied.

Turbulence is often intermittent in the upper part of a very stable boundary layer, and seems to be generated by local shear not directly related to the surface stress (Mahrt, 1985). Consequently models based on boundary layer similarity appear to approximate only the weakly or moderately stable boundary layer, but poorly describe the very stable boundary layer. For example, boundary layer similarity model fails to represent the effect of local shear near the top of the surface inversion layer associated with the nocturnal low-level jet. We will attempt to include the effects of local shear generation of turbulence in the upper part of the stable boundary layer by merging the free atmospheric mixing parameterization with the boundary-layer formulation (Subsection 2.3.4). In Subsections 2.3.5 and 2.3.6, we will investigate the influence of large-scale

subsidence and the vertical shear of geostrophic wind on the turbulent mixing and the evolution of the low-level flow.

1.2 Gravity wave momentum transport

Topographically-generated internal gravity waves transport significant momentum vertically in the free atmosphere. The nondissipative nature of internal gravity waves (Eliassen and Palm, 1960) may allow the wave stress at the surface to be transferred far into the upper atmosphere where the density is small. The impact of gravity wave momentum transport becomes significant for motions on long time scales, typically longer than a week, especially over continental areas during the wintertime (Palmer *et al*, 1986).

The momentum transport by internal gravity waves is mostly confined to the atmosphere over the source region (Smith, 1977). Hence, momentum transfer by gravity waves can cause significant local variation of the mean flow above significant topography. Spectral analyses show that the mesoscale variances are climatologically much larger over mountainous areas than over flat land surfaces or the ocean, and the observed differences are mostly due to the gravity wave activity in the atmosphere (Jasperson *et al*, 1990). Lilly *et al* (1982) and Brown (1983) found that the stress due to gravity-wave scale disturbances is significant over mountainous areas, sometimes exceeding several N/m^2 at the middle of the troposphere. For a summary of the observed values of the gravity wave stress values in previous studies, see Palmer *et al* (1986).

Aircraft data sets collected on 6 and 25 March 1982 in ALPEX (Alpine Experiment) will be analyzed in order to study the most significant disturbances generated by the underlying mountain range and the related momentum and heat fluxes. The mean flow structures on these two days are quite different. On 6 March 1982, strong Bora flow contains a critical layer for stationary gravity

waves at about 5 km above sea level. Strong directional shear and the existence of a critical layer usually implies that wave breaking will occur below the critical level and most of the gravity waves generated by the underlying coastal range will not be able to propagate into upper troposphere. On 25 March 1982, the low-level wind is weaker and increases gradually with height without significant vertical change of wind direction. Such conditions are favorable for propagation of topographically generated gravity waves into the upper atmosphere. This study will show that the observed disturbances possess features of internal gravity waves and hydraulic jump theory is not necessary to explain the variation of the observed flow.

The surface topography induces gravity waves with wide range of scales and frequencies. Because the horizontal length scale and frequency are the most significant characteristics which influence the vertical propagation of gravity waves, it is important to estimate the scales of significant wave activity. The Haar-wavelet variance is more useful than the Fourier transform for estimating the scales of isolated disturbances (Gamage, 1990). Breaking waves are usually accompanied by the steepening of the streamlines (Smith, 1977). In Section 3.1, we will investigate the skewness of the Haar-wavelet transform as an indicator of the asymmetry and scale of the gravity wave motions and wave steepening. However conventional spectral filtering will be used to compute fluxes.

Such fluxes will be used to test simple models of gravity wave transport of momentum. Representation of the *gravity wave drag* in terms of mean flow profiles have been applied to large-scale numerical models with some limited success (Hunt, 1990). A combination of linear gravity wave solutions with hydrodynamic instability criteria, such as Kelvin-Helmholtz instability or convective instability, can significantly improve the simulated large-scale flow field

(Holton, 1982; Palmer *et al*, 1986; McFarlane, 1987). Nonetheless, significant features related to the surface stress and wave breaking aloft, such as the *effective* height of surface topography, the effects of nonlinear lower boundary conditions (Smith, 1977), and saturation or supersaturation of the gravity wave stress, are not clearly understood. Also, verification of the key hypotheses for wave breaking are yet to be established. In fact, previous theories based on saturation and supersaturation conditions have not been compared directly with observed atmospheric fluxes. This is one of main goals of this study.

Supersaturation of gravity wave stress allows for greater transport of wave momentum into the upper atmosphere. The wave stress supersaturation condition presented by Lindzen (1988) is for an isothermal atmosphere with constant wind speed; hence it is not directly applicable to most atmospheric cases. In Section 3.2, we will generalize Lindzen's theory for vertically varying mean flows by introducing the *equivalent scale height* which replaces the scale height for an isothermal atmosphere. Also, the depth of the wave breaking region will be estimated from the amplitude of streamline disturbances rather than from the vertical wavelength.

We will estimate the vertical profile of wave stress by combining the solution to a linear gravity wave equation for the first-order lower boundary condition by Smith (1977) with the gravity wave stress supersaturation condition introduced by Lindzen (1988). Then, the wave momentum flux estimated from various combinations of lower boundary conditions and wave breaking conditions such as wave stress saturation or supersaturation are compared with the vertical profiles of the observed momentum flux. Does the linear gravity wave theory provide a realistic description of height-dependence of the wave momentum flux? Are the predictions based on the wave stress saturation and supersaturation

conditions significantly different? Are the model predictions affected by the choice of zeroth-order or first-order lower boundary condition, and what is the realistic choice of an effective mountain height? Answers to these questions will be sought in Section 3.2.

The spatial variations of the turbulent heat flux will yield important information about the mechanisms of wave breaking. For example, if wave breaking occurs mainly by Kelvin-Helmholtz instability, we expect downward turbulent heat flux in the wave breaking region. If wave breaking occurs by convective instability, the turbulent heat flux will be locally upward in the wave breaking region. The supersaturation condition (Lindzen, 1988) allows for maintenance of some degree of convective instability corresponding to non-instantaneous adjustment to the convective instability. We will estimate the turbulent length scale, stratification, and vertical shear in the wave breaking regions explicitly from the mean flow profile and the horizontal length scale of the gravity wave (Subsection 3.2.5).

2. Turbulent Transport in the Free Atmosphere

2.1 Analyses of turbulent fluxes

The observations of clear air turbulence used in this study are generally from the first few kilometers above the boundary layer. No observations are from the middle and upper atmosphere.

On 5 May 1983 in CABLE, NCAR King Air flew from 0600 to 1000 LST in the east-west direction over western Kansas. The boundary layer was about 100 m deep at the beginning of the observational period and grew to a height of 500 m by the end of the observational period. The low-level wind was from the south-south-west and shifted to west-south-west above the boundary layer. The low-level wind maximum was located between 200 to 500 m above the ground and persisted throughout the observational period.

Flights on 24 May 1983 in CABLE were made over a distance of approximately 600 km in the north-south direction during the period from 1600 to 1900 LST. The flight path extended from over the Gulf of Mexico to near Oklahoma City. Winds on this day are generally north-easterly. The depth of the boundary layer is about 1 km over the ocean and decreases to about 500 to 600 m over the land. Clear air turbulence observed in CABLE flights occurs in regions occupying a relatively small portion of the observational area (dotted areas in Fig. 1). Isentropic analysis shows that such regions are characterized by large-amplitude mesoscale disturbances (Fig. 1).

Data on 6 May 1979 in SESAME were taken in and above a windy, weakly

stable nocturnal boundary layer over central Oklahoma in the early morning. The flight tracks are oriented in the north-south direction and are approximately

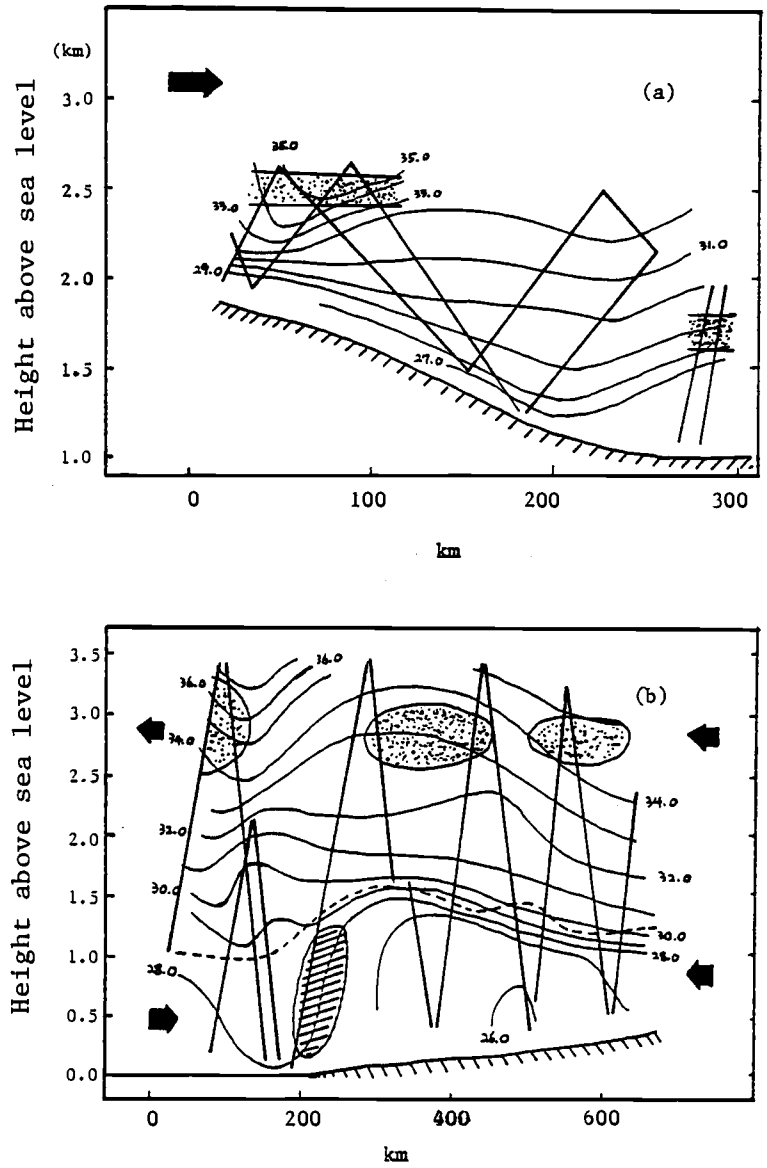

Fig. 1 Cross-section of the CABLE observational region (a) 5 May 1983, (b) 24 May 1983. Clear air turbulence is observed in the dotted regions. The region shaded with solid lines in (b) indicate horizontal convergence. Solid lines are the isentropes and the dashed line in (b) is the top of the boundary layer. Slant solid lines denote the aircraft flight path.

parallel to the wind at the flight levels. For a more detailed description of the flow on this day as well as 7 and 5 May 1979, see Lenschow *et al* (1987) and Mahrt (1985).

Estimation of the turbulence and mean flow from slant soundings requires careful investigation of the variation of the flow in the horizontal as well as in the vertical. Observations made by slant soundings contains both horizontal and vertical variations of the flow. Hence, the inferred horizontal structure of turbulence is contaminated by the vertical structure of the mean flow (Mahrt, 1985).

Increasing the averaging length for the estimation of horizontal mean flow to eliminate the influence of horizontal fluctuations reduces the vertical resolution of the mean flow. This problem becomes severe if the record contains large amplitude gravity waves and the large scale mean flow varies rapidly in the vertical. For example, an estimation of the mean flow from low pass filtering with a cutoff wavelength which is too small can lead to superficial unstable stratification. An example of sampling problems in estimating the horizontal flow structure and its vertical gradient from slant soundings due to the presence of a sinusoidal disturbance are discussed in the Appendix. In spite of these difficulties, slant soundings have successfully depicted the vertical structure of turbulence (e.g. Lenschow *et al*, 1987).

2.1.1 Estimation of the height-dependent mean flow

In the current study, horizontal mean values are calculated from slant soundings by first block-averaging the raw data over fixed intervals of typically 50 m depth although in one case a value of 200 m was used. The choice of averaging depth depends on a subjective assessment of natural layering, depending on the aircraft ascent or descent rate and dependent on the need for averaging

to reduce the influence of wave motions. The layers are chosen just above and below the the layers of turbulence. The block-averaged data is interpolated with cubic splines to obtain mean values at the levels corresponding to the top and bottom of the turbulent layer. If the observed flow varies significantly in the horizontal, the interval of block averaging is increased at the expense of the vertical resolution to reduce errors in estimating vertical gradients of mean variables. The maximum depth of the block averaging is limited by the depth of the turbulent layer.

Choice of averaging intervals in this way is somewhat subjective. Due to a wide variety of ascending and descending rates for each sounding (1 - 6 %) and the existence of large amplitude horizontal disturbances, one value of the averaging interval seems inadequate. For example, uniform horizontal averaging distance will result in a different averaging depth, and vice versa. When the block-averaging intervals were increased by a factor of two, the resulting gradient Richardson numbers by an average amount of about 50 % from those used in the following presentation with no preference for the changes to be positive or negative.

2.1.2 Scale dependence of the turbulent fluxes

The estimated turbulent fluxes are sometimes sensitive to the choice of the cutoff wavelength for high-pass filtering. In stratified flow, gravity waves are sometimes difficult to isolate from large turbulent eddies and may significantly contaminate the estimated fluxes. We will now use the cospectra to investigate the scale dependence of the high-pass fluxes. Cospectra of turbulence in stratified flow is particularly vulnerable to sampling problems because the clear air turbulence may be intermittent and patches of turbulence may contain only a few samples of the main eddies. Therefore the following analysis yields only a

rough assessment of the scale dependence of the flux.

Fig. 2 shows the composites of the cospectra and the quadrature of the temperature and vertical velocity observed on 6 May 1979 in SESAME and on 5 May 1983 in CABLE. The width of turbulent regions varies from 4 to 20 km so that sampling problems in the estimation of the cospectra and quadrature are large on scales larger than a few kilometers or greater.

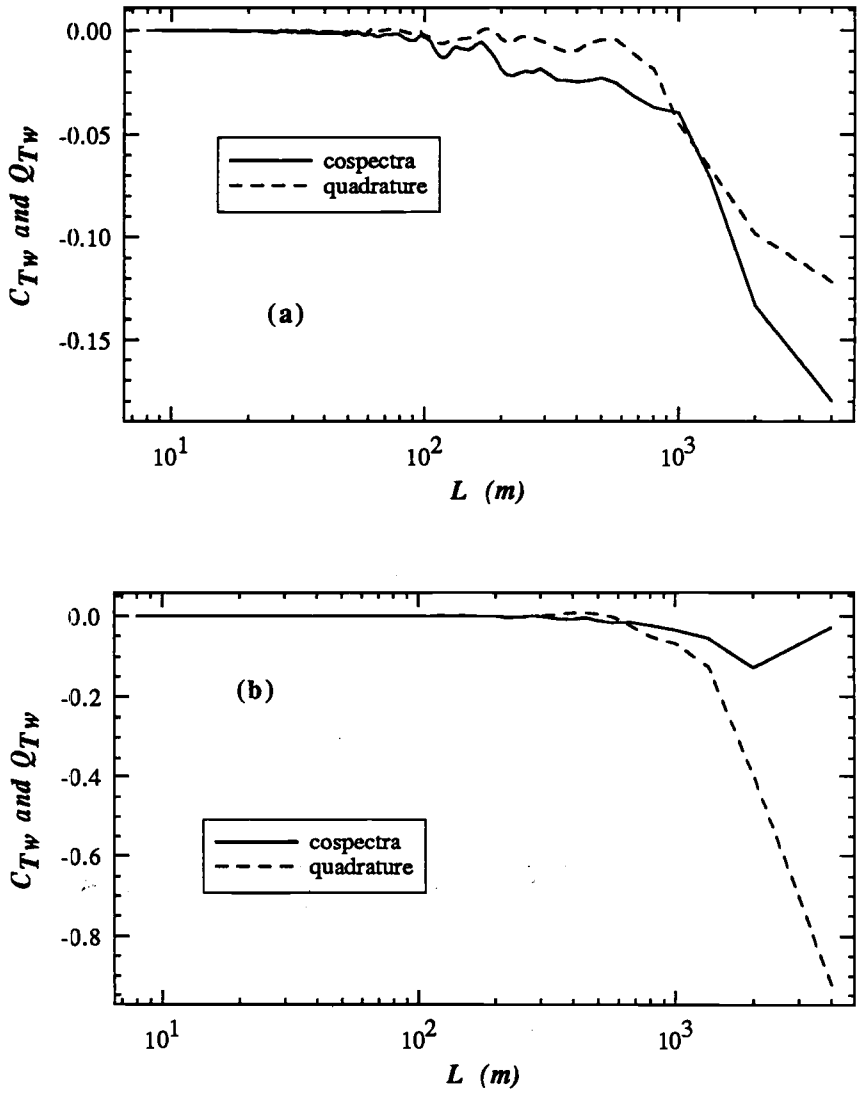

Fig. 2 Composite cospectrum (C_{Tw}) and Quadrature (Q_{Tw}) between T and w: (a) 6 May SESAME, (b) 5 May CABLE.

The quadrature is generally smaller than the cospectra for scales less than about 1 km for SESAME 6 May (Fig. 2a) and 700 m for CABLE 5 May (Fig. 2b). For 5 May CABLE, the quadrature is significantly larger than the cospectra for scales larger than about 800 m. The vertical velocity and temperature are expected to be more in-phase for the turbulent eddies and roughly 90 degrees out of phase for linear gravity waves. Hence, wave-like signature on scales of 1 km or greater observed in CABLE 5 May (Fig. 3b) appear to have characteristics of linear gravity waves.

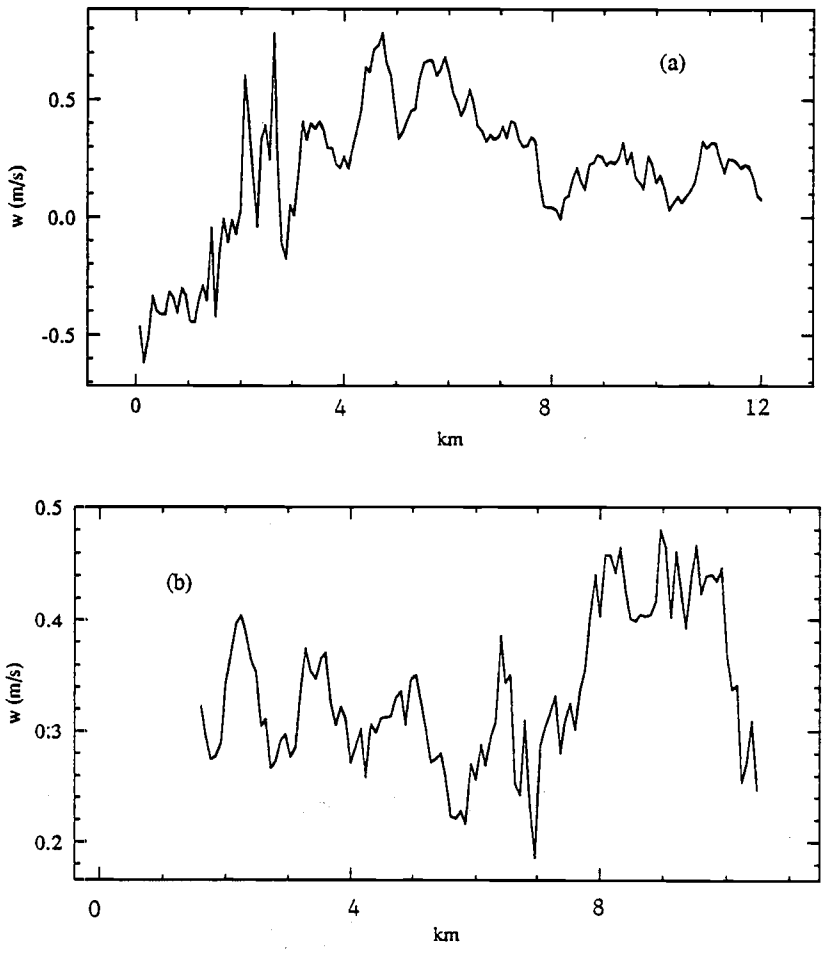

Fig. 3 A raw record of the vertical velocity: (a) 0745 - 0949 on 6 May SESAME, (b) 0611 - 0614 on 5 May CABLE.

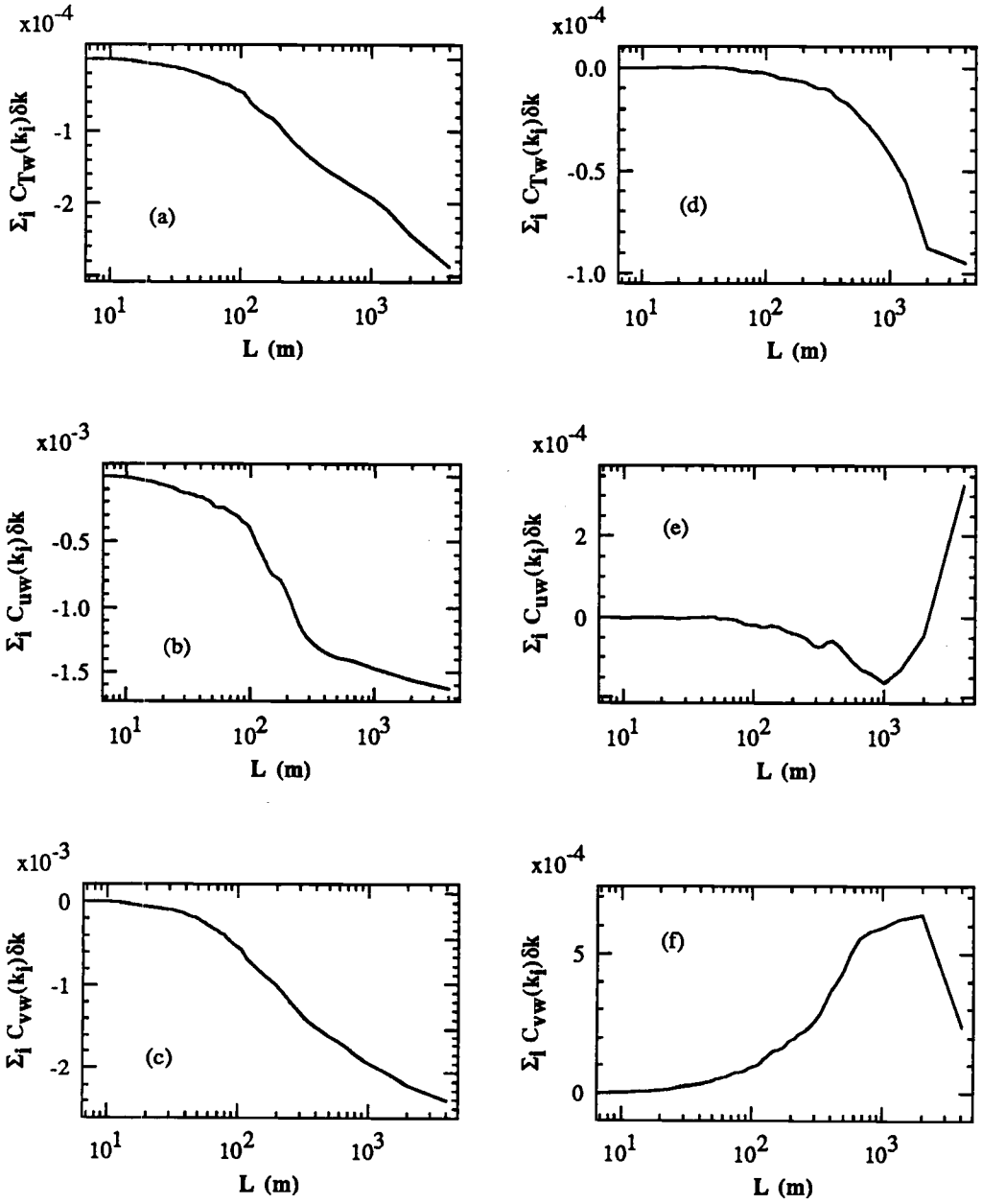

Fig. 4 Integrated cospectrum: (a), (b), (c) 6 May SESAME: (d), (e), (f) 5 May CABLE. $C_{\phi,\psi}$ is the cospectral density between ϕ and ψ, k_i is the horizontal wavenumber, and δk is the width of the wave band.

In SESAME 6 May, raw time series (Fig. 3a) also indicate wave like motions on scales of 1 km or greater but the quadrature and cospectra are of comparable importance. The gravity waves may be more complex in SESAME 6 May. In the following, we choose 840 m cutoff filterlength for high-pass filtering the CABLE 5 and 24 May data and 1 km cutoff wavelength for high-pass filtering the SESAME 6 May data respectively to include the most "turbulent-like" motions, even though the scale transition from turbulence to gravity waves cannot be precisely defined.

We estimate the net heat flux due to the motions in a bandwidth $k_1 \leq k \leq k_2$ from the cospectra as

$$\overline{Tw} = \int_{k_1}^{k_2} C_{Tw} dk \tag{1.1}$$

where C_{Tw} is the cospectral density between the vertical motion and temperature composited over the flight legs where k_1 and k_2 are the cutoff wavenumber for the high-pass filtering and the Nyquist wavenumber, respectively. The vertical flux of the horizontal momentum is similarly calculated from the composited cospectral density between the vertical and horizontal velocity components.

The signs of the net heat and momentum fluxes estimated by the integration of cospectra (1.1) generally agree with the sign corresponding to gradient transport for observed stratification and shear except for $\overline{uw}$ in CABLE 2 for scales larger than 2 km where sampling problems are expected to be large (Fig. 4). However, the heat flux generally becomes counter-gradient (upward) for scales less than 50 m for CABLE 2 and 20 m for SESAME 6 May. The significance of the countergradient heat flux can be found from the frequency distribution and the magnitude of the upward and downward heat fluxes in turbulent regions estimated in CABLE 2 (Fig. 5). Even though the regions of downward heat flux determines the sign of the flux for the record as a whole, the events of

upward heat flux appear almost as frequently as those of downward heat flux (Fig. 5a). The events for the upward heat flux carry a little less transport per event compared to the downward heat flux events (Fig. 5b,c). The corresponding correlation between vertical velocity and temperature ranges from 0.07 to 0.2. Consequently, the net heat flux is only a small difference between the upward and downward heat flux contributions to the analysis.

This countergradient heat flux apparently occurs as rebounding motions as overturned fluid elements accelerate back to their buoyancy equilibrium level. A schematic illustration of various stages of shear driven overturning is presented in Fig. 6. In the initial stage of shear driven overturning (Fig. 6a), fluid elements are displaced vertically from their buoyancy equilibrium level which results in downward heat flux.

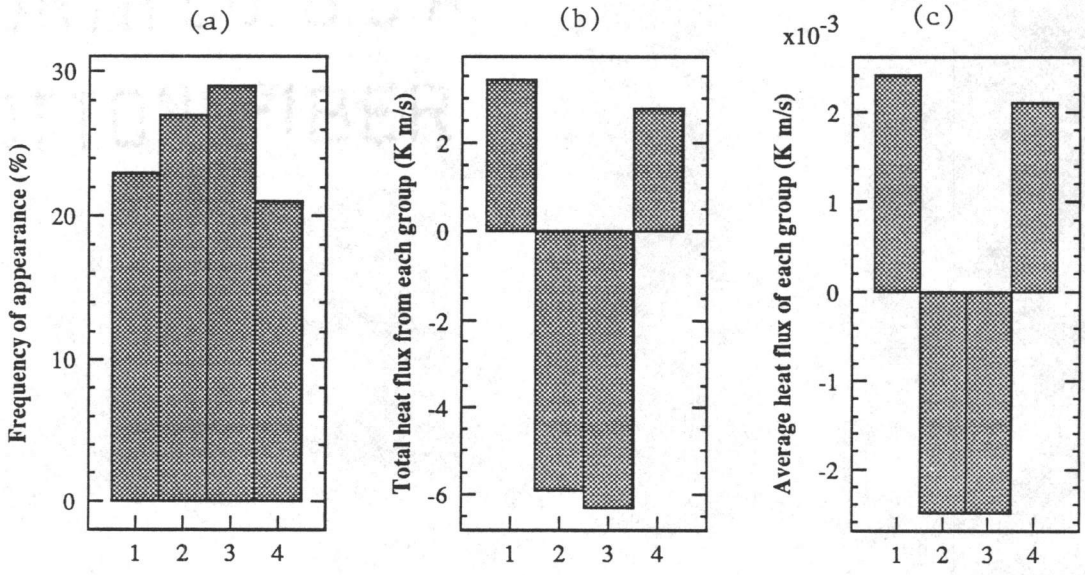

Fig. 5 Frequency of appearance (a), total (b) and mean (c) heat flux for each group of events. Horizontal axis indicates the groups. Group 1 is warm updrafts, group 2 warm downdraft, group 3 cold updraft, and group 4 the cold downdraft.

The local unstable stratification due to the displacement or overturning in turn generates small scale turbulence and transient upward heat flux at smaller scales (Fig. 6b). This possibility might explain the net upward heat flux on the smallest scales (Mahrt, 1985). Such recirculation of displaced fluid elements is also observed in laboratory experiments (Thorpe, 1973). As a result of mixing with environmental fluid the rebounding motion is generally weaker than the initial overturning so that the net heat flux remains downward. Finally, as the disturbance decays the heat flux becomes small (Fig. 6c).

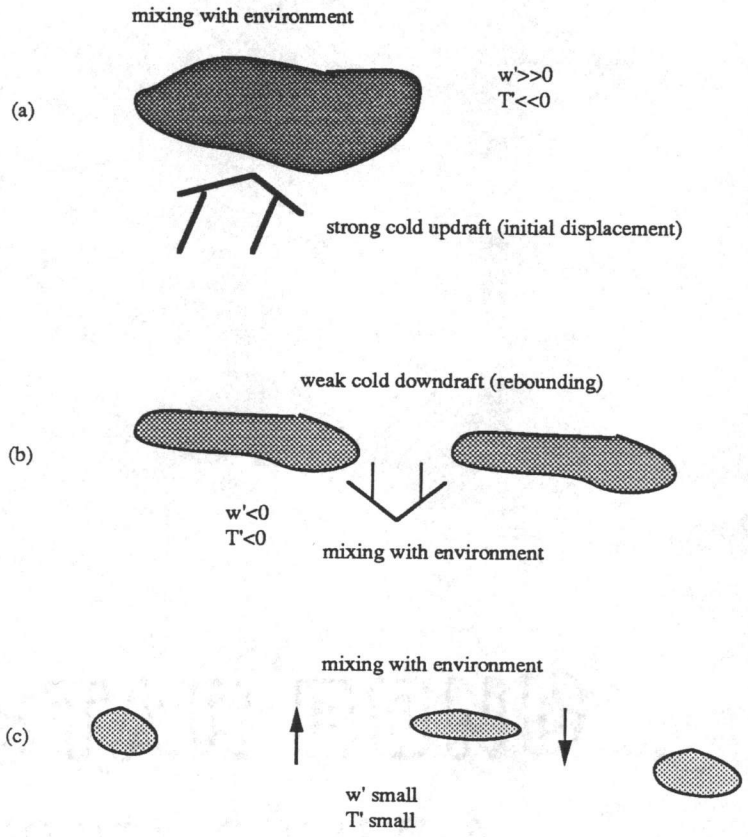

Fig. 6 Schematic illustration of mixing procedure of shear driven overturning: (a) Initial stage, (b) rebounding stage, (c) decaying stage.

2.1.3 Estimation of turbulent fluxes

After high-pass filtering to partially remove gravity waves and other larger scale disturbances, heat and momentum fluxes and the vertical velocity variance are calculated. Clear air turbulence is usually easily identified by the local maxima of the variance of high-pass filtered vertical velocity. Examples of vertical profiles of potential temperature, variance of high-pass filtered vertical velocity, and turbulent heat flux observed in CABLE 24 May over the ocean surface are presented in Fig. 7.

In CABLE 24 May the observed clear air turbulence is separated from boundary layer turbulence by a layer of relatively small vertical velocity variance (solid line, Fig. 7a). The bottom of the near-quiescent layer coincides with the capping inversion at the top of the boundary layer (dashed line, Fig. 7a,b). The variance of the high-pass filtered vertical velocity in the patches of clear air turbulence corresponds to an root-mean-square vertical velocity of 10 - 60 cm/s for the CABLE and 5 - 40 cm/s for SESAME 6 May. The magnitude of the vertical velocity associated with the stronger updrafts and downdrafts is usually an order of magnitude larger than the vertical velocity variance. Elevated maxima of downward turbulent heat flux can be found from the vertical profile of turbulent heat flux at the same level as the vertical velocity variance maxima (Fig. 7b).

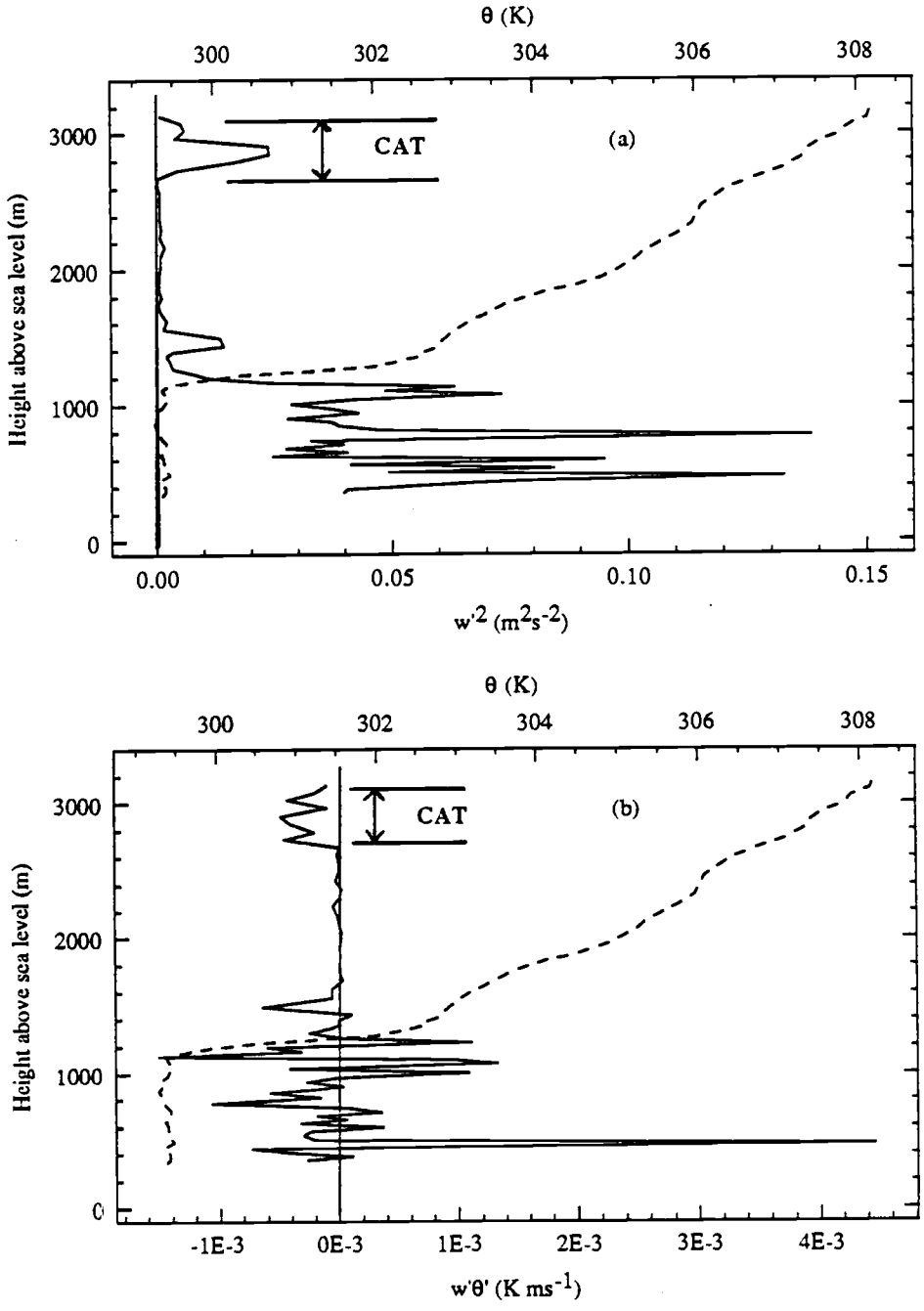

Fig. 7 Vertical profiles of (a) $\overline{w'^2}$ (solid line) and Θ (dashed line) and (b) $\overline{w'\theta'}$ and Θ where Θ is the mean potential temperature.

2.2 Flux formulation

2.2.1 Eddy diffusivities and the turbulent Prandtl number

In the data sets analyzed in this study, the relationship between the mixing length and the Richardson number shows less scatter compared to the relationship between the eddy diffusivities and the Richardson number. We therefore express the eddy diffusivity for heat (K_h) and momentum (K_m) as

$$\begin{aligned} K_h &= \ell_h^2 \left| \frac{\partial V}{\partial z} \right| \\ K_m &= K_h Pr \end{aligned} \tag{2.1}$$

where ℓ_h and Pr are the mixing length for heat and the turbulent Prandtl number assumed to be dependent on the stability of the mean flow.

For slant soundings, we approximate the gradient Richardson number (Ri) by the layer Richardson number (Ri_L) calculated as

$$Ri_L = \frac{g}{\Theta} \frac{\Delta\Theta \, \Delta z}{|\Delta V|^2} \tag{2.2}$$

where g is the gravity, $\Delta\Theta$ and ΔV are the differences of potential temperature and mean wind across the turbulent layer, Θ is the mean potential temperature, and Δz is the thickness of the turbulent layer. For the horizontal flight in SESAME 6 May, the gradients of the mean flow and the associated layer Richardson number are estimated from the adjacent flight levels. In the following discussions this layer Richardson number will be used as an estimate of the "gradient Richardson number".

To close the eddy diffusivity formulation (2.1), the turbulent mixing length and Prandtl number must be estimated from the observations. The eddy diffusivities for heat and momentum are computed from the observed fluxes and vertical variation of the mean flow as

$$K_h = -\frac{\overline{w'\theta'}}{\partial\Theta/\partial z} \tag{2.3a}$$

$$K_m = -\frac{\overline{u'w'}(\partial U/\partial z) + \overline{v'w'}(\partial V/\partial z)}{(\partial U/\partial z)^2 + (\partial V/\partial z)^2} \tag{2.3b}$$

where primed variables (u', v', w', θ') denote the turbulence-scale perturbation velocities and potential temperature. The mixing length for turbulent heat flux (ℓ_h) can be estimated from the observed eddy diffusivity for heat (2.3a) and mean shear as

$$\ell_h^2 = \frac{K_h}{|\partial V/\partial z|}. \tag{2.4}$$

Estimated mixing lengths decrease rapidly with increasing gradient Richardson number in the range $0 < Ri \leq 0.4$, then decrease more slowly for $Ri > 0.4$ (Fig. 8). The mixing length dependence on the Richardson number shows less scatter than this dependence for the eddy diffusivity for heat even though the mixing length is computed from the eddy diffusivity. The mixing length for momentum (not presented) shows more scatter than that for heat. Horizontal velocity fluctuation and momentum fluxes are complicated by pressure fluctuations while temperature is not. Therefore we compute the eddy diffusivity for heat and then compute the eddy diffusivity for momentum from the dependence of the eddy Prandtl number on the stability.

We represent the estimated mixing lengths in terms of an asymptotic mixing length at neutral stability $\ell_{0,h}$, as in Blackadar (1962), and a nondimensional function of the gradient Richardson number $\phi_h(Ri)$ so that

$$\ell_h(Ri) = \ell_{0,h}\phi_h(Ri) \tag{2.5}$$

The nonlinear least-squares fit of the observed mixing length can be approximated by $\ell_{0,h} \approx 52.5$ m and the nondimensional function of the gradient Richardson number

$$\phi_h(Ri) = \frac{e^{-8.5Ri} + 0.15/(Ri + 3.0)}{1.05}. \tag{2.6}$$

Due to the lack of data for small Richardson number range ($Ri < 0.2$), some uncertainty is expected in the estimated asymptotic mixing length. Previous model values of the mixing length at neutral stability above the boundary layer were specified to be 100 m or greater (Louis, 1979 and 1981), although such values were chosen without direct observational evidence. The first term in (2.6) represents the rapidly decreasing part of ℓ_h for the range $0 < Ri < 0.4$ while the second term in (2.6) represents the more slowly decreasing part of ℓ_h for the range $Ri \geq 0.4$. A similar two-regime relationship between Ri and the bulk dimensionless drag coefficient, which is the boundary layer equivalent of ϕ^2 in (2.5), is observed by Mahrt (1987).

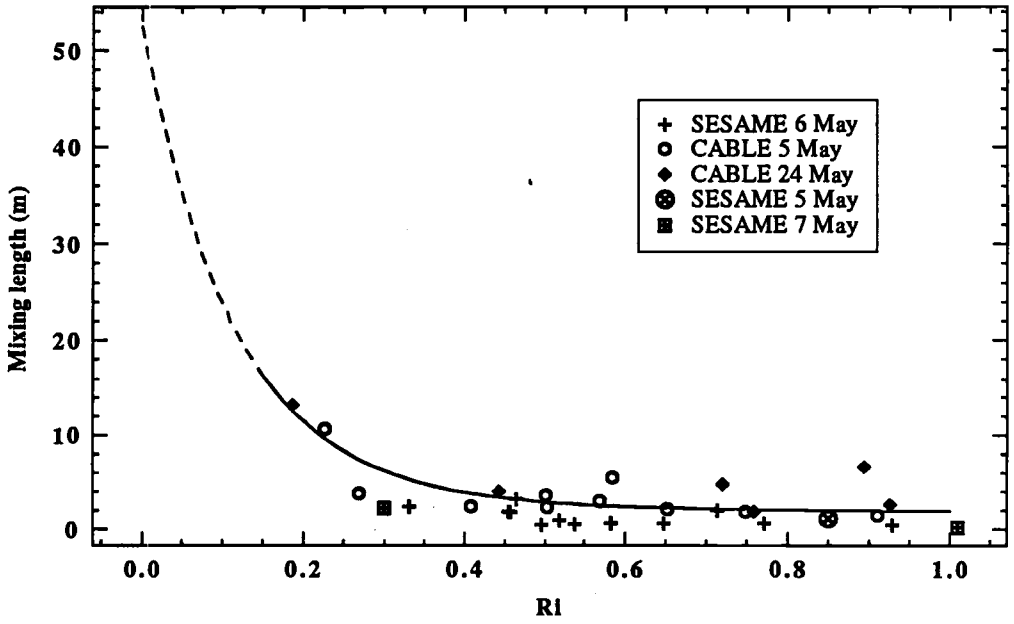

Fig. 8 The estimated mixing length and the least square fit (3.5) and (3.6) with $\ell_0 = 52.5$ m. The mixing length for SESAME 5 May is obtained from the composite profiles (Mahrt, 1985).

The estimated mixing lengths do not appear to be related to the thicknesses of the turbulent layers which vary from 20 m to several hundred meters between different flight legs perhaps suggesting that the vertical length scale of the turbulence is significantly smaller than the layer thickness. Conversely, the thicknesses of turbulent layers show little relationship to gradient Richardson numbers across turbulent layers which vary from 0.2 to 1.0. Hence, the thickness of the turbulent layer is probably not a suitable length scale for the analysis of clear air turbulence.

The turbulent Prandtl number (Pr) is estimated from the observed eddy diffusivities ($2.3a, b$) as

$$Pr = \frac{K_m}{K_h}. \tag{2.7}$$

The estimated Prandtl number from the current analyses is presented in Fig. 9 against Ri and compared with previous observations given in Wittich and Roth (1984). The dependence of the Prandtl number on the Richardson number shows considerable scatter especially at Richardson numbers greater than 0.4 (Fig. 9). The large scatter is partly due to large scatter in the values of the eddy diffusivity for momentum and the usual problems with statistics of ratios. The estimated Pr increases with increasing gradient Richardson number. This increase implies that the contribution of the pressure fluctuations to the vertical transport of horizontal momentum becomes more important as the stability of the mean flow increases. Increasing Pr with increasing Ri has also been observed in various laboratory experiments (e.g. Arya, 1975; Webster, 1964; Rohr *et al*, 1988) and in the lower atmosphere (Wittich and Roth, 1984).

The turbulent Prandtl number estimated from the present analyses are well represented with a linear function of the gradient Richardson number as

$$Pr(Ri) = Pr_0 + \alpha\, Ri, \tag{2.8}$$

where Pr_0 is the value of the turbulent Prandtl number at neutral stability.

A least square fit of the estimated turbulent Prandtl numbers yields $Pr_0 = 1.5$ and $\alpha = 3.08$, respectively (solid line in Fig. 9). This value of the asymptotic Prandtl number (Pr_0) is a little larger than some previous laboratory experiments which suggest $Pr_0 \approx 1$ (e.g. Arya, 1975; Mizushina *et al*, 1978). When $Pr_0 = 1$ is forced, a linear fit of the current results yields $\alpha = 3.84$ (dashed line in Fig. 9).

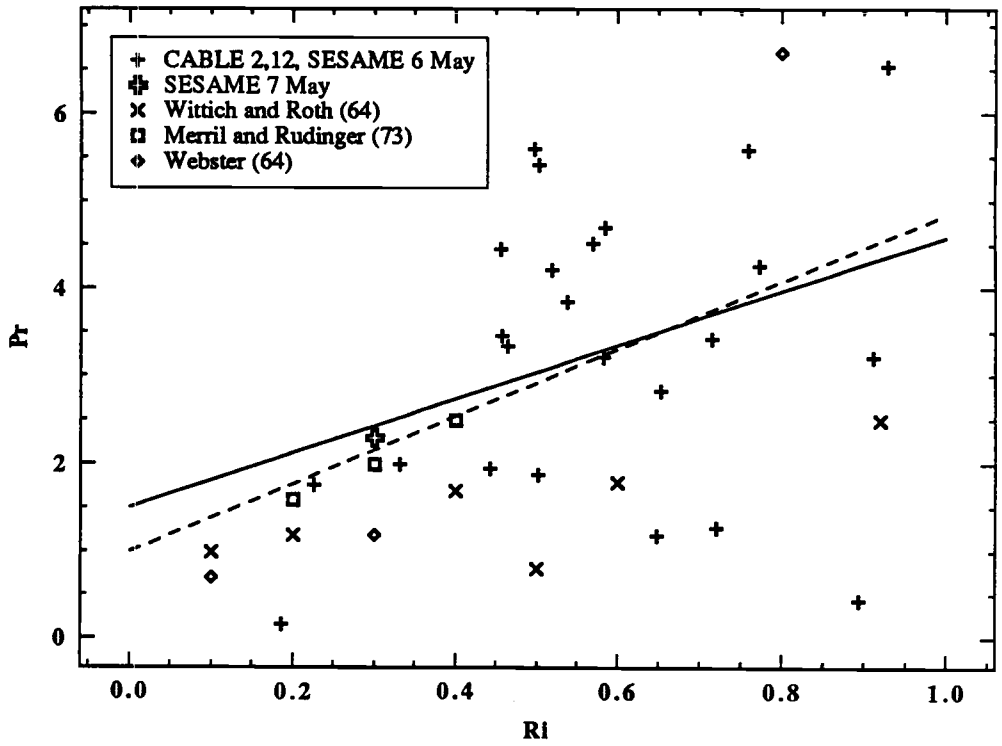

Fig. 9 The estimated turbulent Prandtl numbers and least-square fit with $Pr_0 = 1.5$ (solid line) and $Pr_0 = 1.0$ (dashed line). Data from other experiments are from Wittich and Roth (1984).

2.2.2 Comparison with the Louis model

The most used previous representation of mixing lengths above the boundary layer in large scale numerical models is based on a similarity relationship for the surface layer (e.g. Louis, 1979). Clear air turbulence is not directly influenced by the underlying surfaces so that the stability dependence computed from actual data (2.6) may be different from those based on observations in the surface layer. In the following, the eddy diffusivity formulation introduced by Louis (1979) will be compared against the current model.

The nondimensional function of Ri in the Louis model will be denoted by f_h, instead of ϕ_h in (2.5), and is of the form (Louis, 1979)

$$f_h(Ri) \;=\; [1 \;+\; 15\; Ri(1+5\; Ri)^{1/2}]^{-1/2}. \tag{2.9}$$

As a direct application of Blackadar (1976), the mixing length at neutral stability in the Louis model depends on the distance from the underlying terrain, which approaches a constant asymptotic value at high altitudes above the underlying surface. This asymptotic regime is analogous to (2.5) except we have estimated the nondimensional function of the Richardson number (3.6) from the data observed in the free atmosphere.

The nondimensional functions $\phi_h(Ri)$ and $f_h(Ri)$ both decrease with increasing gradient Richardson number, but $f_h(Ri)$ for the Louis model decreases more slowly than $\phi_h(Ri)$ based on observations (Fig. 10). Thus, for a given asymptotic mixing length, the current formulation will predict smaller eddy diffusivities than the Louis model.

The turbulent Prandtl number for the Louis model is obtained from (2.1), (2.5), and (2.7) as

$$Pr(Ri) \;=\; \frac{\ell_m^2}{\ell_h^2}(Ri) \;=\; \frac{\ell_{0,m}^2}{\ell_{0,h}^2}\frac{f_m^2(Ri)}{f_h^2(Ri)} \tag{2.10}$$

where ℓ_m, $\ell_{0,m}$, and f_m are the mixing length, the asymptotic mixing length, and a nondimensional function of the gradient Richardson number for the turbulent momentum flux, respectively. Defining a new dimensionless function of the gradient Richardson number $F(Ri)$, (2.10) can be simplified to

$$Pr(Ri) = Pr_0 F(Ri) \tag{2.11}$$

where Pr_0 is the turbulent Prandtl number at neutral stability defined as

$$Pr_0 = \frac{\ell_{0,m}^2}{\ell_{0,h}^2}. \tag{2.12}$$

We can obtain $F(Ri)$ from $f_h(Ri)$ and $f_m(Ri)$ given in Louis, (1979) as

$$F(Ri) \equiv \frac{f_m^2(Ri)}{f_h^2(Ri)} = \frac{1 + 15Ri(1+5Ri)^{1/2}}{1 + 10Ri(1+5Ri)^{-1/2}}. \tag{2.13}$$

For the comparison only, $Pr = 1$ at $Ri = 0$ is assumed for both the Louis and current models. The turbulent Prandtl number calculated from the Louis model (dashed line, Fig. 11) increases almost linearly with increasing gradient Richardson number, but faster than the current formulation based on the observations (solid line, Fig. 11). While the difference between the two formulations may not be significant compared to the large scatter in the data, both relationships predict that the Prandtl number becomes large, 5 or greater for strong stability. Therefore equating the eddy diffusivity for momentum to that for heat would seriously underestimate the momentum transport for large stability. For the numerical iteration in the next section, we employ formulations constructed in the previous subsection to model the clear air turbulence.

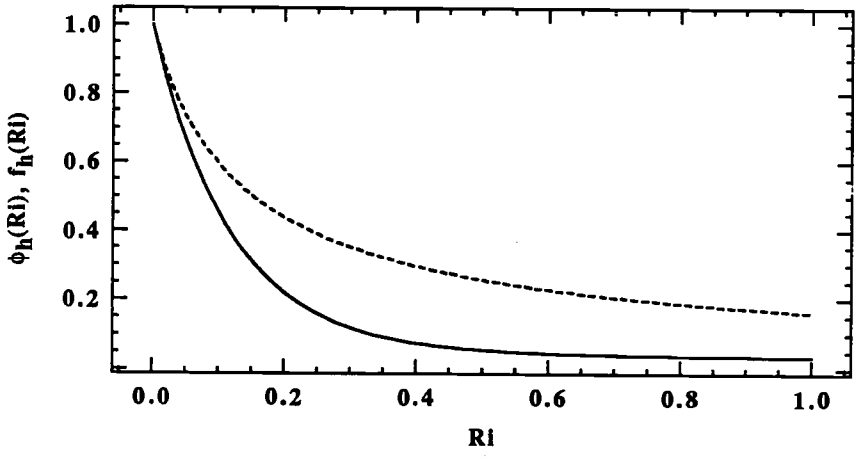

Fig. 10 Nondimensional functions of Ri from data analyses (solid line) and from the Louis model (dashed line) given by (3.6) and (3.8), respectively.

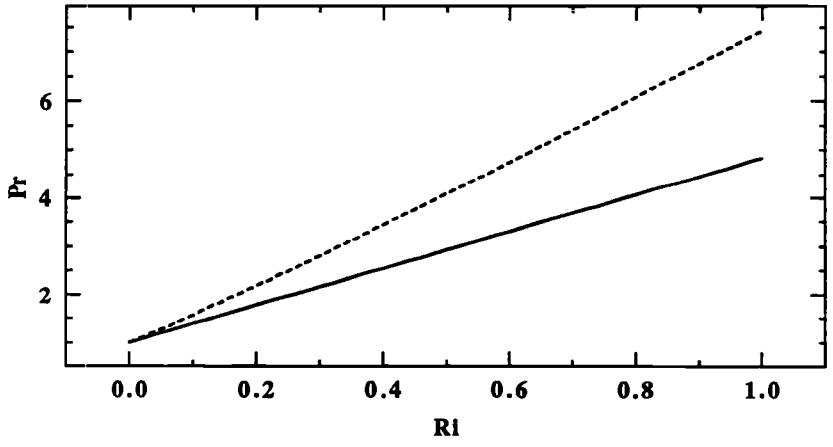

Fig. 11 Pr estimated from the current analyses (solid line) and from the Louis model (dashed line). $Pr_0 = 1$ is forced for each model.

2.3 Turbulence in the free atmosphere simulated with a one-dimensional model

The influence of clear air turbulence on the mean flow in the free atmosphere is now investigated using a one-dimensional numerical model. Turbulent fluxes in the free atmosphere are calculated with the eddy diffusivity and Pr using (2.1), (2.5), (2.6), and (2.7). Turbulent mixing in the boundary layer is calculated from the eddy diffusivity formulation based on boundary-layer similarity theory (Troen and Mahrt, 1986). The turbulence parameterization for the boundary layer and computational features of the column model are explained in detail in Ek and Mahrt (1990).

Initial conditions for model tests are obtained from the radiosonde sounding taken at 0600 LST, 19 May 1986 over Lubbone France, during HAPEX. To eliminate noise, the profiles of the wind, temperature, and mixing ratio obtained from the radiosonde sounding are simplified by assuming that the initial atmosphere can be approximately represented by four layers in which the mean flow varies linearly with height (Fig. 12a-c). The height and the magnitude of the maximum vertical velocity is obtained from the mesoscale analyses of Noilhan and Planton (1989). Then the large scale vertical velocity at each grid level is determined by linearly interpolating the maximum vertical motion toward the lower and upper boundaries of the domain where zero vertical motion is assumed. This condition ensures no vertical advection of heat and momentum through the upper boundary of the model domain.

A definitive comparison between the model and the observations is prevented by the failure to adequately determine the actual time- and height-dependent geostrophic wind and the horizontal advection. In the prototype experiment the geostrophic winds are assumed to be time- and height-independent

at all levels with $(u_g, v_g) = (3.5,3.5)$ ms^{-1} and no subsidence in the model domain. In discussing the model results, we will focus on clear air turbulence above the nocturnal boundary layer associated with the development of the low level nocturnal jet and weak stratification in the residual layer. The residual layer is a layer of weak stratification above the nocturnal boundary layer and is the remnant of the mixed layer of the previous day (Stull, 1990).

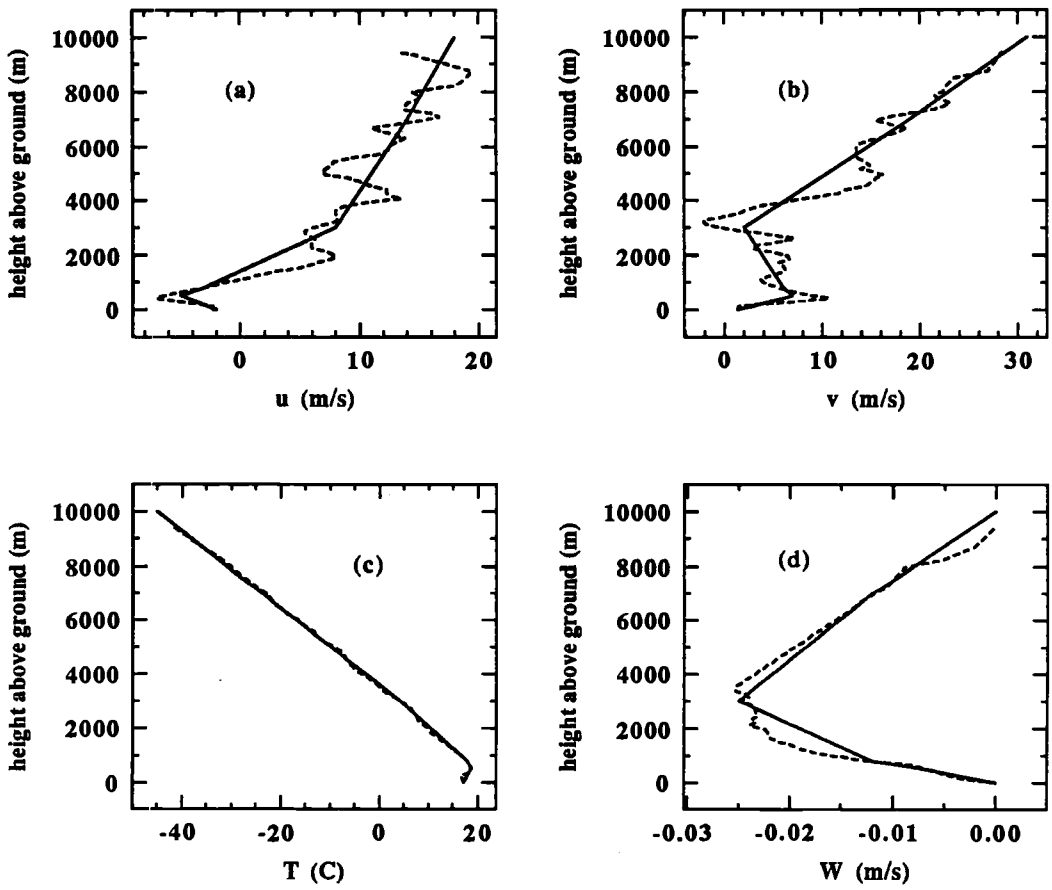

Fig. 12 Radiosonde sounding at 0600 on 19 May 1986 over Lubbone, France (dashed line) and the model input (solid line).

2.3.1 Diurnal variation of the simulated flow

The diurnal variation of the wind, potential temperature, and eddy diffusivity for heat simulated without free atmospheric mixing and large scale subsidence are shown in Fig. 13. Evolution of the model atmosphere is governed mainly by the growth and decay of the mixed layer and attendant inertial oscillation. Such features of the simulated flow are expected to dominate in the absence of the radiative heat transfer and horizontal and vertical advection. Then the large-scale pressure gradient and turbulent diffusion are the two major terms responsible for the evolution of the simulated flow.

During the collapse of daytime boundary layer, the boundary layer depth decreases from 1.6 km above the ground at 1700 LST to near 200 m at 2000 LST. The eddy diffusivity rapidly decreases with time (Fig. 13d) and the inertial oscillation penetrates to a much lower level, just above the nocturnal boundary layer. This leads to the development of a low-level jet just above the surface inversion layer (Fig. 13a,b). The strongest low-level jet appears in the early morning (0600) with maximum wind speed reaching 1.6 times the geostrophic wind.

The residual layer of weak stratification appears between the top of the nocturnal surface inversion layer and the top of the pre-existing daytime mixed layer (Garrat 1985, Stull and Driedonks, 1987). The residual layer is characterized by weak interior stratification with temperature inversion and strong shear at the top and bottom of the layer (Fig. 13a-c). The weakly stratified layer observed in the early morning of 7 May 1979 in SESAME (Fig. 14a) and in the night between days 33 and 34 in Wangara Experiment (André *et al*, 1978) may be good examples of the residual layer. Other possible examples of the residual layer can be found from the potential temperature soundings reported

in Mahrt *et al* (1979), Hsu (1979), and Estournel (1986) although they were not explicitly discussed as residual layers in those studies.

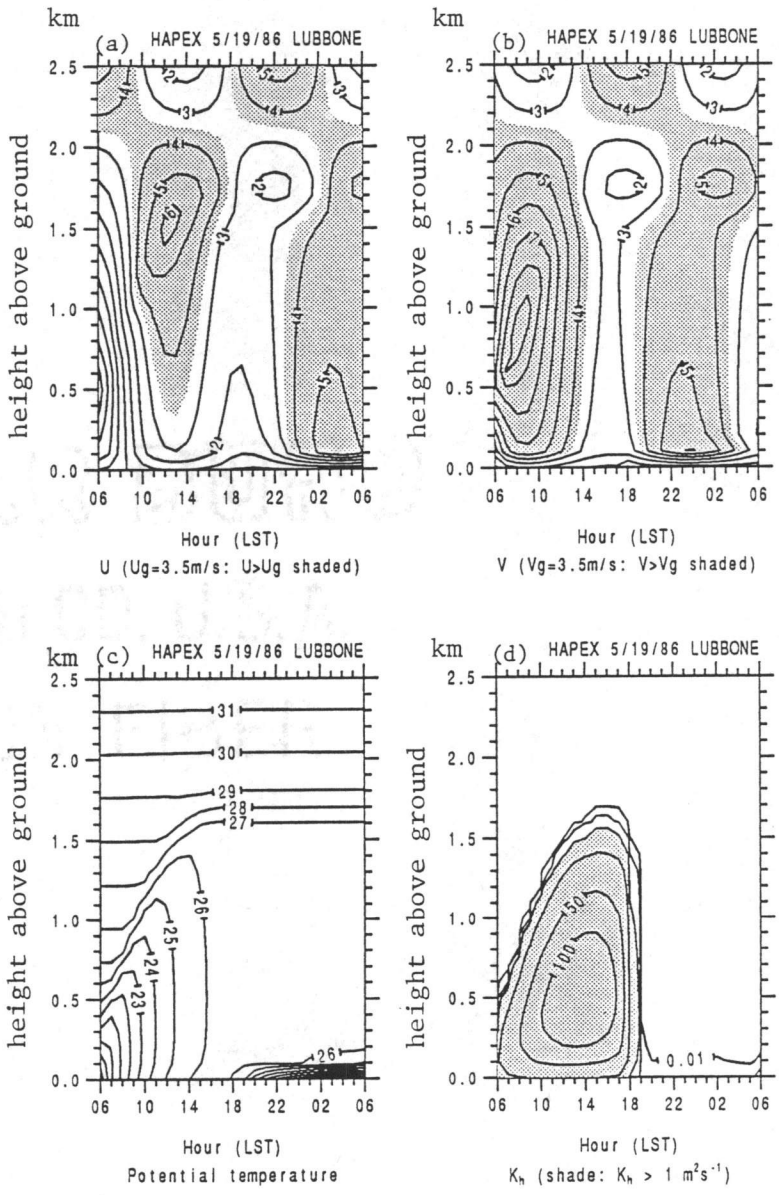

Fig. 13 Model-estimated diurnal variation of: (a) u, (b) v, (c) θ, and (d) K_h. $u > 5$ m/s, $v > 5$m/s, and $K_h > 1$ m^2/s are shaded.

Shear at the bottom of the residual layer is due to the development of a low-level jet while shear at the top of the residual layer results from an almost separate evolution of the flows across the top of the daytime boundary layer. Development of a low-level jet due to the inertial oscillation and and frictional decoupling of the flow in the vicinity of the top of the nocturnal boundary layer is well explained in previous studies (e.g., Wittich and Roth, 1984). The shear at the top of the residual layer in the current study can also be explained as a consequence of the inertial oscillation and frictional decoupling of the flow in the daytime mixed layer. As the daytime mixed layer collapses flow in the residual layer experiences less friction and begins inertial oscillation but with different phase from the flow above the daytime mixed layer, which in turn cause strong shear at the top of the residual layer.

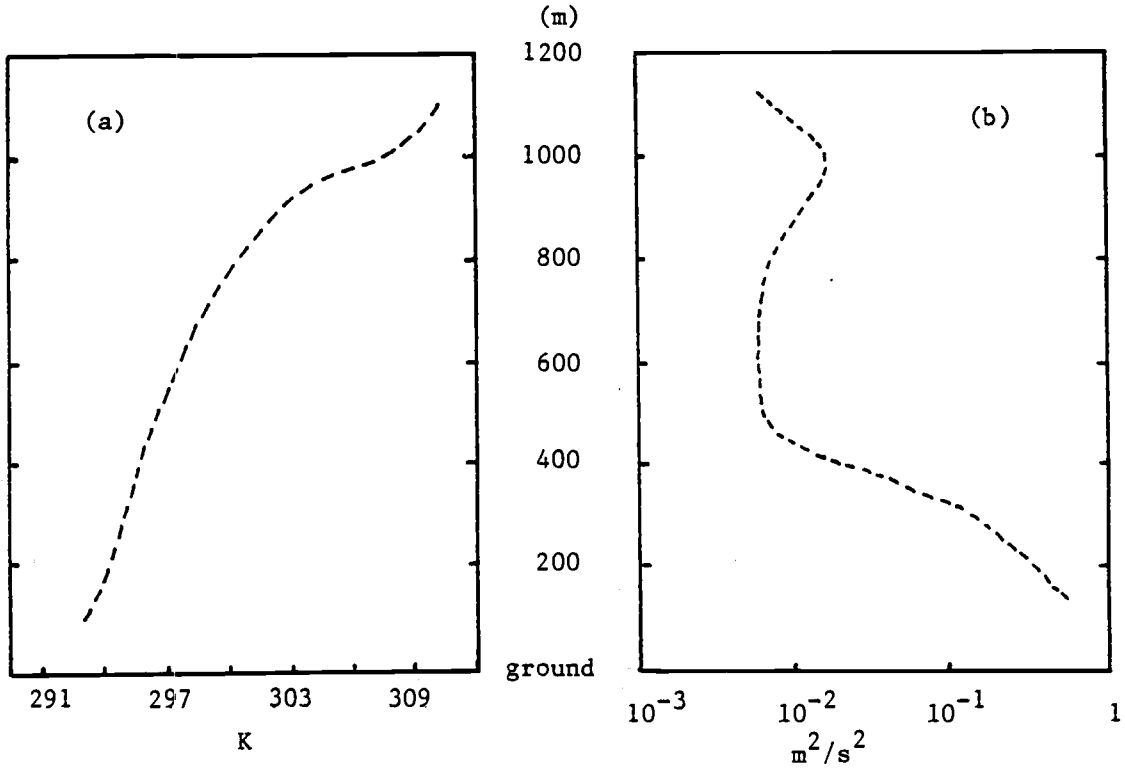

Fig. 14 Profiles of (a) θ, and (b) TKE observed at 0640 on 7 May in SESAME (after Lenschow *et al*, 1987).

2.3.2 Turbulent diffusion in the free atmosphere

The modelled clear air turbulence in the low level nocturnal flow appears to be closely related to the development of strong shear due to the inertial oscillation in the residual layer, especially at the top and bottom of the residual layer. Immediately after the collapse of the daytime mixed layer, before the low-level jet develops, the strongest turbulence above the boundary layer occurs near the top of the residual layer (Fig. 15a). By early morning in this model run, when the low-level jet reaches its full strength, the eddy diffusivity maximum is located just above the low-level wind maximum with a lesser peak near the top of the residual layer (Fig. 15b). A local turbulence maximum near the top of the residual layer also appears in the early morning profile of the turbulence kinetic energy (TKE) profile on 7 May 1979 SESAME (Fig. 14b) and in the model results of André *et al* (1978) and Garratt (1985). Turbulence at the top of a less stable layer above the nocturnal surface inversion layer also has been reported by Lu *et al* (1983) from tower and acoustic sounder data obtained from the Boulder Atmospheric Observatory. However its relationship to the simple concept of the residual layer is complicated by horizontal advection of temperature at the observational site. An inferred maximum of turbulence near the low-level jet has been observed by André and Mahrt (1982) and is suggested by André *et al* (1978) and Garratt (1985) in their modelling studies.

Modelled maxima of eddy diffusivity outside the nocturnal boundary layer appear at the upper and lower edges of the wind maximum of the nocturnal jet while the eddy diffusivity becomes small in the core of the low-level wind maximum (Fig. 15b). Even though turbulence in the free atmosphere does not significantly influence the bulk simulated flow, for this modelled case, it becomes locally important in layers where the flow varies rapidly in the vertical. For

example, turbulence mixing reduces the mean shear near the top of the residual layer by early morning (Fig. 16a,b). The smaller eddy diffusivity for heat (large Prandtl number) fails to significantly modify the profiles of potential temperature profiles (Fig. 16c).

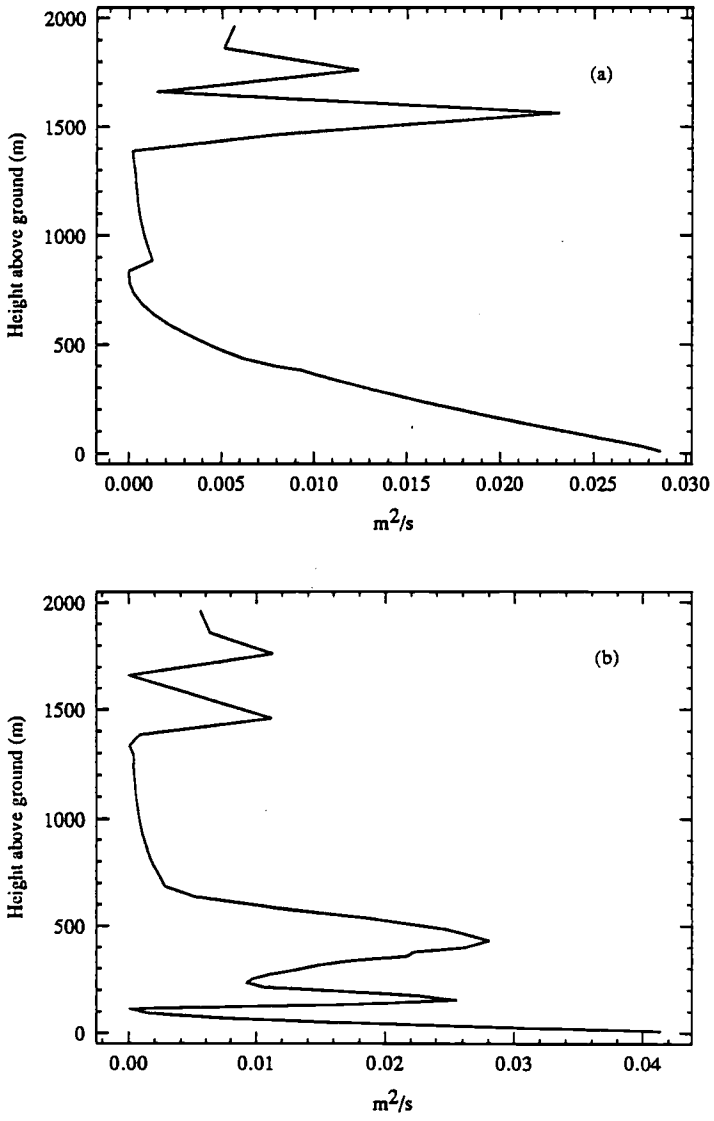

Fig. 15 Model-estimated vertical profiles of K_h at (a) 1900 LST and (b) 0500 LST. The mixing formulation of Troen and Mahrt (1986) is used within the boundary layer.

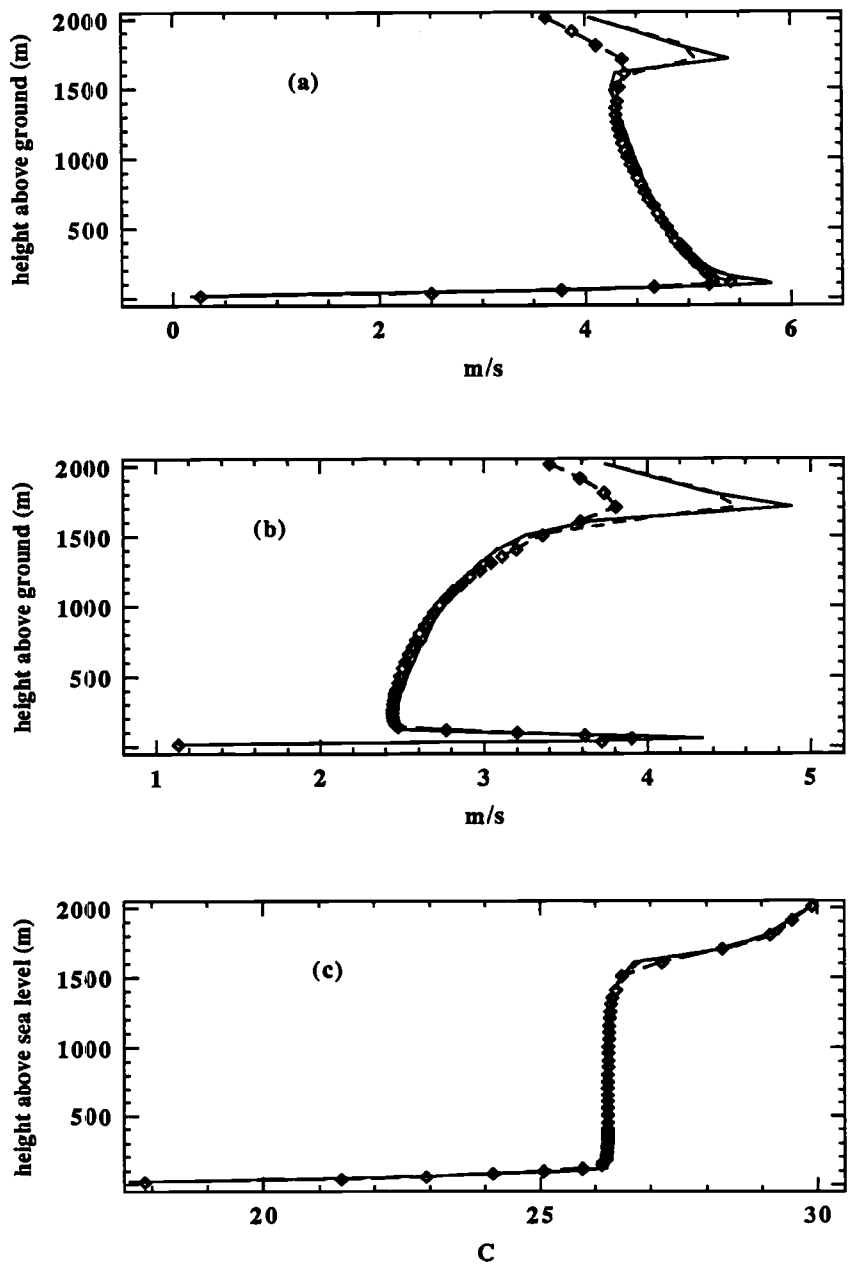

Fig. 16 Model-estimated vertical profiles of (a) u, (b) v, and (c) θ at 0500 LST. Solid line is without free atmospheric mixing, dashed line is with free atmospheric mixing, and dashed line with open diamond is the simulation with enhanced mixing length ($\ell_0 = 250$ m)

2.3.3 Enhanced eddy diffusivity

The above formulation of the eddy diffusivities in the free atmosphere considers only the fluxes due to turbulence scale motions. In large-scale numerical models, where the typical horizontal resolution may be on the order of several hundred kilometers, the *subgrid* scale transport includes motions larger than turbulent eddies. Consequently the magnitude of the subgrid-scale flux may increase with decreasing horizontal resolution. The fluxes computed from observations in this study may underestimate the subgrid scale transport since it does not include scales larger than 1 km. There is no theoretical basis to represent fluxes due to motions larger than turbulence scales by the flux-gradient relationship, but it is usually thought that the subgrid scale flux would increase as the model resolution decreases. In addition we cannot rule out unknown instrumentation problems such as phase errors which act to reduce the observed flux.

The larger values of the mixing length used in previous models have been obtained to provide sufficient mixing to correct for perceived model deficiencies. The larger values of mixing may be needed to control numerical problems, compensate for lack of gravity wave transport, or other model deficiencies in which case the "best" value of the mixing length depend more on model characteristics than on the strength of actual clear air turbulence.

To study the sensitivity of the flow evolution to the modelled strength of the turbulence we arbitrarily increase the asymptotic mixing length in (2.5) to $\ell_0 = 250$ m with the same functional dependence of ϕ_h on the gradient Richardson number (2.6). This modification produces 25 times larger eddy diffusivity. Asymptotic mixing lengths of such magnitude are within the range of those in some large scale numerical models. For example, Louis (1981) used

asymptotic mixing lengths ranging from 150 to 450 m.

The enhanced eddy diffusivity substantially reduces the rapid variation of wind near the top of the residual layer (Fig. 16a,b). It also somewhat reduces the magnitude of low level jet, but not as significantly as near the top of the residual layer. The enhanced mixing still fails to stratify the interior of the residual layer. This again suggests that observed stratification of the residual layer may be due to clear air radiative cooling and temperature advection, neglected in the present model.

2.3.4 Turbulence in the upper part of nocturnal PBL

Models based on boundary layer similarity appear to adequately approximate the weakly stratified boundary layer, but they poorly describe the very stable boundary layer (Mahrt, 1985). For example, the formulation for the stable boundary layer used in the current model fails to represent the effect of strong shear in the upper part of the nocturnal surface inversion layer associated with the overlying low-level jet. In particular, the nocturnal boundary layer may assume an upside down structure with the main source of shear generation occurring at the top of the surface inversion layer.

Boundary-layer similarity theory is based on the assumption that the vertical length scale of large boundary layer eddies is related to the depth of the boundary layer and height above the ground. In the very stable boundary layer, vertical movement of air is restricted and the turbulent eddies can not extend over the entire depth of the boundary layer (Nieuwstadt, 1984). Turbulence is often intermittent in the upper part of the very stable boundary layer. It may be generated more by local shear and become independent of surface stress.

Local generation of the turbulence in the upper part of the stable boundary layer is well approximated by the scaling in terms of a *local* Monin-Obukhov

length (Nieuwstadt, 1984). One shortcoming of the local scaling is that it requires the knowledge of the vertical profiles of shear stress and heat flux including the flux values at the top of the boundary layer which has been assumed to be zero. However, the observed flux at the top of the boundary layer is significant when the mean shear is locally important. Thus the model of Nieuwstadt (1984) can not be used, in general, to predict profiles of flux for the case of a significant low level jet.

In an attempt to consider local generation of turbulence in the upper part of the nocturnal boundary layer, the current free atmospheric mixing model has been merged with the upper part of the modelled nocturnal boundary layer. It is arbitrarily assumed that boundary layer similarity is always valid in the lower 30 % of the stable boundary layer and that local shear and stratification may potentially determine turbulent mixing in the upper 70 % of the modelled boundary layer. In this layer, eddy diffusivities are estimated as the maximum of the boundary layer parameterization or the clear air turbulence prediction, whichever yields the larger value.

For the clear air prediction, the asymptotic mixing length $\ell_{0,h}$ in (2.5) for the upper part of the boundary layer is not allowed to exceed (kz) where k is the von Karman constant assumed to be 0.4 and z is the distance from the surface. That is, *free* eddies attempting to become larger than kz would be constrained by the surface. In actuality the limiting mixing length should be less than kz but there are no observations to study the development of turbulence from elevated shear layers which subsequently becomes influenced by the ground. After determining the mixing length, the clear air eddy diffusivity for heat in the upper part of the surface inversion layer is computed. The eddy diffusivity for momentum is then computed from the turbulent Prandtl number (2.7).

With development of the low level jet, the eddy diffusivity estimated by the clear air prediction generally exceeds the eddy diffusivity estimated from the boundary-layer similarity in the upper part of the surface inversion layer, especially late in the evening when shear near the top of the surface inversion layer becomes large. As a result, the maximum eddy diffusivity in early morning occurs in the upper part of the nocturnal boundary layer instead of near the ground surface (Fig. 17a). This upside down structure is observed in Mahrt (1985).

The locally generated turbulent mixing in the upper part of the nocturnal boundary layer reduces the low-level jet speed maximum and stratification near the top of the surface inversion layer leading to a slight decrease of stability (fig. 17b-d) which results in the nocturnal boundary layer about 12 % deeper than that simulated by the conventional boundary layer similarity model. Low-level jet maximum appears at higher altitude. André *et al* (1978) attribute the lifting of the low-level jet to the enhanced surface friction, but this study suggests that local shear generation of turbulence in the upper part of the nocturnal boundary layer can cause similar lifting of the low-level jet altitude. Although the free atmospheric prediction of mixing is based on observations above the nocturnal boundary layer, there does not exist sufficiently accurate data for the time-dependent geostrophic wind to definitely test the evolution of the boundary-layer-free atmospheric system. The locally generated turbulence increases the nocturnal minimum surface temperature by about 0.4 deg C. Overestimation of surface cooling has been a systematic deficiency of boundary layer models applied to very stable conditions (Ruscher, 1987).

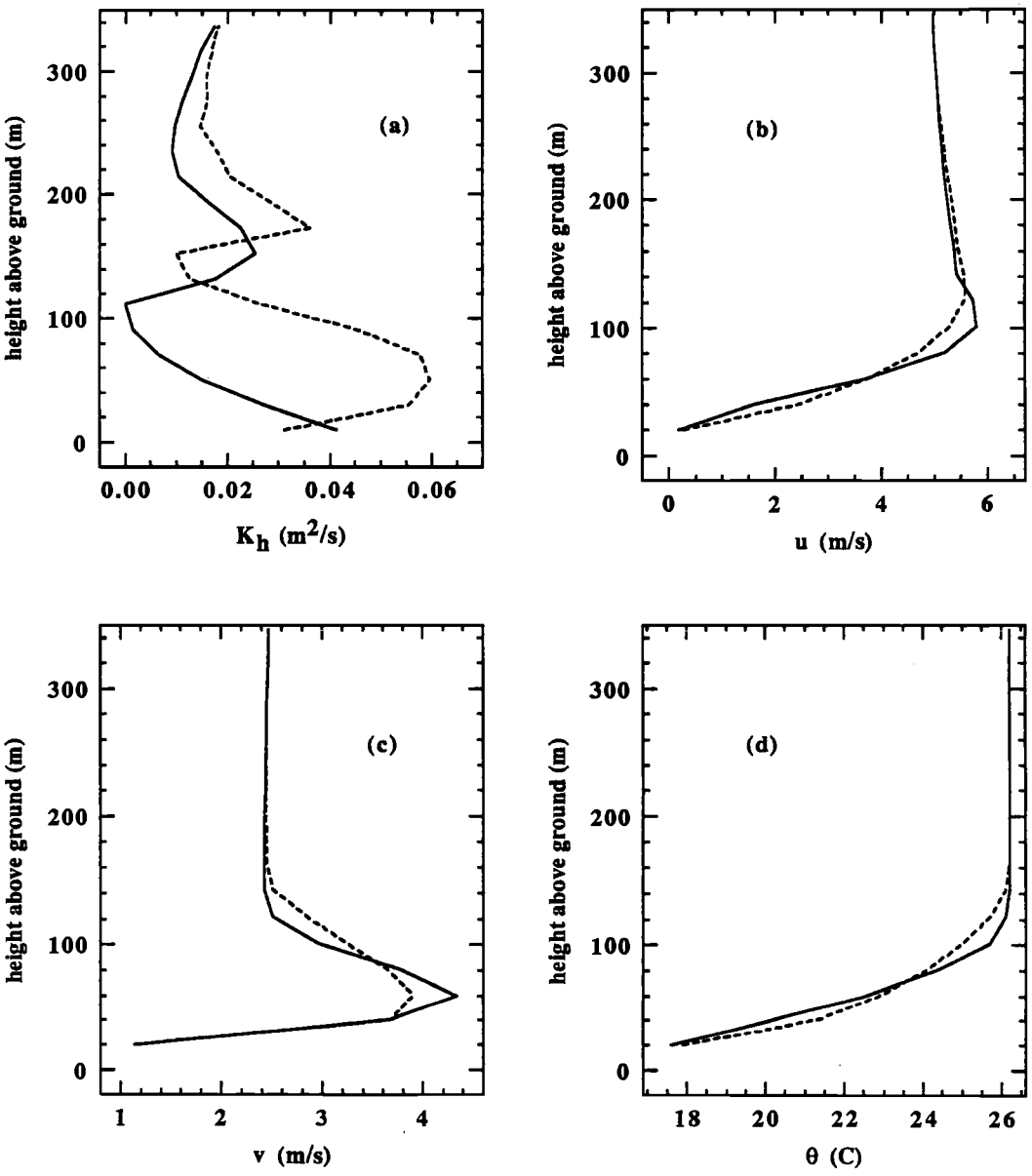

Fig. 17 Model-estimated vertical profiles of (a) K_h, (b) u, (c) v, and (d) θ at 0500 LST. Solid lines are the results from the boundary layer similarity theory and dashed lines are the results when local generation is allowed in the upper part of the stable boundary layer.

2.3.5 Influence of large-scale subsidence

Despite the occurrence of significant eddy diffusivities at the top and bottom of the residual layer, significant stratification does not develop within the modelled residual layer and the nearly-well-mixed structure of potential temperature is maintained until the following morning (Figs. 13d and 16c). Layers with relatively weak stratification are occasionally observed above the nocturnal surface inversion layer, but such layers usually do not maintain a completely well mixed structure (Fig. 14a, also see Lu *et al*, 1983). Thus, the lack of the development of stratification and shear in the residual layer in the current model might indicate the possible significance of radiative heat transfer, advection, and baroclinicity on the evolution of the nocturnal residual layer or might indicate underestimation of mixing. Radiative heat transfer usually exceeds the turbulent heat transfer near the top of the surface inversion layer and within the residual layer, even in the presence of a low-level jet (André and Mahrt, 1982). Subsidence also plays an important role which is the main subject of this subsection.

The influence of large-scale subsidence on the nocturnal flow is investigated by imposing the mean vertical motion (Fig. 12d) throughout the model integration during the day and night. For comparison, another model run is made without nocturnal large-scale subsidence in which case the large scale vertical motion imposed during the daytime is set to be zero beginning at 1900 LST. With this comparison, we isolate the influence of subsidence on the residual layer.

The large-scale subsidence enhances the shear and stratification in the residual layer (Fig. 18). The net result of enhanced shear and stratification is to stabilize the residual layer, especially in the upper part of it which results

in the reduction of the thickness of the residual layer to less than one half of that without subsidence (Fig. 18c). A major difficulty for modelling the residual layer now emerges. The depth of the layer is sensitive to even modest values of subsidence yet subsidence cannot be accurately estimated from observations.

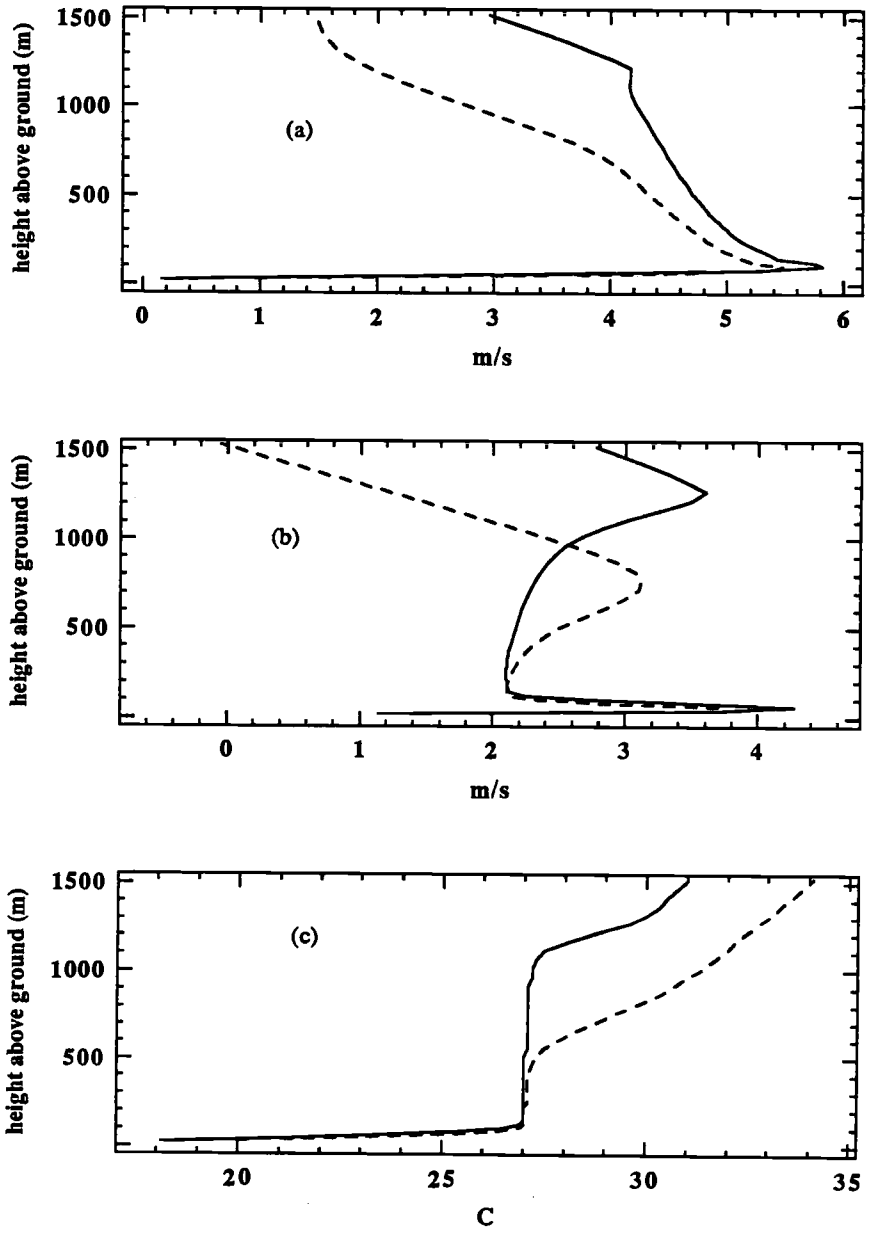

Fig. 18 Vertical profiles of (a) u, (b) v, and (c) θ in the presence (dashed line) and in the absence (solid line) of subsidence.

2.3.6 Influence of geostrophic wind shear

Mean shear and resulting turbulent mixing in the residual layer can be enhanced by baroclinicity of the large-scale flow. The influence of geostrophic wind shear on the generation of turbulence is tested by imposing the vertically-varying geostrophic wind profile shown in Fig. 19. Horizontal advection of temperature implied by the geostrophic wind shear is neglected. The large-scale subsidence is also neglected throughout the simulation. Details of the simulated flow will depend on the shape of each geostrophic wind profile, hence the results presented below represents only one simple example.

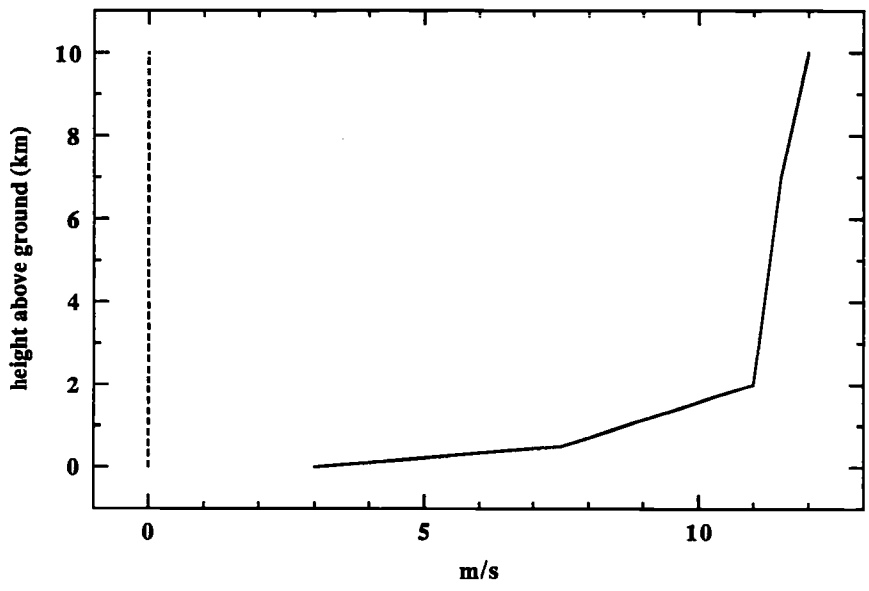

Fig. 19 Vertical profiles of the geostrophic wind used in the baroclinic run: U_g (solid line) and V_g (dashed line).

With the imposed geostrophic wind shear (Fig. 19), turbulent mixing significantly alters the shape of the low level flow, especially near the top of the nocturnal boundary layer (Fig. 20). The u wind component maximum near 50 m above ground, which appears in the run without free atmospheric diffusion, almost disappears when the clear air prediction of turbulent mixing is included in the free atmosphere (Fig. 20a). Also, the sharp vertical variation of the u wind component near 500 m above ground is greatly reduced by the mixing. The sign of the vertical shear of v wind component changes to the opposite sign due to mixing in the free atmosphere (Fig. 20b).

When local generation of turbulence in the upper part of the stable nocturnal boundary layer is included together with the eddy mixing in the free atmosphere, vertical variations of the wind and potential temperature near the top of the nocturnal stable boundary layer are further smoothed (Fig. 20). Nocturnal boundary layer is warmed by the mixing in the free atmosphere and in the upper part of the nocturnal boundary layer. Compared to the case where mixing in the free atmosphere and in the upper part of the nocturnal boundary layer is absent, the warming at 20 m above the ground (lowest model level) is about 0.6 deg C when only mixing in the free atmosphere is considered and is almost 1.9 C deg when additional mixing in the upper part of the nocturnal boundary layer due to local shear is considered (Fig. 20c).

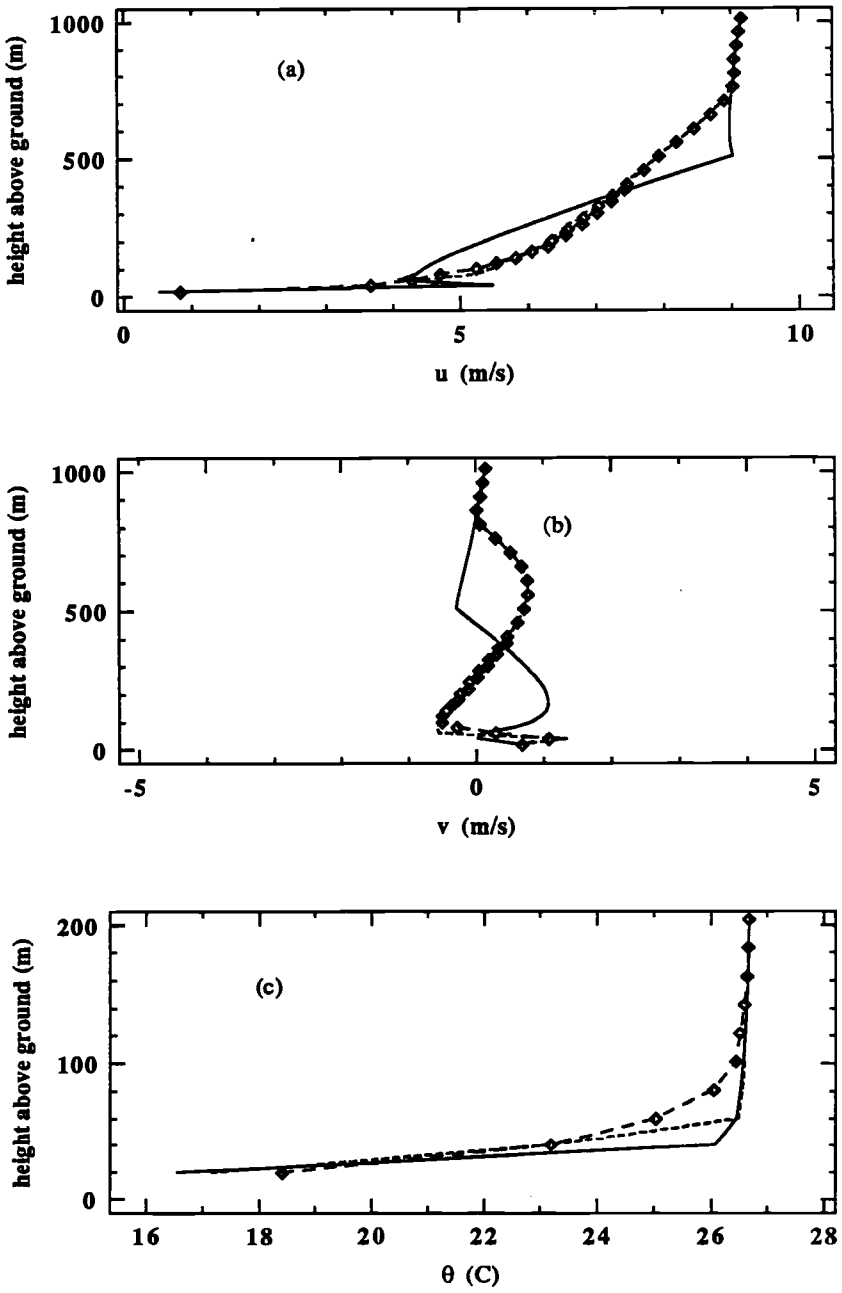

Fig. 20 Vertical profiles of (a) u, (b) v, and (c) θ at 0500 LST simulated with geostrophic wind shear with (dashed) and without (solid) mixing in the free atmosphere, and with local generation of mixing in the stable boundary layer (dashed line with open diamonds).

The enhanced turbulent mixing above the boundary layer in the presence of strong geostrophic wind shear deepens the nocturnal boundary layer (Fig. 21) by 50 - 100 % compared to the depth of the nocturnal boundary layer without turbulent mixing in the baroclinic free atmosphere. The inclusion of locally generated turbulent mixing in the upper part of stable boundary layer results in deeper nocturnal boundary layer later when the nocturnal boundary layer grows following the development of the low level jet.

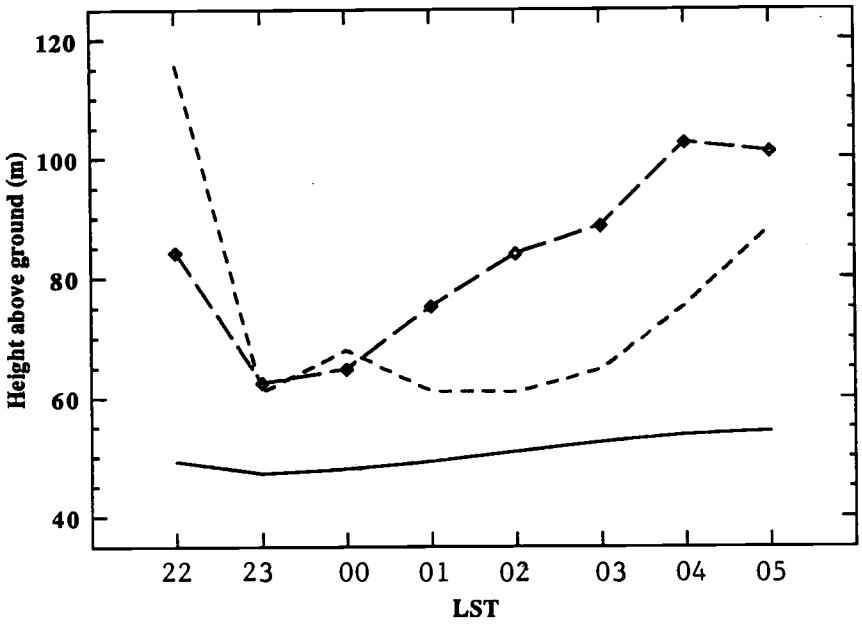

Fig. 21 Variation of the simulated nocturnal boundary layer top with (dashed line) and without (solid line) free atmospheric mixing, and additional local shear generation of turbulent mixing in the upper part of stable boundary layer (dashed line with open diamond).

3. Momentum Transport by Gravity Waves

3.1 Disturbances observed during ALPEX

In this section, we study the main characteristics of the disturbances observed over the coastal range of Northern Yugoslavia on 6 March 1982. Aircraft legs were flown in the North-east to South-west directions at about 2.4, 2.7, 3.3, 3.7, and 4.4 km above sea level. See Mahrt and Gamage (1987) and Smith (1987) for the description of the flow on this day.

In the following discussions, the x-coordinate is parallel to the aircraft flight legs directed toward the southwest, and the y-coordinate is in the direction to the right of the positive x-direction (toward the northwest). The u and v components of a wind are in the positive x- and y-directions, respectively, and w denotes vertical velocity. In this system of coordinates, the low-level mean flow is approximately in the positive x-direction, which is almost perpendicular to the underlying topographical ridge. Hence horizontal scales depicted from analyses performed in this system of coordinates will closely represent "true" length scales associated with gravity waves generated by two-dimensional ridge whose phase lines in a horizontal plane are approximately parallel to the underlying ridge.

3.1.1 Horizontal variation of the observed flow

The u and w wind components and potential temperature observed at the 3.3 km level on 6 March 1982 are shown in Fig. 22. The most significant

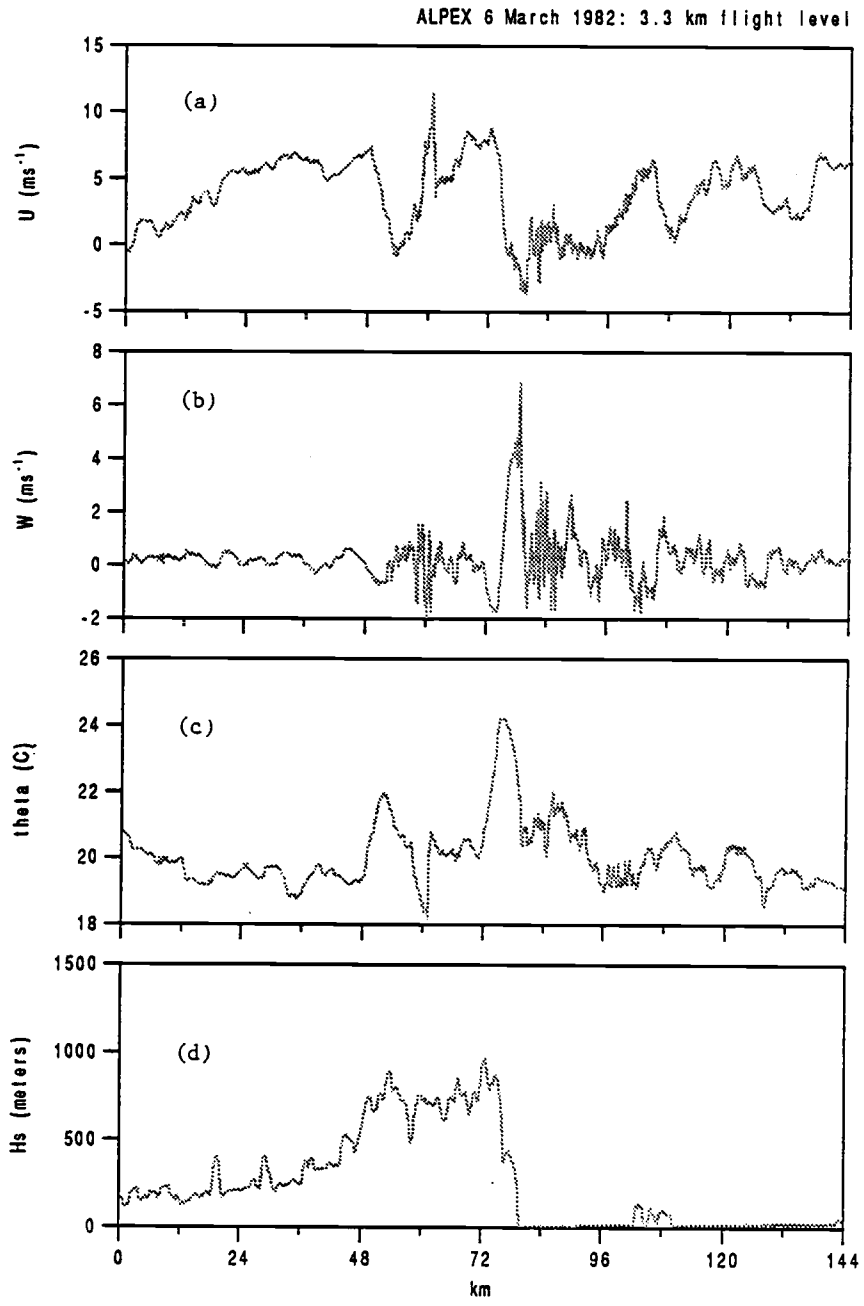

Fig. 22 Observed (a) u, (b) w, (c) θ, and (d) topography at 3.3 km level. Linear trend is removed from the raw data.

feature of the observed flow is the large-amplitude disturbances with a horizontal scale of a few tens of kilometers with small-scale turbulence superimposed on them. The larger-scale disturbances appear to be wave-like, and are confined to the coastal range with a width comparable to the width of the underlying ridge.

The larger-scale disturbances along the flight path can also be viewed in terms of the horizontal variation of the larger-scale vertical velocity variance (Fig. 23a). The larger-scale motions are constructed from band-pass filtering of raw records with 10 and 80 km cutoff wavelengths for the lower and upper limits of horizontal length scales, respectively. Noticeable peaks of the variance of larger-scale vertical velocity appear above the ridge between 45 to 110 km from the beginning of the record in Fig. 23a. The variance of band-pass filtered vertical velocity decreases rapidly with distance from the coastal range. Similar variations of the raw record and the variance of band-pass filtered vertical velocity along the flight path also appear at other flight levels on this day (not shown).

Growth and breaking of gravity waves are usually accompanied by significant asymmetry of the shape of perturbation streamlines and the concentrated horizontal gradients of u (Fig. 22). Such regions appear as boundaries of *ramp*-like structures and they may indicate the presence of *frontal* region associated with wave steepening. At the 3.3 km flight level (Fig. 22a), the sharpest decrease of u in the direction of the mean wind (convergence in the x-direction) occurs across an approximately 10 km wide region. An adjacent region of $\partial u/\partial x > 0$ (divergence in the x-direction) is several times wider. Observed vertical velocity (Fig. 22b) shows that the strongest updraft is concentrated in a narrow region where u decreases sharply along the flight path.

The turbulence occurring on this day is strongly related to larger-scale disturbances. The variance of 960 m high-pass filtered vertical velocity (Fig. 23b) shows that large variance of turbulence-scale vertical velocity appears in the frontal regions where u changes sharply. Such features also appear at other flight levels on this day. This appearance of turbulence at the frontal zones may imply the occurrence of gravity wave breaking in the lower part of the free atmosphere. Turbulence in the wave breaking regions will be discussed in more detail in Section 2.

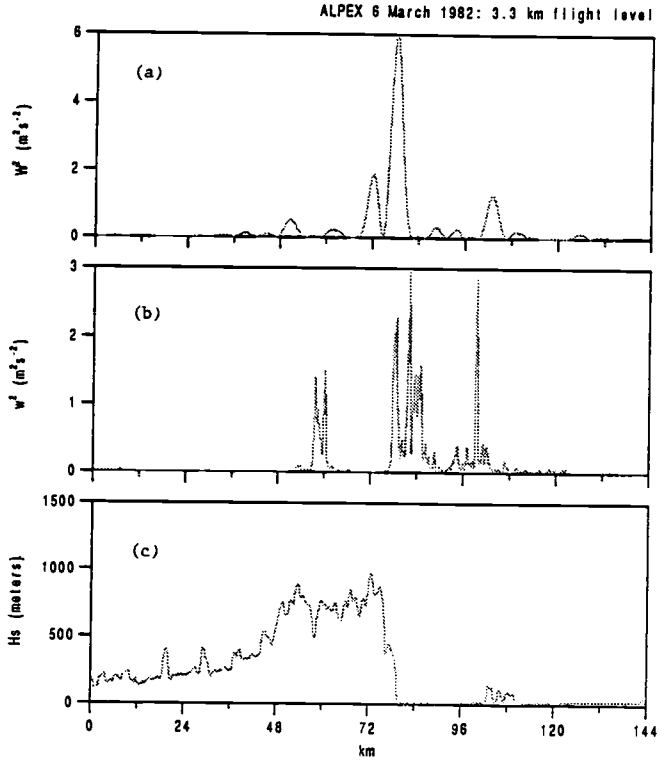

Fig. 23 Vertical velocity variance: (a) 10-80 km band-pass filtered: (b) 960 m high-pass filtered

3.1.2 Horizontal scales of motions

Since the disturbances are more event like and not periodic for the record, spectra are not particularly useful to study the length scales for this data. Instead, the variance of the Haar-wavelet transform (Daubechies, 1988) are computed. Statistics of the wavelet transform appear to be a useful tool for finding scales of localized disturbances (e.g. Mahrt, 1990). Tests performed on artificially generated records show that peaks of the Fourier (global) spectra tend to be located near the frequency of event periodicity (related to event width plus spacing), while peaks of the variance of the Haar-wavelet transform tend to be located near the scale of the width of the events (Gamage, 1990). The wavelet transform is local and finds the event width even if the events are randomly located. More details on the wavelet transform and it's application for finding scales of dominant disturbances in geophysical flows can be found in Mahrt (1990) and Gamage (1990).

The wavelet transformation operator $W[f(x), a, b]$ for a wavelet basis function $h[(x-b)/a]$ can be expressed in the form

$$W[f(x), a, b] = \frac{1}{a} \int h[(x-b)/a] f(x)\, dx \tag{1.1}$$

where the integration is over the transformation window of width a and b is the translate or centering of the spatial window of the calculation. To estimate horizontal differences, we choose the Haar-wavelet function $h[(x-b)/a]$ in the form

$$\begin{aligned} h(x_0, L) = -1, \quad & for \quad -\frac{1}{2} < \frac{x-b}{a} < 0, \\ 1, \quad & for \quad 0 < \frac{x-b}{a} < \frac{1}{2} \\ 0, \quad & otherwise. \end{aligned}$$

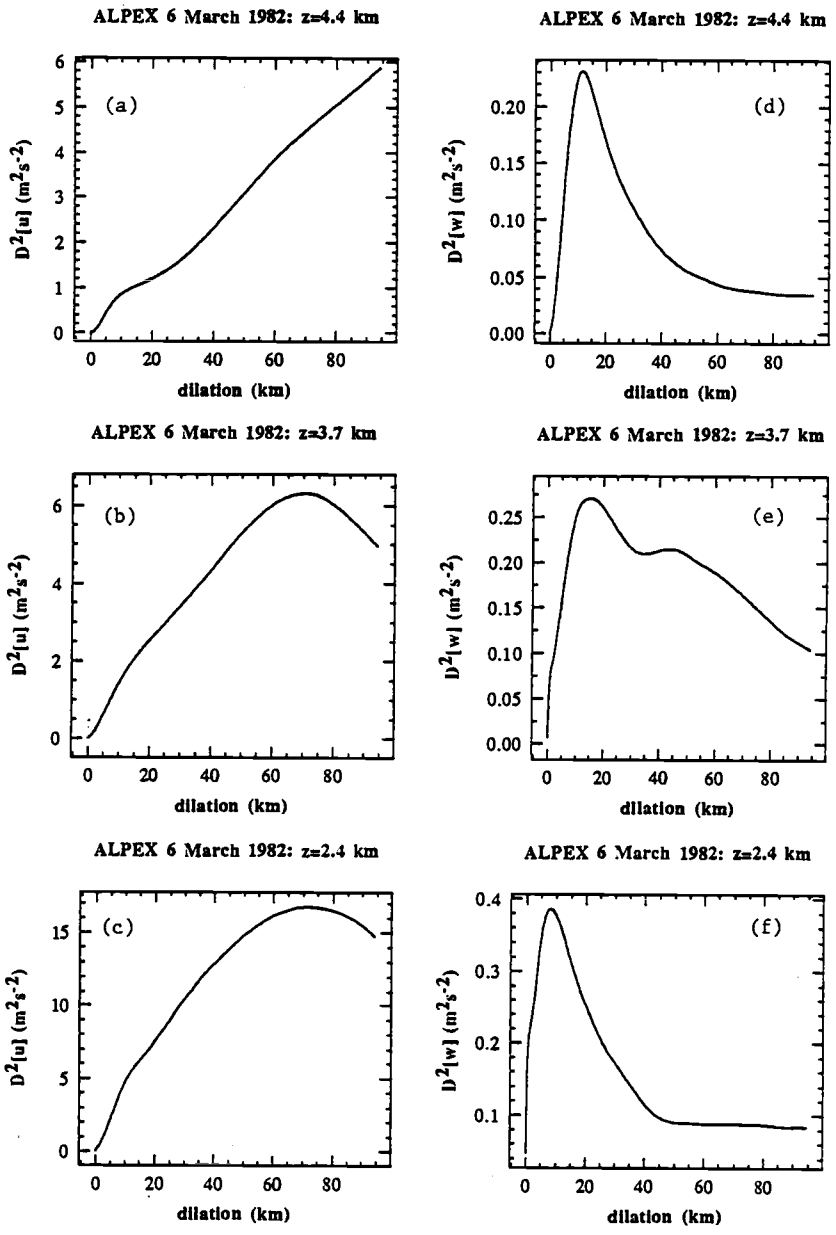

Fig. 24 The Haar-wavelet variances of u (a,b,c) and w (d,e,f) at 2.4, 3.7, and 4.4 km levels.

The Haar-wavelet transform effectively averages the variable $f(x)$ across each of the two halves of the transformation window and computes the difference between the averages.

The transformation window corresponding to the domain of integration of (1.1) sequentially marches through the record to construct a series of the wavelet transform. Arbitrary p^{th} moments of the wavelet transform for a scale a are defined as

$$D_a^p = \langle W^p[f(x), a, b] \rangle \tag{1.2}$$

where $\langle\ \rangle$ represents a simple unweighted average of the p^{th} moment of the wavelet transform over all of the local transforms of the record (summing over window position b) for a given scale a. For example, $p = 2$ represents the variance of the wavelet transform.

The wavelet variances of u and w suggest that disturbances observed on this day may be characterized by two distinct horizontal length scales. Peaks of wavelet variances of u at the 2.4 and 3.7 km flight levels (Fig. 24b,c) appear at dilations between 60 to 70 km, while peaks of wavelet variances of w (Fig. 24d,e,f) are located near the 10 km scale at all levels. The larger scale peak at 60 - 70 km is comparable to the width of the coastal range. The smaller-scale variations might be identified with the frontal zones associated with wave steepening. In addition to the variance peak for w, the wavelet variance of u suddenly changes slope near 10 km scale at all three flight levels (Fig. 24a,b,c) suggestive of weak secondary peak superimposed on the general trend of the wavelet variance with increasing scale.

The wavelet variance of u also suggests that mountain-scale disturbances are probably the most dominant coherent structures at the lower levels, below approximately 4 km above sea level. Peak value of wavelet variance decreases

with increasing altitude and at the highest flight level (4.4 km above sea level), wavelet variance of u no longer shows a peak at 60 to 70 km scale (Fig. 24a). This decrease of the wavelet variance suggests that mountain-scale motions lose strength above 4 km.

3.1.3 Asymmetry of the observed flow

The variance peak of w at 10 km is associated with narrow zones of the strongest updraft evident from the raw record (Fig. 22b). These zones may occur as steepening of streamlines found in previous studies of mountain waves (e.g., Huppert and Miles, 1969; Smith, 1977). The asymmetry of streamlines of the waves on this scale are probably associated with strong nonlinearity and perhaps influenced by the asymmetric slopes of the mountain as discussed in Smith (1977).

Even though such an association cannot be established with certainty, the spatial asymmetry of the disturbances can be documented for various parts of the streamline pattern. Fig. 25 sketches an asymmetric streamline pattern due to forward steepening. The vertical velocity associated with the streamline disturbance $\delta(x,z)$ can be approximated to the lowest order by

$$w \approx U \frac{\partial \delta(x,z)}{\partial x} \tag{1.3}$$

where U is the mean flow speed which is assumed to be a function of z only. Because U is horizontally uniform, horizontal variation of the vertical velocity is determined by the slope of the streamline $\partial\delta(x,z)/\partial x$. In Fig. 25, the maximum values of $\partial\delta(x,z)/\partial x$ and vertical motion appear in a narrow region at the left-hand side of the figure and vertical velocity outside this *frontal* region is much weaker. As the streamline becomes more asymmetric, the width of the *frontal* zone decreases further and the vertical motion becomes more concentrated. The

strong updraft appearing in a narrow region of strong horizontal convergence is evident in raw time series (Fig. 22).

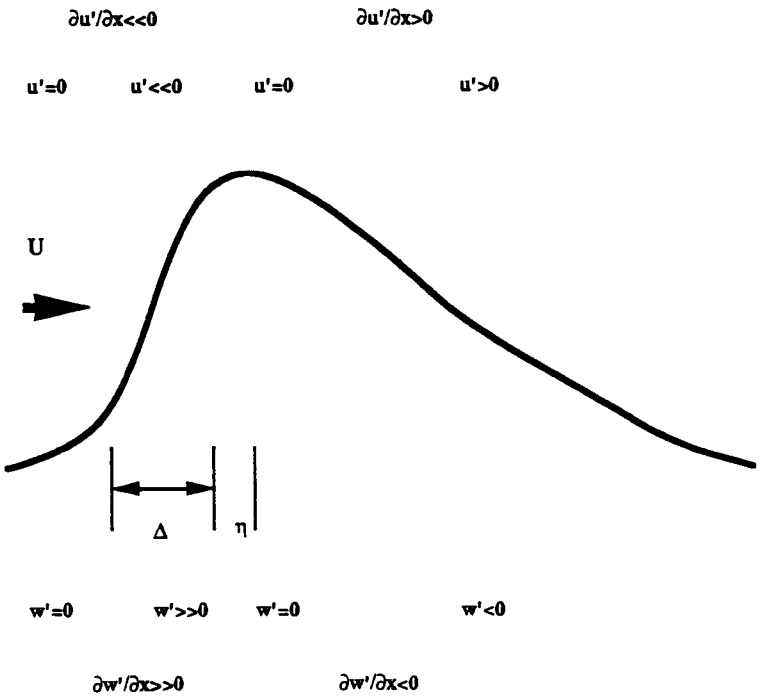

Fig. 25 A schematic diagram of a streamline (solid line) for an asymmetric disturbance with forward steepening and associated horizontal variations of the vertical and horizontal velocities where U is the mean flow and u' and w' are the perturbation flow. Δ denotes the width of the steepening *frontal* zone.

This asymmetry can be documented in terms of the skewness of the Haar-wavelet transform. The skewness of the Haar-wavelet transform is defined as

$$SK_a \equiv \frac{D_a^3}{[D_a^2]^{3/2}} \tag{1.4}$$

where SK_a represents the wavelet skewness at the scale a and again D_a^p represents the p^{th} moment of the wavelet transform for the entire record. The third moment of the Haar-wavelet transform, D_a^3, increases with increasing asymmetry and its sign is determined by the sign of the strongest gradients, while the wavelet variance is determined by the characteristic magnitude or energy of the disturbances. Hence, the Haar-wavelet skewness defined in (1.4) represents the relative importance of asymmetry compared to the strength of disturbances at the same scale.

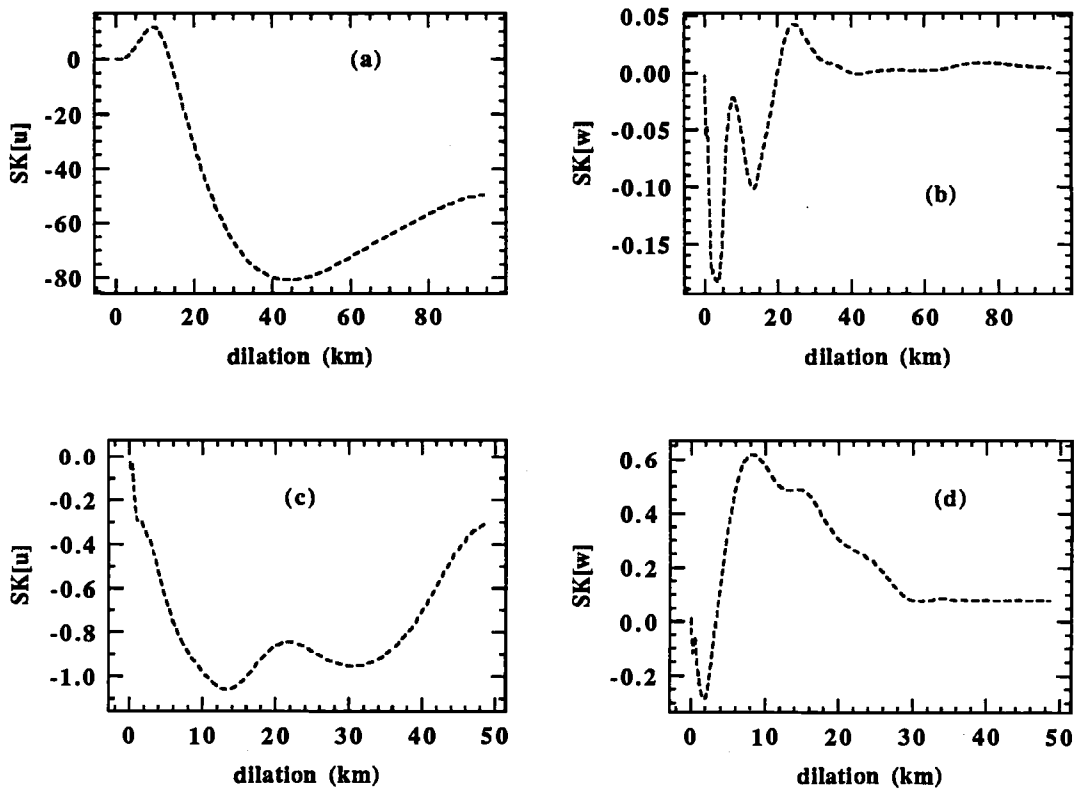

Fig. 26 The Haar-wavelet skewness of u and w: (a), (b) At 2.4 km level (c), (d) At 3.3 km level.

The Haar-wavelet skewness of w ($SK(w)$) at the 2.4 and 3.3 km flight level (Fig. 26) shows negative values at scales smaller than 2 km, and a positive peak near 10 to 20 km. The negative skewness of the Haar-wavelet transform of vertical velocity at the smallest scales agrees with the expected asymmetry of the turbulent eddies by the observed mean wind shear (Mahrt and Frank, 1988), hence it seems to be related to turbulence scale disturbances.

At larger scales (10 - 20 km), the skewness represents the asymmetry of the few main events. Peaks of the Haar-wavelet skewness of u and w appearing at 25 to 40 km dilations at the 2.4 km level and at 8 to 15 km dilations at the 3.3 km level can be explained by considering the asymmetry of streamlines as sketched in Fig. 25. With forward steepening, the strongest horizontal gradients of u' and w' are concentrated at the front associated with steepening, with $\partial u'/\partial x < 0$ and $\partial w'/\partial x > 0$. Note that adjacent zone of strong horizontal gradient (denoted by η in Fig. 25) with opposite signs, located between the maximum w' (or minimum u') and the crest of the streamline, may be of much smaller scale than the scale of the front mentioned here. For example, notice the rapid decrease of the vertical velocity immediately after the peak of the updraft in Fig. 22b. Hence, for scales comparable to the width of the front, positive gradients of w' and negative gradients of u' will dominate, which in turn determines the sign of the Haar-wavelet skewness. The negative skewness of u' and the positive skewness of w in Fig. 26 agrees with this model.

The positive (negative) peak of $SK(w)$ ($SK(u)$) at the 3.3 km level appears at smaller scales than the corresponding peaks at the 2.4 km level. Although the scale dependence of the wavelet skewness is more difficult to interpret than the scale dependence of the wavelet variance, the location of peaks of $SK(u)$ and $SK(w)$ at the low levels are comparable to the width of the region where u

changes rapidly (Fig. 22). Also, it may suggest that the frontal zone at the 3.3 km level is narrower than that at the 2.4 km level, implying more asymmetry in the shape of streamlines at the 3.3 km level.

The negative peak of $SK(w)$ at 15 km scale and the positive peak of $SK(u)$ at about 10 km appearing at 2.4 km level may imply the significance of the asymmetric topography in the shape of streamline of the main disturbances in the lower level (to be more specific, below the level where the vertical phase of a gravity wave is less than π: vertical phase of the gravity wave at 2.4 km level is about 0.6 π). As shown in Fig. 22d, the coastal range is characterized by a steep slope at the lee-side. Hence, lee-side steepening of the low-level wave disturbance (Smith, 1977; his Fig. 24) is expected to be enhanced by the asymmetry of the underlying ridge. Such asymmetry is expected to enhance the forward steepening of the streamline at levels where the vertical phase of gravity waves is $(2n + 1)\pi$, where n is an integer (Smith, 1977). Hence at the 3.3 km level, where the vertical wave phase is about 1.1 π, forward steepening and the associated asymmetry of the streamline will be further enhanced by the asymmetry of the underlying ridge. Above the 3.3 km level, such relationships between the Haar-wavelet skewness and the shape of streamlines (now shown) as predicted by theory (Smith, 1977) are not as clearly defined as in the lower levels, probably due to rapid change of the mean flow and the decrease of the intensity of gravity wave activity with height above 3.3 km level.

3.2 Observed momentum and heat fluxes and their relationships to the gravity waves induced by the coastal range

The most significant disturbances in the ALPEX data examined here are related to perturbations forced by the surface topography. Observed momentum and heat fluxes will then be interpreted using linear, hydrostatic, gravity wave theory with wave stress saturation conditions (Lindzen, 1981, 1988) as a criterion for wave breaking.

We will briefly review the solutions to the linear gravity wave equation with zeroth- and first-order lower boundary conditions as presented by Smith (1977). Then, in Subsection 3.2.2, the saturated wave stress will be derived for the linear gravity wave solutions by using the wave-stress saturation and supersaturation conditions introduced by Lindzen (1988). His development will be generalized to include a vertically-varying mean flow. Lindzen (1988) considered only the isothermal atmosphere with vertically uniform mean wind speed. His results are not directly applicable to the present case because strong height-dependence of the mean wind crucially affects the vertical propagation and breaking of gravity waves. The observed momentum fluxes will be compared against the wave momentum fluxes from the gravity wave models with the zeroth- or first-order lower boundary conditions and the wave stress saturation or generalized wave stress supersaturation conditions in Subsections 3.2.3 and 3.2.4. A formulation for the upward turbulent heat flux in the wave breaking regions is developed in Subsection 3.2.5 and compared with the observations.

3.2.1 Wave equation

The disturbance field of a streamline for a linear, stationary gravity wave in a steady, incompressible, hydrostatic flow can be expressed by Long's equation

(Long, 1953)

$$\nabla^2\delta + \ell^2\delta = 0 \tag{2.1}$$

where ∇^2 is a two-dimensional Laplacian operator in the $x-z$ plane, $\delta \equiv z-z_0$ is the height perturbation of a streamline from its undisturbed upstream value, and ℓ is the Scorer parameter defined as

$$\ell^2 \equiv -\frac{1}{U^2}\frac{g}{\rho}\frac{d\rho}{dz_0} \equiv \frac{N^2}{U^2}. \tag{2.2}$$

If we further assume that the horizontal wavelength of the motion is much larger than the vertical length scale, which can be justified for cases considered in this study, we can neglect terms containing second order derivatives in the horizontal, while retaining those containing second derivatives in the vertical. Then, expanding the Laplacian operator, (2.1) can be approximated as

$$\frac{\partial^2\delta}{\partial z^2} + \ell^2\delta = 0. \tag{2.3}$$

Equation (2.3) is closed with boundary conditions at the top and bottom of the domain. Assuming that surface topography is the only source of gravity waves, the radiation boundary condition is appropriate at the top of the domain. At the bottom of the domain, a kinematic boundary condition

$$\delta(x, h(x)) = h(x) \tag{2.4}$$

is imposed, where $h(x)$ is the height of surface topography and $\delta(x, h(x))$ is the disturbance of a streamline at the ground surface.

The lower boundary condition (2.4) can be expanded in terms of $h_0\ell_0$ (Smith, 1977) as

$$\delta(x, h(x)) \approx \delta(x, 0) + \frac{\partial\delta}{\partial z}(x, 0)h(x) + O(\ell_0^2 h_0^2(x)) = h(x)$$

where the subscript "$_0$" denotes the value at ground surface. As will be discussed in Subsection 2.4, surface processes such as blocking and boundary layer would limit $\ell_0 h_0$ to be less than unity. Hence the terms containing nonzero powers of $\ell_0 h_0$ may be neglected in the expanded lower boundary condition. By retaining only the lowest-order terms, we obtain

$$\delta(x,0) \;=\; h(x), \tag{2.5}$$

which is the usual expression of a linear lower boundary condition. If we retain the first order term and neglect the second and higher order terms from the expanded lower boundary condition, we obtain

$$\delta(x,0) \;+\; \frac{\partial \delta}{\partial z}(x,0)h(x) \;=\; h(x). \tag{2.6}$$

For a shallow mountain, (2.5) may be sufficient to represent the disturbance of streamline at the surface, but as the mountain becomes higher, the first-order term in (2.6) will have significant influence (Smith, 1977). We will consider the wave solution with the first-order lower boundary condition (2.6) in this study. Then the wave solution for the zeroth-order lower boundary condition (2.5) can be determined by neglecting the first-order term in the first-order solution.

To complete the problem, the shape of surface topography $h(x)$ must be determined. For simplicity, we assume a monochromatic sinusoidal topography with an amplitude h_0 defined as $h(x) = h_0 \cos(kx)$. In the presence of vertical shear and vertically nonuniform stratification the solution to (2.4) with the first-order lower boundary condition (2.6) can be written, by employing the WKB approximation, (Smith, 1977) as

$$\delta(x,z) \;=\; h(z)\left[\cos(kx + \phi(z)) \;+\; \frac{h_0 \ell_0}{2}\sin(2kx + \phi(z))\right] \tag{2.7}$$

where $\phi(z) \equiv \int^z \ell(z')dz'$ and $h(z)$ is the amplitude of streamline disturbances at height z.

The amplitude of the streamline height disturbance $h(z)$ can be derived by considering the principles of conservation of wave stress (Eliassen and Palm, 1961) or conservation of wave action (Smith, 1977) for linear internal gravity waves. The relationship between the mean flow and the amplitude of streamline disturbances for a linear, monochromatic gravity wave can be written (Smith, 1977) as

$$\rho(z)U(z)N(z)k\overline{\delta^2}(z) \;=\; constant \tag{2.8}$$

where $\overline{\delta^2}(z)$ is the mean-square amplitude of the gravity wave at height z and $\overline{()}$ denotes horizontal averaging over one wavelength. From (2.8), the ratio of the amplitude of a streamline disturbances (or normalized wave amplitude) at height z above the ground to the amplitude at the surface, $\gamma(z)$, can be determined as (Smith, 1977)

$$\gamma(z) \;\equiv\; \frac{h(z)}{h_0} \;=\left(\frac{\rho_0 U_0 N_0}{\rho(z)U(z)N(z)}\right)^{1/2} \tag{2.9}$$

where the subscript "$_0$" again denotes the value at the ground level.

Relationship (2.9) indicates that internal gravity waves amplify during vertical propagation due to decreasing density and sometimes decreasing wind speed and decreasing stratification of the mean flow with height. In the lower part of the atmosphere where the height-dependence of atmospheric density and stratification is not usually large, vertical shear of the mean flow will dictate most of the vertical variation of wave amplitude. On the other hand, the decrease of air density will dominate amplification and steepening of gravity waves in the upper atmosphere.

3.2.2 Wave stress saturation and wave breaking

As the amplitude of a gravity wave increases with height, the flow modified by the wave activity can become locally unstable, and hydrodynamic instability will limit the maximum growth of wave amplitude (saturation hypothesis; Lindzen, 1981). The major mechanism of wave breaking can be either shear-driven overturning (Kelvin-Helmholtz instability) or convective instability. For example, Thorpe (1973) observed in laboratory experiments that disturbances begin to grow when the gradient Richardson number of a mean flow decreases below 0.25. On the other hand, Smith (1977) and Lindzen (1981) have argued that convection, when it occurs, will dominate shear-driven overturning in wave breaking on the basis that the growth rate of perturbations by convective instability is much faster than that by Kelvin-Helmholtz instability. In this study, convective instability criterion will be used to derive wave breaking conditions.

The saturation hypothesis (Lindzen, 1981) assumes that the maximum slope of a streamline caused by wave activity will be limited by the onset of hydrodynamic instability. It has been suggested by several authors that when wave breaking occurs, gravity waves may acquire sufficient amplification to maintain some degree of hydrodynamic instability in the wave breaking region, not just a state of marginal (or neutral) stability (e.g. Smith, 1977). In the following, the term ***saturation*** will denote the assumption that the maximum amplitude of a gravity wave will be limited by the amplitude at neutrally stable state while ***supersaturation*** allows the maximum amplitude to exceed the value for the neutrally stable state.

Lindzen (1988) estimated the degree of supersaturation of internal gravity waves in an isothermal atmosphere with vertically uniform mean wind. His results suggest that gravity waves can achieve a significant degree of supersat-

uration in a wave breaking region, allowing more wave stress to propagate into higher altitudes. In the following, the wave stress supersaturation condition presented by Lindzen (1988) is modified to include vertically varying mean flow. Then supersaturated wave stress will be estimated for the wave solution with first-order lower boundary condition. The cases for zeroth-order lower boundary conditions or wave stress saturation conditions can be recovered from this result by neglecting the appropriate terms.

In the presence of wave breaking by convective instability, the slope of a streamline $(\partial\delta/\partial x)(x,z)$ due to internal gravity wave activity in a vertically varying atmosphere will be limited by a constraint on the height dependence of the vertical disturbance of the streamline (Lindzen, 1988). This condition can be mathematically expressed as

$$\left(\frac{\partial\delta}{\partial z}\right)_{max}(z) \leq 1 + S(z) \tag{2.10}$$

where $(\partial\delta/\partial z)_{max}(z)$ is the maximum value of the quantity $(\partial\delta/\partial z)(x,z)$ at height z and $S(z)$ is the (degree of) supersaturation at height z. When $S(z) > 0$ (2.10) implies the reversal of the slope of the streamline so that some degree of convective instability is maintained when wave breaking occurs. When $S(z) = 0$, (2.10) reduces to the expression for usual *wave-stress saturation* condition with respect to the convective instability.

The degree of supersaturation $S(z)$ can be determined by considering the reduction of the wave amplitude by wave breaking and the growth of the wave amplitude due to the vertical variation of the mean flow. It also depends on the streamline shape of the wave. To estimate the degree of supersaturation, the shape of streamline disturbance will be assumed to be sinusoidal.

The ratio of the mean-square amplitude of a sinusoidal gravity wave with wave breaking to that without wave breaking $f(\alpha)$ can be estimated by assuming

complete flattening of streamline in the wave breaking region as (Lindzen, 1988; his equation 8a)

$$f(\alpha) \equiv \frac{\left(\int_0^{(3\pi/2)\,-\,\alpha} + \int_{(3\pi/2)\,+\,\alpha}^{2\pi}\right) \cos^2\beta \; d\beta}{\int_0^{2\pi} \cos^2\beta \; d\beta} \tag{2.11a}$$

where α is the half-width of the wave breaking region in radians (see Lindzen, 1988; his figure 1) and $\beta \equiv kx + \phi$, where k is the horizontal wavenumber. The reduction factor $f(\alpha)$ is obtained as a function of the half width of the wave breaking region α by integrating (2.11a) with respect to horizontal distance as (Lindzen, 1988; his equation 8b)

$$f(\alpha) = \frac{\pi - \alpha + 0.5 \sin(2\alpha)}{\pi}. \tag{2.11b}$$

The wave grows as it propagates through the convectively unstable region due to the vertical variation of the mean flow. Determining the growth of the mean-square amplitude of the gravity wave with height requires consideration of the vertical variations of wind speed, atmospheric density, and buoyancy frequency. The ratio of the mean-square amplitude of the gravity wave at height z to that at height $z + D$ is obtained from (2.8) and (2.9) as

$$\frac{\overline{\delta^2}(z+D)}{\overline{\delta^2}(z)} = \frac{\gamma^2(z+D)}{\gamma^2(z)} \tag{2.12}$$

where $\overline{\delta^2}(z)$ again is the mean-square amplitude of the gravity wave at height z and γ is again the normalized amplitude defined by (2.9).

To make an analogy to the isothermal atmosphere with constant wind speed considered by Lindzen (1988), we introduce an *equivalent scale height H*. Across a layer of depth D, the growth of the mean-square amplitude (2.12) can be expressed by using an equivalent scale height H defined by the relationship

$$\frac{\overline{\delta^2}(z+D)}{\overline{\delta^2}(z)} = e^{D/H}. \tag{2.13}$$

Notice that the argument of the exponent is in terms of $1/H$ instead of $1/2H$, as appearing in Lindzen (1988), since we are concerned with the growth of the mean square amplitude with height. Then the *equivalent scale height* H can be determined from (2.12) and (2.13) as

$$H = \frac{D}{\ell n[\gamma^2(z+D)/\gamma^2(z)]}. \tag{2.14}$$

Defining the equivalent scale height as (2.14), we can follow the procedure presented in Lindzen (1988). In the case of an isothermal atmosphere with constant wind speed, the equivalent scale height (2.14) reduces to the usual definition of the scale height (g/RT).

Lindzen (1988) estimated the depth of the unstable region D by assuming that the depth and width of wave breaking region are related via the dispersion relationship of linear gravity waves. Instead of following his approach, we will estimate D from the shape of the streamline disturbance to be more consistent with the physical dimension of the wave.

We first estimate the maximum depth of the convectively unstable region which does not consider the limitation of the convection on the vertical wave propagation. The depth of the unstable region D can be estimated from the shape of streamline disturbances and the width of the wave flattening region ($3\pi/2 - \alpha \leq kx + \phi \leq 3\pi/2 + \alpha$). For a sinusoidal streamline disturbance, the depth of the unstable region D may be written as

$$D \approx h(z)\left[\cos\left(\frac{3}{2}\pi + \alpha\right) - \cos\left(\frac{3}{2}\pi - \alpha\right)\right] = 2h(z)\sin\alpha \tag{2.15a}$$

where $h(z)$ is the amplitude of the streamline disturbance at z. Using the relationship between the wave amplitude at height z and at the surface (2.9), the depth of the convectively unstable region D (2.15a) is rewritten as

$$D \approx 2h(z)\sin\alpha = 2h_0\gamma(z)\sin\alpha \tag{2.15b}$$

where $\gamma(z)$ is again the normalized wave amplitude (2.9).

Lindzen (1988) has proposed that the vertical propagation of the wave is limited by the convection so that the actual depth of the convectively unstable region would be less than D estimated as in (2.15*b*). Following Lindzen (1988), the depth over which convection occurs (D_g) is assumed to be proportional to, but less than, D as

$$D_g = \mu D \tag{2.16}$$

where μ is a positive constant of less than 1. Then the growth of the mean-square amplitude (or the amplification factor $g(\alpha)$) over the depth D_g is obtained by substituting D_g for D in (2.13) as

$$g(\alpha) \equiv \frac{\overline{\delta^2}(z + D_g)}{\overline{\delta^2}(z)} \approx e^{D_g/H}. \tag{2.17}$$

By multiplying the reduction factor ($f(\alpha)$ (2.11b)) and the amplification factor ($g(\alpha)$ (2.17)) the net change of the mean square amplitude of the wave over the depth of the breaking region ($F(\alpha)$) can be expressed as a function of the half width of the wave breaking region α analogous to Lindzen (1988; his equation 13)

$$F(\alpha) = f(\alpha)g(\alpha). \tag{2.18}$$

Note again that the amplification factor $g(\alpha)$ in (2.17) is for the mean square amplitude of a gravity wave. In Lindzen (1988), the amplification factor (his equation 12) is calculated for the amplitude while the flattening $f(\alpha)$ (or the reduction factor; his equation 9) is calculated for the mean-square amplitude. Hence, the current derivation is more consistent. The relationship (2.18) implies that the streamline at wave breaking regions is not completely flat but maintains some slope as illustrated by Dunkerton (1989).

We assume that the wave breaking occurs in a narrow region compared to the horizontal wavelength (that is, α is small). We also assume that the

depth of convection is small compared to the effective scale height (that is, $D_g << H$). Then the net change of the mean-square amplitude $F(\alpha)$ and the depth of convection D_g can be approximated by expanding $\sin\alpha$, $\cos\alpha$, and $e^{D_g/H}$ for small values of α and D_g/H in (2.11*b*), (2.15*b*) and (2.17) as

$$F(\alpha) \approx \left(1 - \frac{2}{3\pi}\alpha^3\right)\left(1 + \frac{D_g}{H}\right) \approx 1 + \frac{D_g}{H} - \frac{2}{3\pi}\alpha^3 \qquad (2.19)$$

and

$$D_g = \mu D = 2\mu h_0 \gamma \sin\alpha \approx 2\mu h_0 \gamma \left(\alpha - \frac{\alpha^3}{6}\right). \qquad (2.20)$$

At an equilibrium state, the net change of the mean square amplitude in the wave breaking region $F(\alpha_e) = 1$, where α_e denotes the half width of the wave breaking region at the equilibrium state. This half width α_e can be estimated from (2.19) and (2.20) as

$$\alpha_e = \left(\frac{6\mu h_0 \gamma}{\mu h_0 \gamma + 2H/\pi}\right)^{1/2}. \qquad (2.21)$$

Then $(\partial\delta/\partial z)_{max}$ (or $\tilde{A}$ in Lindzen, 1988) in the presence of wave breaking can be evaluated from the geometric argument of Lindzen (1988; see his figure 1) as

$$\left(\frac{\partial\delta}{\partial z}\right)_{max} = \frac{1}{\cos\alpha_e}. \qquad (2.22)$$

The constant μ in the expression for the depth of the wave breaking region D_g (2.20) can be estimated by considering the balance between the convective time scale and the time scale for the propagation of the wave energy across the wave breaking layer (Lindzen, 1988) as

$$\mu \approx \frac{U}{N}\left(\frac{\sqrt{2}}{6\pi}\frac{k}{H}\right)^{1/2}\frac{H}{h_0\gamma} = \left(\frac{\sqrt{2}}{3}\frac{H}{L}\right)^{1/2}\frac{1}{h_0\gamma\ell}. \qquad (2.23)$$

Expanding $\cos\alpha_e$ for small α_e and substituting into (3.22), and substituting the result into (2.23), we obtain

$$\left(\frac{\partial\delta}{\partial z}\right)_{max} \approx 1 + \frac{3}{2}\frac{(\pi/\ell)(\sqrt{2}H/3L)^{1/2}}{(\pi/\ell)(H/3\sqrt{2}L)^{1/2} + H}. \qquad (2.24)$$

From (2.24) the degree of supersaturation $S(z) \equiv (\partial\delta/\partial z)_{max} - 1$ is determined as

$$S(z) = \frac{3}{2}\frac{(\pi/\ell)(\sqrt{2}H/3L)^{1/2}}{(\pi/\ell)(H/3\sqrt{2}L)^{1/2} + H}. \tag{2.25}$$

The degree of supersaturation estimated by (2.25) is somewhat different from that estimated by Lindzen (1988). The first term in the denominator on the right hand side of (2.25), which is absent in Lindzen's result, comes from the difference in the expression of the depth of the convectively unstable region D in (2.15b). This term is thought to be usually smaller than the equivalent scale height H, and may be neglected. When this term is neglected, the degree of supersaturation estimated in the current study is larger than that estimated by Lindzen (1988) by a factor of $\sqrt{2}$. This difference is the result of the more consistent estimation of the growth factor $g(\alpha)$ in (2.17).

Computations in Subsection 3.4 will show that the degree of wave stress supersaturation estimated in the wave breaking region on 6 March in ALPEX appears to be about 10 to 20 %, that is, the wave stress supersaturation condition allows 10 to 20 % more wave amplitude than would be allowed by the wave stress saturation condition. The wave stress is proportional to the square of the wave amplitude, hence 20 % supersaturation leads to a 40 % increase of the transmitted wave stress across the wave breaking region.

Having estimated the degree of supersaturation, we proceed to calculate the wave stress for a given degree of supersaturation. From the wave solution with first-order lower boundary condition (2.7), the quantity $\partial\delta/\partial z$ becomes

$$\frac{\partial\delta}{\partial z}(x,z) = h(z)\ell(z)\left[-\sin(kx+\phi) + \frac{h_0\ell_0}{2}\cos(2kx+\phi)\right]. \tag{2.26}$$

Or, using the relationship between $h(z)$ and h_0 such as $h(z) = h_0\gamma(z)$, we can rewrite (2.26) in terms of h_0 and ℓ_0, which are the wave amplitude and the

vertical wave number at the surface, as (Smith, 1977),

$$\frac{\partial \delta}{\partial z} = h_0 \ell_0 \gamma' \left[-\sin(kx + \phi) + \frac{h_0 \ell_0}{2} \cos(2kx + \phi) \right] \tag{2.27}$$

where γ' is defined by

$$\gamma' \equiv \frac{\gamma(z)\ell(z)}{\ell_0} = \left(\frac{N(z)}{N_0} \right)^{1/2} \left(\frac{U(z)}{U_0} \right)^{-3/2} \left(\frac{\rho(z)}{\rho_0} \right)^{-1/2}. \tag{2.28}$$

For the wave solution with zeroth-order lower boundary condition, the second term in the square bracket of (2.27) is omitted. Relationships (2.27) and (2.28) imply that $(\partial\delta/\partial z)$ will increase (hence wave breaking is more likely to occur) as ρ and U decrease with height and N increases with height.

The maximum value of $\partial\delta/\partial z$ at height z occurs where $\sin(kx + \phi) = -1$, and is obtained from (2.27) as

$$\left(\frac{\partial \delta}{\partial z} \right)_{max} (z) = h_0 \ell_0 \gamma'(z) \left[1 - \frac{h_0 \ell_0}{2} \cos\phi \right] \tag{2.29}$$

for the wave solution with first-order lower boundary condition where γ' (2.28) and ℓ_0 represent the influence of the mean flow. If we neglect the second term in the square bracket in (2.29), we would obtain $(\partial\delta/\partial z)_{max}$ for the wave solution with zeroth-order lower boundary condition. From (2.29), $(\partial\delta/\partial z)_{max}$ can be determined from the known height of the surface topography h_0 and the mean flow which determines ℓ_0 and the growth of the wave amplitude with height, $\gamma(z)$.

$(\partial\delta/\partial z)_{max}$ determined by (2.29) cannot exceed the value corresponding to the wave breaking condition (2.10). The wave breaking condition (2.10) in turn limits the maximum amplitude of the streamline disturbance $h(z)$ at that height. Note that the degree of supersaturation (2.25) and the corresponding wave breaking condition (2.10) are determined solely by the mean flow profile.

Consequently the maximum wave amplitude allowed in the presence of wave breaking is determined by the mean flow profile.

From the wave breaking condition (2.10) and the expression for $(\partial\delta/\partial z)_{max}$ (2.29), we can estimate the maximum amplitude of a gravity wave at height z allowed in the presence of wave breaking. We define a new variable h_m such as

$$h_m(z) \equiv \frac{h_{max}(z)}{\gamma(z)} \tag{2.30}$$

where h_{max} is the maximum allowable amplitude of a gravity wave in the presence of wave breaking and h_m is a surrogate mountain height corresponding to h_{max}. h_m carries information about saturated or supersaturated wave amplitude and is independent of the height of the actual surface topography. We can obtain h_m by substituting $(\partial\delta/\partial z)_{max}$ on the left hand side of (2.29) with the wave breaking condition (2.10) and substituting h_0 on the right hand side of (2.29) with h_m. The resulting equation is written as

$$h_m \ell_0 \gamma' \left[1 - \frac{h_m \ell_0}{2} \cos\phi\right] = 1 + S(z). \tag{2.31}$$

Then h_m is determined by solving (2.31) with known $S(z)$ (2.25) and vertical wave phase ϕ. The maximum amplitude of a gravity wave at height z, h_{max}, is determined from h_m and (2.30). This maximum amplitude h_{max} will be used below to compute the maximum allowable wave stress (hereafter saturated wave stress) corresponding to wave stress saturation or supersaturation.

The average stress exerted by a gravity wave $\tau_w(z)$ is calculated by

$$\tau_w(z) = -\rho(z)\overline{\tilde{u}\tilde{w}}(z) = -\frac{1}{L}\int_{-L/2}^{L/2} \rho(z)\tilde{u}(x,z)\tilde{w}(x,z)dx \tag{2.32}$$

where $\rho(z)$ is again the mean atmospheric density, L is the horizontal wavelength of the wave, and $\tilde{u}(x,z)$ and $\tilde{w}(x,z)$ are disturbances of horizontal and

vertical components of wind speed due to wave activity given by the following relationships;

$$\tilde{u} = -U\left(\frac{\partial \delta}{\partial z}\right)(x,z) \tag{2.33}$$

$$\tilde{w} = U\left(\frac{\partial \delta}{\partial x}\right)(x,z) \tag{2.34}$$

where U is the mean wind speed and $\delta(x,z)$ is again the vertical displacement of the streamline due to gravity wave activity. By evaluating (2.32) together with the expressions for $\tilde{u}$ (2.33) and $\tilde{w}$ (3.34), the average wave stress for the gravity wave solution with first-order lower boundary condition is obtained as

$$\tau_w(z) \approx \frac{1}{2}k\rho(z)U(z)N(z)h^2(z)\left[1+\frac{(h_0\ell_0)^2}{4}\right] \tag{2.35a}$$

where $k \equiv 2\pi/L$ is the horizontal wave number of a gravity wave. Substituting h_m and h_{max} from (2.30) and (2.31) for h and h_0 in (2.35a), we obtain the maximum allowable wave stress, τ_{sat}, corresponding to wave stress saturation or supersaturation at height z as

$$\tau_{sat}(z) \approx \frac{1}{2}k\rho(z)U(z)N(z)h_{max}^2(z)\left[1+\frac{(h_m\ell_0)^2}{4}\right]. \tag{2.35b}$$

Wave breaking occurs when the predicted incident wave stress (2.35a) exceeds the saturated wave stress (2.35b). Otherwise, wave breaking will not occur and the wave stress will be conserved with vertical propagation. This condition can be expressed as

$$\tau_w(z) \leq \tau_{sat}(z). \tag{2.35c}$$

When wave breaking occurs, the wave stress becomes equal to the saturated wave stress and the resulting wave stress divergence will decelerate the mean flow at a rate

$$\left(\frac{\partial U}{\partial t}\right)_w = \frac{1}{\rho}\frac{\partial \tau}{\partial z} \tag{2.35d}$$

where $(\partial U/\partial t)_w$ is the deceleration of the mean flow by wave stress convergence and τ is the vertical profile of wave stress determined from (2.35a) subject to (2.35c).

3.2.3 Observed wave momentum flux during ALPEX

The momentum flux by gravity-wave scale disturbances has been estimated from aircraft data collected on 6 and 25 March 1982 in ALPEX. Wave-scale disturbances are selected by band-pass filtering raw data with cutoff wavelengths at 10 and 80 km, respectively. Selection of the cutoff wavelengths is based on the wavelet variance discussed in Section 1.

The wave-scale momentum flux is averaged along a flight track for a 120 km wide region above the coastal range where the wave activity is most pronounced. Averaging lengths on such a scale may not satisfy the requirement for stable flux estimates discussed by Lumley and Panofsky (1964) and Wyngaard (1972). However, large-scale disturbances observed in each flight leg appear to be stationary and sampling problems here are quite different from those of random signals.

Even though we expect that topographically-induced gravity waves are the most dominant disturbances observed during the period, it is not feasible to determine the "$surface$" momentum flux directly related to gravity waves. The momentum flux calculated from band-pass filtered variables may include contributions from various disturbances which are not directly related to the gravity waves induced by the underlying ridge. Hence, only the component of wave-scale momentum flux in the opposite direction of the low-level mean flow will be analyzed to partly filter out the effects not directly related to the gravity waves induced by the underlying ridge. Such components of momentum flux (or stress) will be called the *parallel momentum flux* hereafter. The parallel

momentum flux is determined from the observations as

$$(\overline{\tilde{u}\tilde{w}})_p \equiv -\frac{<\overline{\tilde{u}\tilde{w}}, \mathbf{V}_0>}{|\mathbf{V}_0|} \tag{2.36}$$

where again "$\tilde{()}$" refers to band pass variables, "$\overline{()}$" refers to averaging along the flight path, $<,>$ represents the inner product of two vectors, the subscript p denotes the *parallel* components, and $\mathbf{V}_0$ is the mean wind near the ground surface.

On 6 March 1982, the observed parallel momentum flux is about 1.9 Nm^{-2} at 2.3 km level and decreases with height below the critical level (open circles in Fig. 27). At the highest observation level, at 4.8 km above sea level, the observed parallel momentum flux becomes about 0.25 Nm^{-2}. This vertical variation of the parallel momentum flux implies that the mean wind component parallel to the surface wind is decelerated at a rate about 6×10^{-4} ms^{-2} due to wave momentum flux divergence in the layer. This forcing on the mean flow due to the wave momentum flux divergence is comparable to the forcing by Coriolis force on 6 ms^{-1} wind. Hence wave drag appears to be important in the evolution of the low level flow over the coastal range on this day.

This vertical variation of the observed parallel momentum flux is consistent with the expected occurrence of wave breaking on this day. Conservation of wave stress for linear gravity waves implies that wave momentum flux should *increase* with height due to the decrease of atmospheric density with height. Hence decreasing wave momentum flux with height can be regarded as an indication of *decreasing* wave stress with height and the occurrence of gravity wave breaking.

Unlike the case observed on 6 March 1982, the parallel momentum flux observed on 25 March 1982 increases with increasing altitude (open circles in Fig. 28) with a rate comparable to the inverse of the decrease of atmospheric density with height. Therefore, this case probably does not contain wave breaking in

the lower troposphere.

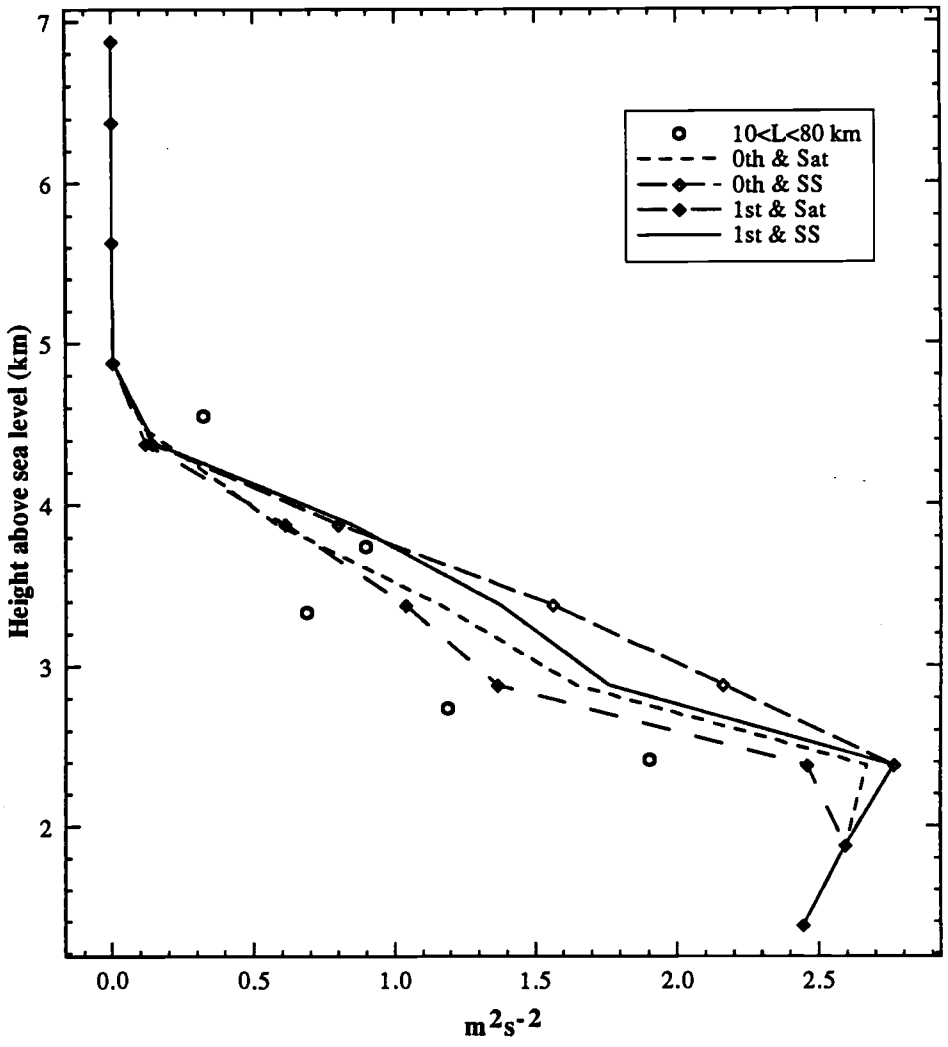

Fig. 27 Observed and model-estimated wave momentum flux on 6 March 1982 in ALPEX. Open circles are the observed momentum flux from $10 < L < 80$ km band-pass filtered variables and lines are model results. In the legends, "0th" and "1st" denote the zeroth- and first-order LBC while "Sat" and "SS" represent the wave stress saturation and supersaturation conditions.

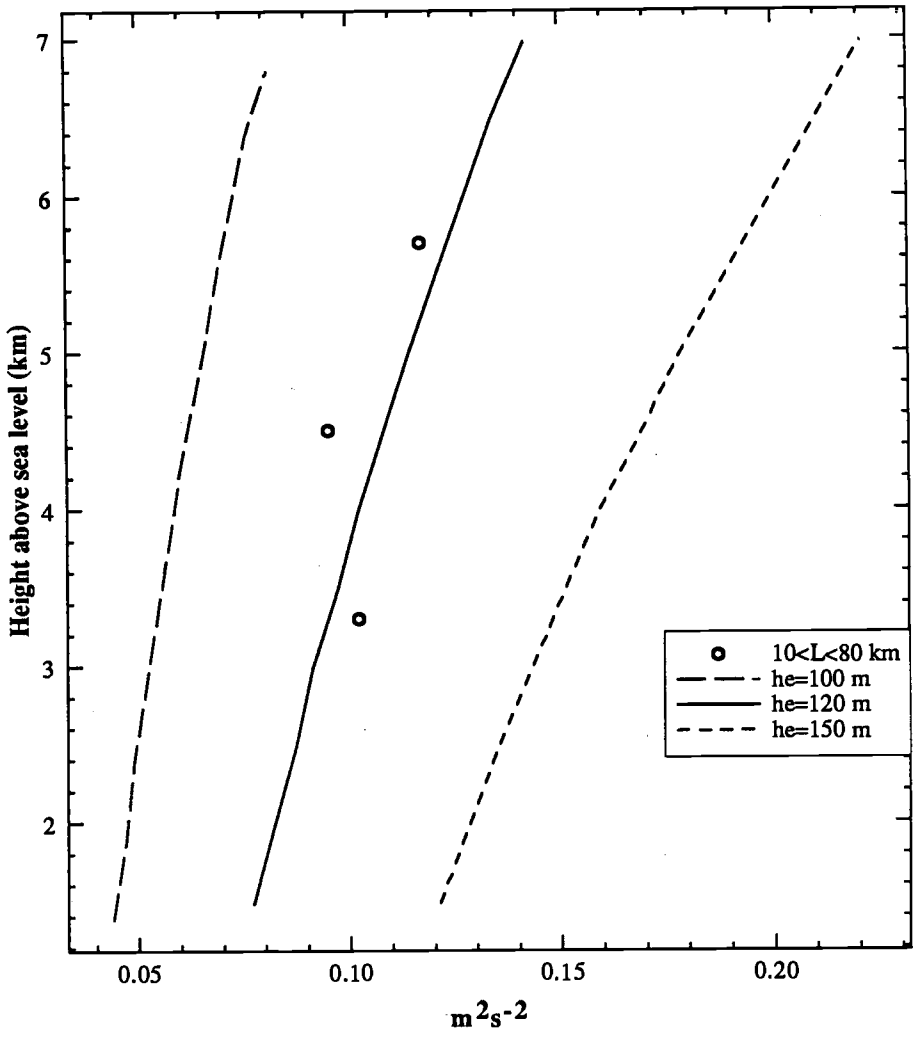

Fig. 28 Observed and model-estimated wave momentum flux on 25 March 1982 in ALPEX. Open circles are the observed momentum flux from $10 < L < 80$ km band-pass filtered variables and lines are model results with different effective mountain heights.

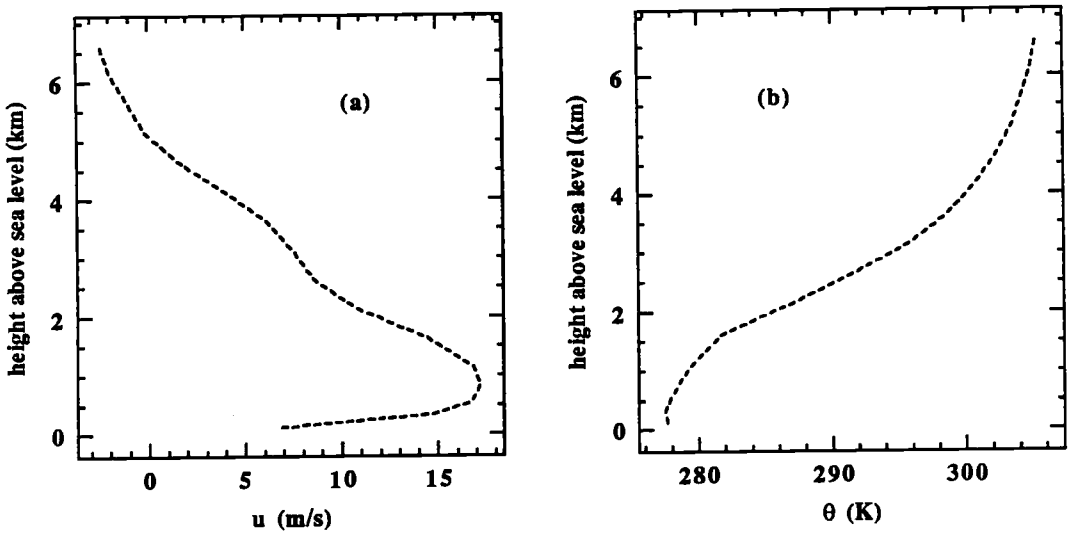

Fig. 29 The upstream profiles for U (a) and θ (b) from the radio sounding over Zagreb, Yug. at 1200 z on 6 March 1982.

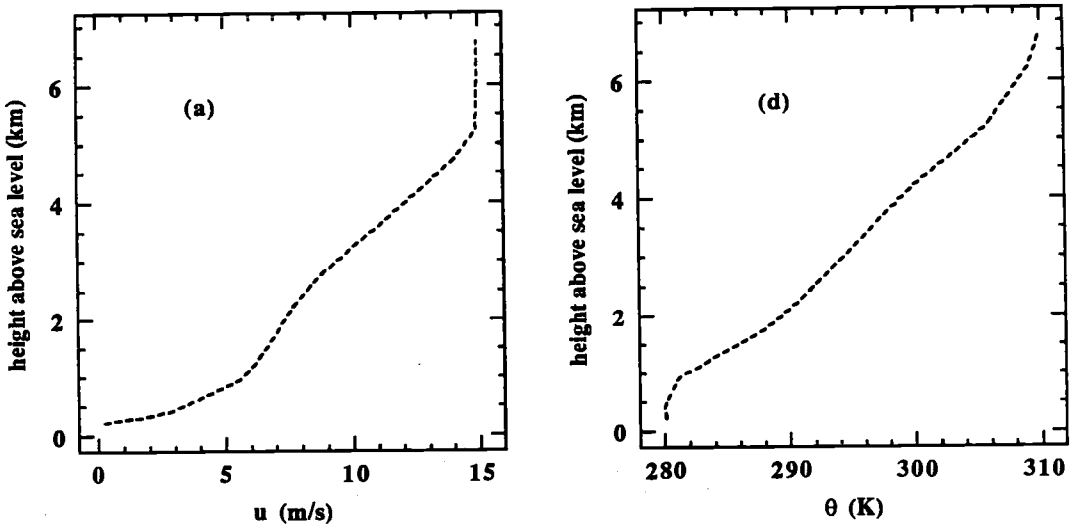

Fig. 30 Same as Fig. 9, except 25 March 1982. These profiles are derived by averaging the soundings at 0600 and 1200 LST.

3.2.4 Wave momentum flux estimated by gravity wave models

The wave momentum fluxes are now calculated from gravity wave models with zeroth- and first-order lower boundary conditions and wave stress saturation and supersaturation conditions ((2.35a-c), (2.30) and (2.31)). For zeroth-order lower boundary condition the second term in the square bracket of (2.35a) and (2.35c) is neglected. For wave stress saturation condition, $S(z)$ on the right hand side of (2.31) is set to be zero.

The upstream flow profiles used in model calculations are shown in Fig. 29 (6 March 1982) and Fig. 30 (25 March 1982). The upstream flow profile for the 6 March 1982 case has been derived from a radiosonde sounding data taken at 1200 Z, 6 March 1982 over Zagreb, Yugoslavia. For the 25 March 1982 case, the upstream flow condition has been derived by averaging the radiosonde soundings taken at 0600 Z and 1200 Z, 25 March 1982 at Zagreb, Yugoslavia, because the aircraft observations have been made for the approximate period 0900 to 1200 Z. The speed of the parallel component wind is calculated by projecting the observed wind onto the direction of the surface wind. This wind component decreases with height on 6 March 1982, with a critical level appearing near 5 km above sea level while it increases with height on 25 March 1982.

To simplify calculations, the coastal range is treated as a two-dimensional, sinusoidal ridge with a horizontal wavelength of 60 km. The effective mountain height, which partly determines the magnitude of surface stress, has been taken as 500 m for 6 March 1982 and as 120 m for 25 March 1982. The effective mountain height will be discussed later in this section.

For 6 March 1982, the modelled wave momentum flux decreases with height below the critical level as a result of wave breaking, which is in good agreement with observations (Fig. 27). The resulting wave stress convergence decelerates

the mean flow in the layer between 2.5 to 5 km above sea level by as much as 10^{-3} m/s^2, which is comparable to the observation. The wave momentum flux calculated with the first-order lower boundary condition (Fig. 27, solid line) seems to agree better with the observed parallel flux than that calculated with zeroth-order lower boundary condition (Fig. 27, long dashed line). However, the difference between the two model predictions is small compared to uncertainties in the estimation of the observed wave momentum flux and in the determination of the model parameters.

On 6 March, the model predicts the maximum degree of supersaturation to be 18 % at 3.9 km (Fig. 31). The wave momentum flux estimated with the wave stress supersaturation condition is about 30 % larger than that estimated with wave stress saturation condition at 3 km level (Fig. 27).

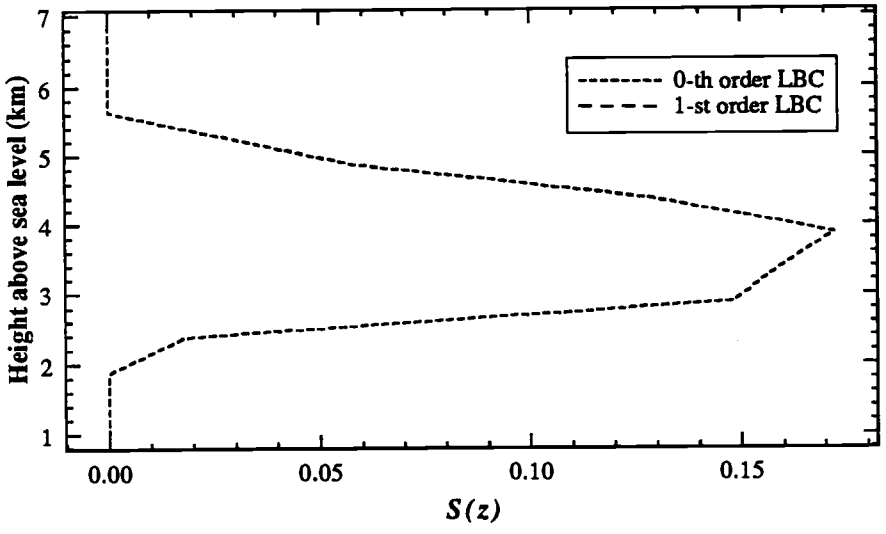

Fig. 31 The degree of supersaturation estimated for 6 March ALPEX.

This effect of supersaturation leads to significant additional wave stress convergence in higher levels while wave stress convergence is reduced in lower levels. Similar difference between two wave breaking models occurs with application of either zeroth-order or first-order lower boundary condition. For 25 March 1982, wave breaking is not predicted by any combination of lower boundary conditions and wave breaking criteria. The calculated wave momentum flux increases with increasing height for all models in agreement with observations (Fig. 27, solid line).

One of the most significant problems in calculating gravity wave momentum flux is the determination of the effective mountain height needed to calculate the wave stress at the ground surface. Based on a two-dimensional model, Stern and Pierrehumbert (1988) suggest that the maximum value of the effective mountain height would be limited by the condition

$$h_e = min[h_0, cU_0/\ell_0] \tag{2.37}$$

where the subscript"$_0$" again denotes the surface value, h_e is the effective height of a topography, and c is a constant estimated to be about 0.8 in their study (they used $c = 0.4$ for actual computation in the same work).

We estimate the effective mountain height h_e by equating the model wave stress at the surface to the observed wave stress below the wave breaking level. The model wave stress is estimated by evaluating (3.35a) at the surface. Using the zeroth-order lower boundary condition, effective mountain heights of 500 m and 120 m appear to yield the best agreement between the observed and model-estimated fluxes for 6 and 25 March 1982. Retaining the first-order term in the lower boundary condition, (3.35a) yields slightly smaller effective mountain heights. Examples of the estimated wave momentum fluxes with various effective mountain heights for 25 March case are shown in Fig. 27.

Using the above values of h_e and substituting the observed upstream wind and stratification into (3.37), the coefficient c in (3.37), perhaps coincidentally, is predicted to be 0.32 for both cases.

A more definitive determination of the effective mountain height would require exact knowledge of disturbances near the surface, such as the blocking of low-level flow (Pierrehumbert and Wyman, 1986) or pooling of cold air in valleys. Using the above value of c and the corresponding effective mountain height, the value of $(\partial\delta/\partial z)_{max}$ can then be calculated from (2.29). The computation indicates that the first-order term in the lower boundary condition changes $(\partial\delta/\partial z)_{max}$ by 15 % or less and probable reduction of the effective mountain height.

3.2.5 Upward turbulent heat flux in the wave breaking region

Comparison of the wave momentum flux estimated from linear gravity wave models in the previous subsection suggests that the difference between the wave momentum flux predicted by wave stress saturation and supersaturation conditions can be locally significant. Even though supersaturation of gravity wave stress has been suggested by many authors (e.g. Smith, 1977; Lindzen, 1988), observational verification of such hypothesis in the atmosphere is yet to be made. Also, the wave momentum flux with both wave breaking conditions agrees reasonably well with the observations. Therefore the flux observations alone are unable to determine which model better explains the observed momentum flux.

While definitive evaluation of such theories from observations is difficult, one indication of wave stress supersaturation can be found from the turbulent heat flux profile since wave stress supersaturation implies convective instability. Turbulent heat fluxes calculated for each flight level on 6 March show well-defined regions of upward turbulent heat flux over the upstream edge of the

coastal range (Fig. 32), roughly where maximum wave steepening is expected. The width of the upward turbulent heat flux region is approximately 10 to 20 km depending on the altitude. The region of the upward turbulent heat flux shown in Fig. 32 approximately coincides with the cloud-free region reported in the analysis by Smith (1987). Moreover, downward turbulent heat flux is observed where cloud layer appears in his analysis. Hence the relationship between the observed upward turbulent heat flux and cloud layer is ruled out.

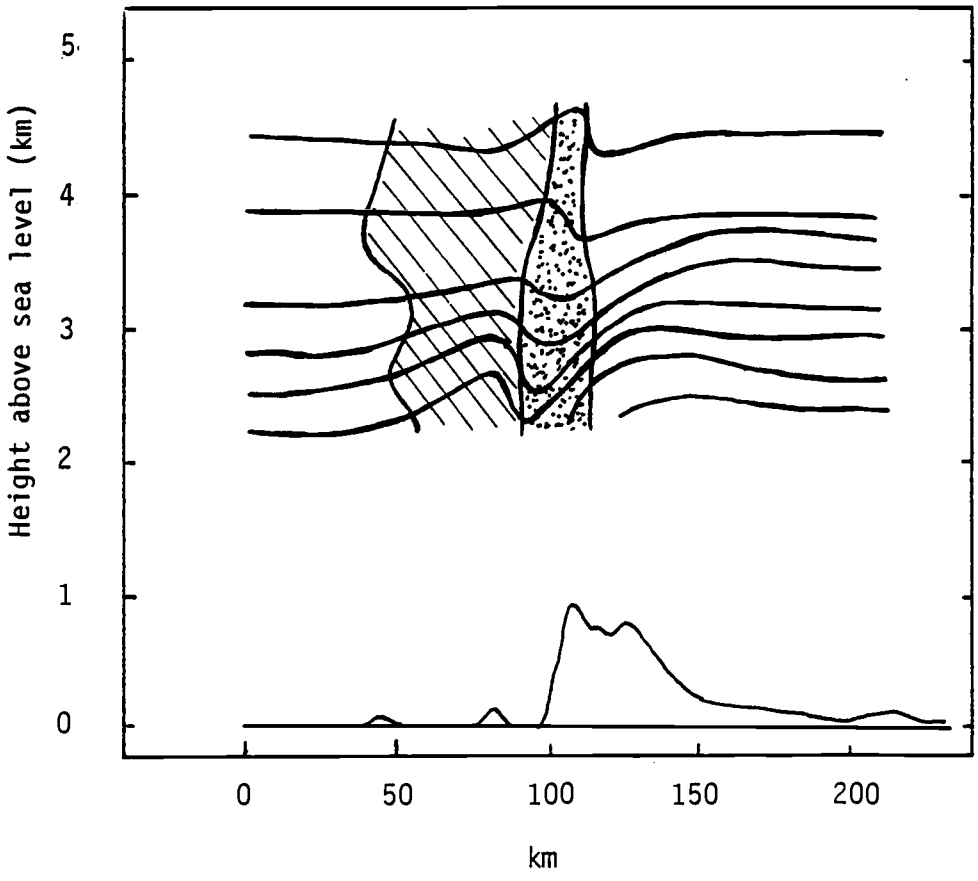

Fig. 32 A schematic diagram of the isentropes (after Smith, 1987) and the regions of downward (shaded with lines) and upward (shaded with dots) turbulent heat flux observed on 6 March 1982.

The occurrence of convection can be clearly seen from the horizontal variations of vertical velocity and potential temperature in composited "*eddies*" in the upward heat flux region (Fig. 33). The samples are centered at peaks of the coefficient of the Haar-wavelet transform of the vertical velocity calculated for a 480 m dilation. Only the samples where the wavelet coefficient of vertical velocity exceeds 0.1 m/s are selected. The combined total length of the selected samples represents about 80 % of total record length of the upward heat flux region for each flight level so that most of the record is represented.

In the composited structure, temperature and vertical velocity are almost exactly in phase (Fig. 33) leading to efficient upward heat flux. Since mean values of the turbulent heat flux by shear driven overturning in a stably-stratified flow is, in general, expected to be downward, the existence of a well-defined region of upward turbulent heat flux indicates that convection is occurring. This convection in turn is consistent with wave stress supersaturation with respect to the convective instability in wave breaking regions.

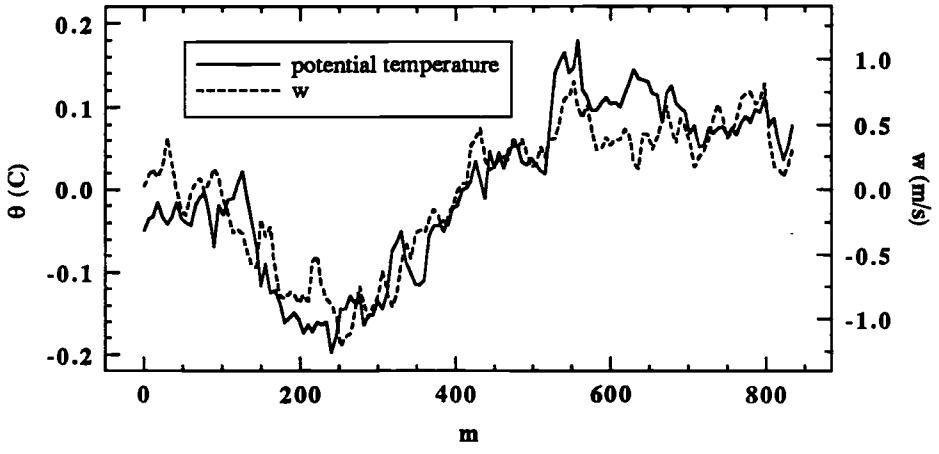

Fig. 33 The Composite of w (dashed line) and θ (solid line) in the upward turbulent heat flux region at 3.3 km level on 6 March 1982.

The magnitude of the mean upward turbulent heat flux decreases with height (Fig. 34). Turbulent heat fluxes in Fig. 34 are calculated by high-pass filtering the raw records with 480 m (cross in Fig. 34) and 960 m (open circle in Fig. 34) cutoff wavelengths for comparison. The cutoff wavelength for high-pass filtering is somewhat arbitrary and the estimated turbulent heat flux varies with the cutoff wavelength. An example of such sensitivity of the turbulent heat flux is shown in Fig. 35 for the upward heat flux region at the 3.3 km level. It shows that the upward heat flux reaches a maximum near 1 km cutoff wavelength.

The net turbulent heat flux for those parts of the record where the flux is upward can be viewed as the difference between the accumulated upward and downward heat flux. The net turbulent heat flux is much smaller than the accumulated heat flux of either sign. The ratio between the accumulated fluxes and the ratio of the fraction of the record occupied by upward turbulent heat flux to that occupied by by downward turbulent heat flux both have maxima near the 1 km cutoff wavelength. In this study, motions smaller than 960 m are regarded as turbulence-scale disturbances.

Some degree of convective instability should be maintained when wave stress supersaturation occurs (Lindzen, 1988). We now attempt to formulate a relationship for the upward turbulent heat flux in the wave breaking region. The purpose of this formulation is more to know the plausibility of the wave stress supersaturation condition for wave breaking rather than to provide a practical tool for modelling.

The upward turbulent heat flux in a wave breaking region may be estimated by assuming a relationship between the turbulent flux and the wave-modified gradient mean flow so that

$$\overline{w'\theta'} = - K\frac{\partial \theta}{\partial z} \tag{2.38}$$

where K is the eddy diffusivity for heat and θ is the total potential temperature modified by wave activity. When the wave stress is supersaturated, $\partial\theta/\partial z$ in the wave breaking region can be estimated by

$$\frac{\partial\theta}{\partial z} \approx \frac{\partial\Theta}{\partial z}\left(1 - \left(\frac{\partial\delta}{\partial z}\right)_{max}\right) = -S\,\frac{\partial\Theta}{\partial z} \tag{2.39}$$

where Θ is the mean potential temperature (not modified by wave activity) and S is the degree of supersaturation (2.25). From (2.39), nonzero supersaturation (positive $S(z)$) corresponds to convective instability.

The eddy diffusivity in the wave breaking region may be approximated as

$$K \approx \ell_w^2 \left|\frac{dV}{dz}\right| \tag{2.40}$$

where ℓ_w is the turbulent length scale for heat and V is the wind speed modified by wave activity. In the wave breaking region, turbulent length scale ℓ_w would be restricted by the depth of the wave breaking region, D_g, determined from (2.20), (2.21) and (2.23). Then D_g must be recognized as the maximum turbulent length scale which can be achieved corresponding to the largest-possible eddies in the wave breaking region.

Now we determine the wind shear in the wave breaking region. The total wind speed including wave modification can be estimated as

$$u \approx U\left(1 - \left(\frac{\partial\delta}{\partial z}\right)_{max}\right). \tag{2.41}$$

Hence the minimum wind speed (due to the maximum modification of the mean wind speed by gravity waves) would become

$$u_c \approx -S\,U, \tag{2.42}$$

and the maximum difference of wind speed across a depth comparable to the amplitude of the wave is approximately

$$\Delta U \approx U - u_c = (1+S)U \tag{2.43}$$

where u_c is given by (2.42). We assume that this maximum difference of wind speed (2.43) occurs over the amplitude of the vertical disturbance of the streamline so that the mean shear in the wave breaking layer can be approximated from (2.43) and the amplitude of the streamline disturbance as

$$\left|\frac{\partial u}{\partial z}\right| \approx \frac{(1 + S)U}{h(z)} \tag{2.44}$$

where $h(z)$ is again the amplitude of the vertical displacement of the streamline.

Assuming the mixing length to be proportional to the depth of wave breaking region and using the estimated wind shear (2.44), the eddy diffusivity in the wave breaking region may be approximated as

$$K \approx \alpha D_g^2 \frac{(1 + S)U}{h(z)}. \tag{2.45}$$

where α is a constant with magnitude less than or equal to 1. From (2.20), (2.21) and (2.23), D_g^2 can be estimated as

$$D_g^2 \approx a \left(\frac{H}{L}\right)^{1/2} k \left(\frac{U}{N}\right)^3 \tag{2.46}$$

where $a \equiv (2^{3/2}/3)^{1/2} \approx 0.97$.

Finally, the heat flux in the wave breaking region can be estimated from (2.38), (2.39), (2.45) and (2.46), together with the supersaturation (2.25) as

$$\overline{w'\theta'} \approx \alpha D_g^2 \frac{(1 + S)U}{h(z)} S\frac{d\Theta}{dz}. \tag{2.47}$$

The observed and model-calculated upward turbulent heat flux decreases with increasing altitude (Fig. 33) corresponding mostly to the decrease of the depth of convection $D_g(z)$ with height. Also, the results suggest that the constant α in (2.47) is order of unity. It may imply that the asymmetry of the underlying ridge enhances the slope of the streamlines, as discussed in the Section 1. However quantitative estimation of such effects is not available. For

Section 1. However quantitative estimation of such effects is not available. For 25 March 1982, well defined upward turbulent heat flux regions is not found as expected from the absence of wave breaking.

While the net turbulent heat transport by breaking gravity waves is another important problem, one must note that the estimation of turbulent heat flux by (2.47) is valid only in the region where wave breaking occurs by convective instability. Outside the convectively unstable region, wave activity can still lead to the generation of turbulence by reducing stratification or enhancing shear, but the mean heat flux in this region should be downward. For example, a wide region of the downward turbulent heat flux occurs immediately downstream of the relatively narrower region of the upward turbulent heat flux (Fig. 31). The turbulent flux in the stably-stratified region cannot be estimated by the simple procedure introduced in this section.

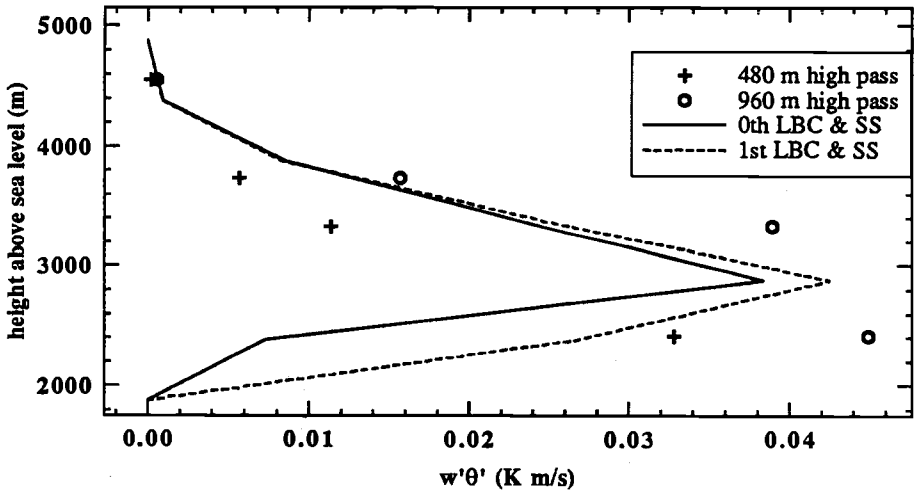

Fig. 34 The upward turbulent heat flux from high-pass filtered variables with cutoff wavelengths 480 m (cross) and 960 m (open circles) on 6 March 1982.

When averaged over the entire flight path the upward and downward heat flux appear to cancel each other resulting in very small net turbulent heat flux. As a result, the net influence of turbulent heat flux due to wave breaking on the mean stratification seems to be small for this day similar to the result of a rotating tank experiment by Dunkerton (1989).

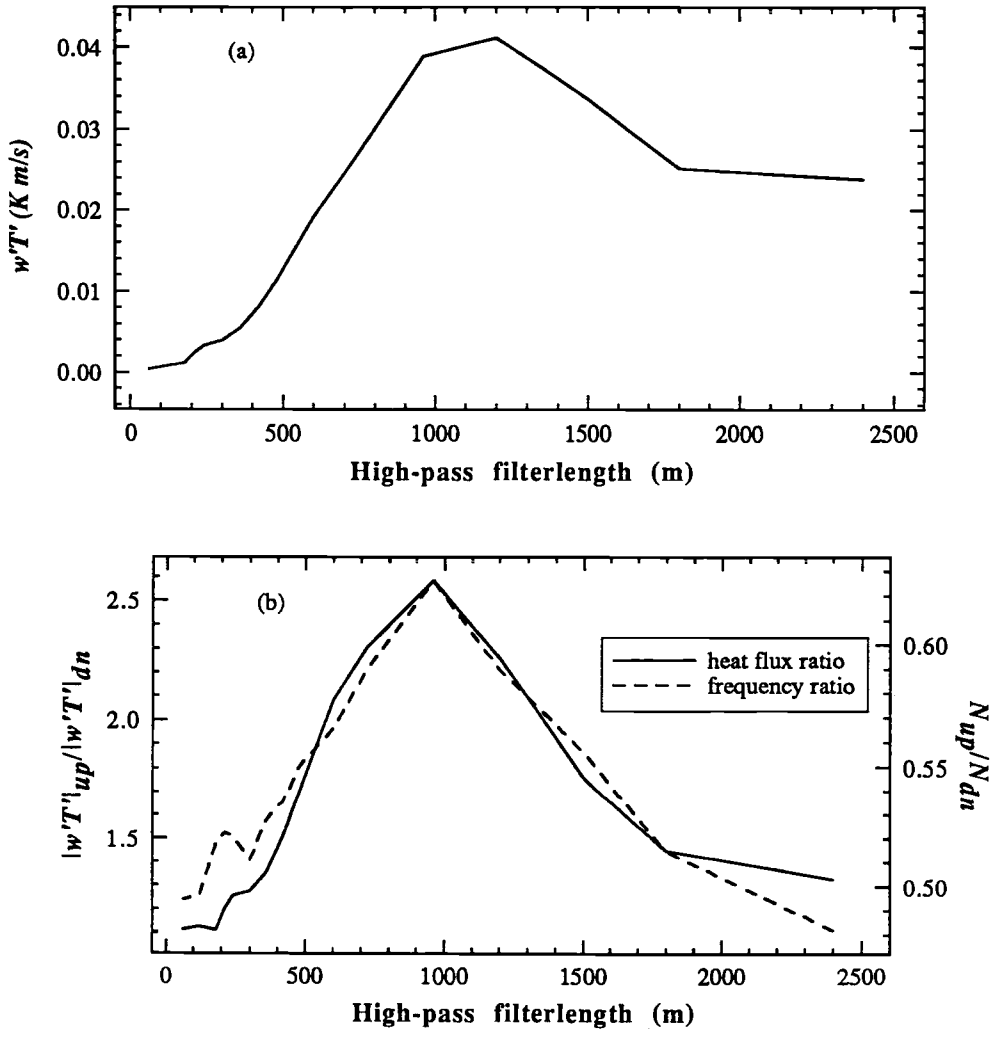

Fig. 35 (a) $\overline{w'\theta'}$, (b)$|w'\theta'|_{up}/|w'\theta'|_{down}$ (solid line) and N_{up}/N_{down}, N is the number of events, (dashed line) for different filterlength in the upward turbulent heat flux region at 3.3 km level on 6 March.

4. Conclusions

Turbulent fluxes, mixing lengths, and eddy diffusivities in layers of clear air turbulence are estimated from aircraft data obtained during SESAME and CABLE. The composite cospectra and quadrature from the aircraft legs suggests that significant turbulence-scale motions occur on horizontal scales of about 1 km and less. Motions on larger scales become more wave-like. At the very smallest scales, less than several tens of meters, the net heat flux becomes countergradient (upward) apparently resulting from small scale unstable stratification due to shear driven overturning.

For small positive gradient Richardson numbers, the eddy diffusivities and mixing lengths decrease rapidly with increasing gradient Richardson number. The mixing length decreases more slowly at larger values of the gradient Richardson number. The turbulent Prandtl number tends to increase to values significantly greater than unity with increasing Richardson number although the scatter is large. This indicates that the relative influence of pressure fluctuations on the momentum flux increase as the stability increases.

A formulation for turbulent mixing has been constructed from the data analyses by determining the similarity dependence of the mixing length and Prandtl number on the Richardson number in the free atmosphere. This formulation is applied to a column model. During the night, the model predicts significant turbulence at the top and bottom of the residual layer which is a remnant of the daytime boundary layer above the thin nocturnal surface inversion layer. The development of the turbulence at the top and bottom of the residual

layer is a direct consequence of shear developing in association with a low-level wind maximum (nocturnal jet). When eddy diffusivity is arbitrarily increased, turbulent mixing in the free atmosphere further reduces shear associated with local wind maxima.

The current formulation for turbulent mixing is allowed to override the boundary layer scheme in the upper part of the nocturnal inversion layer when boundary layer similarity theory fails to represent the impact of the local shear associated with the underside of the nocturnal jet. The model results suggest that this local shear can generate significant turbulence in the upper part of the nocturnal surface inversion layer especially late in the night when the jet is strongest.

With significant geostrophic wind shear, the turbulent mixing significantly alters the wind and potential temperature profiles in the residual layer and the nocturnal boundary layer becomes significantly deeper than that without the eddy mixing in the free atmosphere. However the model results also indicate that the depth and structure of the residual layer is sensitive to the value of the large-scale vertical motion, a quantity difficult to estimate from observations.

We have studied two distinctly different atmospheric flows over the coastal range of Northern Yugoslavia using aircraft measurements conducted during ALPEX. On 6 March, the most significant motions are associated with the steepening and breaking of orographic gravity waves. On 25 March low-level wave breaking does not occur and the wave momentum is transferred into the upper atmosphere. The most important conclusions from this study are:

(1) On 6 March, the Haar-wavelet transform of the vertical velocity exhibits maxima at horizontal scales between 10 and 20 km. Skewness of the Haar-wavelet transform of vertical velocity documents the asymmetry of the motions

at such scales. This asymmetry of gravity waves indicates the formation of *fronts* associated with wave steepening as observed by Smith (1977).

(2) Variance of the Haar-wavelet transform of u implies that the large-scale disturbances on 6 March 1982 is of horizontal scale between 60 and 70 km. This is comparable to the width of the underlying coastal range and the scale of the expected topographically-induced gravity waves.

(3) The observed momentum flux at the scale of the gravity waves decreases with increasing height on 6 March 1982 and increases with height on 25 March 1982. This vertical variation of the wave momentum flux implies that wave breaking is occurring on 6 March but not on 25 March. Deceleration of the wind component parallel to the surface wind below the critical level due to wave breaking and associated wave stress divergence on 6 March appears to be about 0.6 ms^{-2} which is comparable to the magnitude of Coriolis forcing.

(4) Estimated wave momentum flux by using linear gravity wave models agree with the observed momentum flux on both days. Different lower boundary conditions based on the zeroth- and first-order expansions of nonlinear lower boundary condition, respectively, (Smith, 1977) show differences of 10 to 15 % in the estimated wave momentum flux.

(5) The wave-stress supersaturation theory by Lindzen (1988) predicts 10 - 20 % supersaturation on 6 March 1982 which translates into 20 - 40 % more wave stress transfer into higher levels. But the difference between the wave stress saturation and wave stress supersaturation models may not be measurable due to uncertainties in observations and other model input variables such as the effective mountain height or the asymmetry of the underlying topography.

(6) The effective mountain height, one of the most important parameters in determining the gravity wave stress at the surface, appears to be limited by the

low-level wind and stratification by the relationship as

$$h_e = min\left[h_0, \frac{0.32U_0}{\ell_0}\right]$$

where h_e is the effective mountain height, and N_0 and U_0 are the stratification and mean wind speed near the surface. Such estimation of the upper limit of the effective mountain height is comparable to the one suggested in Stern and Pierrehumbert (1988).

(7) Regions of the upward turbulent heat flux, about 10 km wide, may be an evidence of wave breaking and convective instability. The magnitudes of the observed upward turbulent heat flux decrease with increasing altitude. The vertical profile of the observed upward turbulent heat flux can be well approximated by a flux gradient relationship based on the mixing length and vertical shear derived from the generalized wave stress supersaturation theory. Despite the occurrence of clearly defined upward and downward turbulent heat flux, the net turbulent heat flux over the entire flight path appears to be small and may not have significant influence on the mean stratification of wave breaking level on 6 March ALPEX.

Application of the topographic wave stress model in actual large-scale models requires, in addition to the knowledge of wave breaking, estimations of appropriate horizontal length scale L and the height of topography for each grid area (Palmer *et al*, 1986). The scale of dominant topography and its height will vary according to the model resolution. Also the use of this wave stress model in concert with the model of turbulent boundary layer requires further consideration.

REFERENCES

André, J. C., G. De Moore, P. Lacarrére, G. Therry, and R. Du Vachat, 1978: Modelling the 24 hr evolution of the mean and turbulent structures of the planetary boundary layer. *J. Atmos. Sci.*,**35**, 1861-1883.

André, J. C. and L. Mahrt, 1982: The nocturnal surface inversion and influence of clear-air radiative cooling., *J. Atmos. Sci.*,**39**, 864-878.

Arya, S. P. S., 1975: Buoyancy effects in a horizontal flat-plate boundary layer., *J. Fluid Mech.*,**68**, 321-343.

Blackadar, A. K., 1962: The vertical distribution of wind and turbulent exchange in a neutral atmosphere., *J. Geophys. Res.*,, **67**, 3095-3102.

Brown, Phillip R. A., 1983: Aircraft measurements of mountain waves and their associated momentum flux over the British Isles. *Quart. J. Roy. Meteorol. Soc.*,**109**, 849-865.

Daubechies, I., 1988: Orthogonal basis of compactly supported wavelets. *Comm. Pure. Appl. Math.*, **41**, 909-996.

Dunkerton, Timothy, 1989: Theory of internal gravity wave saturation. *PA-GEOPH.*, **130**, 373-397.

Ek, M. and L. Mahrt, 1990: *A user's guide to OSU1DPBL version 1.0.3: A one-dimensional planetary boundary layer model with interactive soil layers and plant canopy,*, Dept. of Atmos. Sci., Oregon State University, Corvallis, OR 97331.

Eliassen, A. and E. Palm, 1960: On the transfer of energy in stationary mountain waves. *Geophy. Publ.*, **22**, 1-23.

Estournel, C., R. Vehil, and D. Guedalia, 1986: An observational study of radiative and turbulent cooling in the nocturnal boundary layer (ECLATS EXPERIMENT). *Bound.-Layer Meteor.*,**34**, 55-62.

Finnigan, J. J., F. Einaudi, and D. Fua, 1984: The interaction between an internal gravity wave and turbulence in the stably-stratified nocturnal boundary layer., *J. Atmos. Sci.*,**41**, 2409-2436.

Gamage, N., 1990: *Modeling and analysis of geophysical turbulence: Use of optimal transforms and basis sets.*, Ph.D thesis, Oregon State University. 135p.

Garratt, J. R., 1985: The inland boundary layer at low altitudes. *Bound.-Layer Meteor.*,**32**, 307-327.

Heck, W. J., H. A. Panofsky, and M. A. Bender, 1977: The effect of clear-air turbulence on a model of the general circulation of the atmosphere. *Beiträge zur Physik der Atm.*, **50**, 89-97.

Heck, W. J., 1977: A comparison of estimated and directly measured turbulent heat fluxes in the lower troposphere., *Mon. Wea. Rev.*,**105**, 1337-1340.

Hoinka, Klaus P., 1985: Observation of the airflow over the Alps during a foehn event. *Quart. J. Roy. Meteorol. Soc.*,**111**, 199-224.

Holton, James R., 1982: The role of gravity wave induced drag and diffusion in the momentum budget of the mesosphere. *J. Atmos. Sci.*,**39**, 791-799.

Hsu, S. A., 1979: Mesoscale nocturnal jetlike winds within the planetary boundary layer over a flat, open coast. *Bound.-Layer Meteor.*,**17**, 485-494.

Hunt, B. G., 1990: A simulation of the gravity wave characteristics and interactions in a diurnally varying model atmosphere. *J. Met. Soc. Jap.*, **68**, 145-161.

Huppert, H. E., and J. W. Miles, 1969: Lee waves in a stratified flow, Part 3, Semi-elliptical obstacle. *J. Fluid Mech.*,**35**, 481-469.

Jasperson, W. H., G. D. Nastrom, and D.C. Fritts, 1990: Further study of terrain effects on the mesoscale spectrum of atmospheric motions. *J. Atmos. Sci.*,**47**, 979-987.

Kennedy, P. J. and M. A. Shapiro, 1980: Further encounters with clear air turbulence in research aircraft., *J. Atmos. Sci.*,**37**, 986-993.

Lenschow, D. H., X. S. Li, C. J. Zhu, and B. B. Stankov, 1987: The stably stratified boundary layer over the great plains., *Bound.-Layer Meteor.*,**42**, 95-121.

Lilly, D. K., J. M. Nicholls, R. M. Chervin, P. J. Kennedy, and J. B. Klemp, 1982: Aircraft measurement of wave momentum flux over the Colorodo Rocky mountains. *Quart. J. Roy. Meteorol. Soc.*,**108**, 625-642.

Lindzen, Richard S., 1981: Turbulence and stress owing to gravity wave and tidal breakdown. *J. Geophys. Res.*, **86**, 9707-9714.

Lindzen, Richard S., 1988: Supersaturation of vertically propagating internal gravity waves. *J. Atmos. Sci.*,**45**, 705-711.

Long, Robert R., 1953: Some aspects of the flow of stratified fluids, I. A theoretical investigation. *Tellus*, 42-58.

Louis, J., 1979: A parametric model of vertical eddy fluxes in the atmosphere., *Bound.-Layer Meteor.*,*17*, 187-202.

Louis, J., M. Tiedke, and J. F. Geleyn, 1981: A short history of the operational PBL parameterization at ECMWF. *Workshop on planetary boundary layer parameterization*, ECMWF., 59-79.

Lu, N., W. D. Neff, and J. C. Kaimal, 1983: Wave and turbulence structure in a disturbed nocturnal inversion. *Bound.-Layer Meteor.*,**26**, 141-155.

Lumley, J. L., and H. A. Panofsky, 1964: *The structure of atmospheric turbulence.*, New York, Interscience. 239p

Mahrt, L., R. C. Held, D. H. Lenschow, B. B. Stankov, and IB Troen, 1979: An observational study of the structure of the nocturnal boundary layer. *Bound.-Layer Meteor.*,**17**, 247-264.

Mahrt, L., 1985: Vertical structure and turbulence in the very stable boundary layer. *J. Atmos. Sci.*,**42**, 2333-2349.

Mahrt, L., 1987: Grid-averaged surface fluxes. *Mon. Wea. Rev.*,**115**, 1550-1560.

Mahrt, L. and N. Gamage, 1987: Observations of turbulence in stratified flow. *J. Atmos. Sci.*,**44**, 1106-1121.

Mahrt, L. and H. Frank, 1988: Eigenstructure of eddy microfronts. *Tellus*, **40A**, 107-119.

Mahrt, L. 1990: Eddy asymmetry in the sheared heated boundary layer. to appear in *J. Atmos. Sci.*

McFarlane, N.A., 1987: The effect of orographically excited gravity wave drag on the general circulation of the lower stratosphere and troposphere. *J. Atmos. Sci.*,**44**, 1775-1800.

Mizushina, T., F. Ogino, H. Ueda, and S. Komori, 1978: Buoyancy effects on eddy diffusivities in thermally stratified flow in an open channel. *Heat transfer 1978, 1*, 91-96, New York, Hemisphere publishing Co.

Nieuwstadt, F. T. M., 1984: The turbulent structure of the stable, nocturnal boundary layer., *J. Atmos. Sci.*,**41**, 2202-2216.

Noilhan, J. and S. Planton, 1989: A simple parameterization of land surface processes for meteorological models., *Mon. Wea. Rev.*,**117**, 536-549.

Palmer, T.N., G.J. Shutts, and R. Swinbank, 1986: Alleviation of a systematic bias in general circulation and numerical weather prediction models through an orographic gravity wave drag parameterization. *Quart. J. Roy. Meteorol. Soc.*,**112**, 1001-1039.

Pierrehumbert, R.T. and B. Wyman: Upstream effects of mesoscale mountains. *J. Atmos. Sci.*,**42**, 977-1003.

Rohr, J. J., E. C. Itsweire, K. N. Helland, and C. W. Van Atta, 1988: Growth and decay of turbulence in a stably stratified shear flow., *J. Fluid Mech.*,**000**, 000-000

Ruscher, P. H., 1987: *An examination of structure and parameterization of turbulence in the stably-stratified atmospheric boundary layer.*, Ph. D thesis, Oregon State University. 170p.

Smith, Ronald B.,1977: The steepening of hydrostatic mountain waves. *J. Atmos. Sci.*,**34**, 1634-1654.

Smith, Ronald B.,1987: Aerial observation of the Yugoslavian Bora. *J. Atmos. Sci.*,**44**, 269-297.

Stern, W.F. and R.T. Pierrehumbert, 1988: The impact of an orographic gravity wave drag parameterization on extended range predictions with a GCM. *Eighth conference on numerical weather pred., Ame. Met. Soc.*, 745-750.

Stull, R. B., and A. G. M. Driedonks, 1987: Applications of the transilient turbulence parameterization to atmospheric boundary layer simulations., *Bound.-Layer Meteor.*,**40**, 209-239.

Stull, R. B, 1990: *An introduction to boundary layer meteorology.*, Boston, Kluwer academic publishers, 666pp.

Thorpe, S. A., 1973: Turbulence in stably stratified fluids: A review of laboratory experiments., *Bound.-Layer Meteor.*,**5**, 95-119.

Troen, IB and L. Mahrt, 1986: A simple model of the atmospheric boundary layers; sensitivity to surface evaporation., *Bound.-Layer Meteor.*,**37**, 129-148.

Trout, D. and H. A. Panofsky, 1969: Energy dissipation near the tropopause., *Tellus*, **21**, 355-358.

Webster, C. A. G., 1964: An experimental study of turbulence in a density-stratified shear flow. *Fluid Mech.*, **19**, 221-245.

Wingaard, 1972: On surface layer turbulence. *Workshop on micrometeorology.*, 101-150, edited by D. A. Haugan, Boston, Ame. Met. Soc., 392p.

Wittich, K.-P., and R. Roth, 1984: A case study of nocturnal wind and temperature profiles over the inhomogeneous terrain of Northern Germany with some considerations of turbulent fluxes. *Bound.-Layer Meteor.*,**28**, 169-186.

Appendix

Appendix. Errors in estimating the mean flow structure from slant soundings

Presence of a large amplitude disturbance in the observed domain can cause significant errors in the estimated mean variables and their vertical gradients from slant soundings. As an example we consider the error in estimating the structure of the mean potential temperature due to the presence of large amplitude linear gravity wave in the domain. The observed potential temperature $\theta(x,z)$ can be written as

$$\theta(x,z) = \Theta(z) + \theta_0(z)\cos(kx + \ell z) \tag{A.1}$$

where $\Theta(z)$ is the *true* mean potential temperature, θ_0 is the amplitude of the potential temperature disturbance due to the wave.

For a linear gravity wave, $\theta_0(z)$ may be estimated by

$$\theta_0(z) \approx \left(\frac{d\Theta}{dz}\right)A \tag{A.2}$$

where A is the amplitude of vertical displacement of streamline due to wave activity. Then $\theta(x,z)$ can be rewritten as

$$\theta(x,z) = \Theta(z)\left(1 + \frac{1}{\Theta}\frac{d\Theta}{dz}A\cos(kx + \ell z)\right) \tag{A.3}$$

The horizontal mean value of $\theta(x,z)$ ($\overline{\theta}(z)$) can be estimated by integrating $\theta(x,z)$ over the horizontal intervals L_x. In the slant sounding, averaging over the horizontal length L_x includes averaging over the depth of L_z where L_x and L_z are related by the aircraft ascending/descending angle β as

$$L_z/L_x = \tan\beta. \tag{A.4}$$

In CABLE, $\tan\beta$ is between 1 and 6 %, hence $0.01 \leq L_z/L_x \leq 0.06$ The integral of the observed potential temperature $\theta(x,z)$ along the flight track is written as

$$\overline{\theta}(z) = \frac{1}{L_x}\int_{-L_x/2}^{+L_x/2}\frac{1}{L_z}\int_{z-L_z/2}^{z+L_z/2}\theta(x,z')dz'dx \qquad (A.5)$$

We assume that $L_z << \ell^{-1}$, that is the depth of the averaging region is smaller than the vertical wavelength of the wave, so that we can employ the WKB approximation in evaluating the integral $(A.5)$. Employing WKB approximation we assume that $\Theta(z)$ and $\ell(z)$ are constant in the layer where the averaging is taken. We also assume that $d\Theta/dz$ is also constant in the averaging depth. Then the double integral (A.5) is integrated to yield $\overline{\theta}(z)$ as

$$\overline{\theta}(z) = \Theta(z)\left[1 + \frac{1}{\Theta}\frac{d\Theta}{dz}A\frac{\sin(kL_x/2)}{kL_x/2}\frac{\sin(\ell L_z/2)}{\ell L_z/2}\cos(kx+\ell z)\right] \qquad (A.6)$$

For an exact estimation of the mean potential temperature at height z, we expect $\overline{\theta}(z) = \Theta(z)$. We define the relative error δ between the estimated mean value $\overline{\theta}(z)$ and the true mean value $\Theta(z)$ as

$$\delta \equiv \frac{\overline{\theta}(z)}{\Theta(z)} - 1 = \frac{1}{\Theta}\frac{d\Theta}{dz}A\frac{\sin(kL_x/2)}{kL_x/2}\frac{\sin(\ell L_z/2)}{\ell L_z/2}\cos(kx+\ell z) \qquad (A.7)$$

In $(A.7)$ $|\sin(kL_x/2)/(kL_x/2)| \leq 1$, $|\sin(\ell L_z/2)/(\ell L_z/2)| \leq 1$, and $|cos(kx + \ell z)| \leq 1$, hence the maximum error $|\delta|_{max}$ becomes

$$|\delta|_{max} = \frac{1}{\Theta}\frac{d\Theta}{dz}A. \qquad (A.8)$$

For typical amplitude of the wave, $\frac{d\Theta}{dz}A << \Theta$, hence the true mean of the potential temperature may be well represented by averaging over finite depth not losing much resolution in the vertical. One must note that, even though we may estimate mean variables quite accurately from slant sounding, the limitation on the averaging length due to the vertical variation of flow field may violate the

sampling criterion (Wyngaard,1972) for the estimation of the mean values of higher-order moments or flux.

The error in the estimation of the vertical gradient of the mean potential temperature can be obtained by differentiating the estimated mean potential temperature $\overline{\theta}$. We rewrite $\overline{\theta}$ from (A.7) as

$$\overline{\theta}(z) = \Theta(z)(1+\delta) \tag{A.9}$$

where δ is the relative error in the estimation of the mean value $(A.7)$. Then the gradient of the mean variable $\overline{\theta}(z)$ can be written

$$\frac{d\overline{\theta}}{dz} = \frac{d\Theta}{dz}(1+\delta) + \Theta(z)\frac{d\delta}{dz} \tag{A.10}$$

where $d\Theta/dz$ is the *true* vertical gradient of potential temperature. We substitute for δ from $(A.7)$ and assume that $\delta << 1$. Then neglecting $d^2\Theta/dz^2$ (A.10) can be rewritten as

$$\frac{d\overline{\theta}(z)}{dz} = \frac{d\Theta(z)}{dz}\left[1 - A\ell\frac{\sin(kL_x/2)}{kL_x/2}\frac{\sin(\ell L_z/2)}{\ell L_z/2}\sin(kx+\ell z)\right] \tag{A.11}$$

where A and ℓ are again the amplitude of the vertical displacement of streamline and the vertical wavenumber of the wave, respectively. We also assumed $L_z << \ell^{-1}$ so that WKB approximation can be justified. The relative error α in the estimation of the vertical gradient is defined as

$$\alpha \equiv \frac{d\overline{\theta}/dz}{d\overline{\Theta}/dz} \tag{A.12}$$

which can be obtained from (A.11) as

$$\alpha = -A\ell\frac{sin(kL_x/2)}{kL_x/2}\frac{\sin(\ell L_z/2)}{\ell L_z/2}\sin(kx+\ell z) \tag{A.12}$$

The relative error in the estimation of the mean stratification α increases as the wavenumber and amplitude of the streamline displacement in the vertical

increases. The relative error α also decreases as L_x and ℓL_z decrease. To ensure the correct vertical resolution $\ell L_z << 1$ which in turn restricts the horizontal averaging length L_x as

$$L_x = \frac{L_z}{\tan\beta} << \frac{\ell}{\tan\beta}. \qquad (A.13)$$

The condition $\ell L_z << 1$ gives $\sin(\ell L_z/2)/\ell L_z/2 \approx 1$ in (A.12). The magnitude of kL_x in (A.12) is limited by (A.13) as

$$kL_x << \frac{k\ell}{\tan\beta}. \qquad (A.14)$$

For an atmospheric condition where $U \approx 10$ m/s and $N \approx 10^{-2}$ s^{-1}, the vertical wave number for a hydrostatic gravity waves $\ell = N/U$ is $\ell \approx 10^{-3}$ m^{-1}. Thus kL_x decreases as the horizontal wavenumber decreases (long wave) and the ascending or descending angle increases. The term $sin(kL_x/2)/kL_x/2$ in (A.12) increases as kL_x decreases so the relative error. The maximum relative error in the estimation of the vertical gradient is

$$|\alpha|_{max} = A\ell \qquad (A.13)$$

Hence, the presence of large amplitude wave (large A in (A.13)) in the observational region can cause significant error in the estimation of the vertical gradient.